Topological Phenomena in Ultracold Atomic Gases

Hannah Price
Queens' College
University of Cambridge

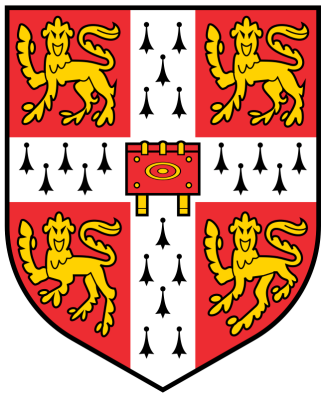

A thesis submitted for the degree of
Doctor of Philosophy
September 2013

For my family.

Preface

This thesis describes work undertaken in the Theory of Condensed Matter (TCM) group at the Cavendish Laboratory under the supervision of Prof. Nigel Cooper. Chapters 1 and 2 provide the relevant background for the work in this thesis. Subsequent chapters present original research that is published or submitted for publication as follows:

Chapter 3: Hannah M. Price and Nigel R. Cooper, *Mapping the Berry curvature from semiclassical dynamics in optical lattices*, Phys. Rev. A **85**, 033620 (2012) [1]

Chapter 4: Hannah M. Price and Nigel R. Cooper, *The Effects of Berry Curvature on the Collective Modes of Ultracold Gases*, arXiv:1306.4796 [2]

Chapter 5: Hannah M. Price and Nigel R. Cooper, *Skyrmion-antiskyrmion pairs in ultracold atomic gases*, Phys. Rev. A **83**, 061605(R) (2011) [3]

Chapter 5 was begun as a Part III project and was continued from October 2010 to January 2011. Chapters 3 & 4 describe work carried out between January 2011 and August 2013. This dissertation is the result of my own work and includes nothing which is the outcome of work done in collaboration except where specifically indicated in the text. This thesis does not exceed 60,000 words.

Acknowledgements

The research in this thesis was supported financially by an Engineering and Physical Sciences Research Council studentship. I am also grateful to Queens' College Cambridge for their continued support, as well as their award of the Munro studentship for teaching throughout 2012-2013.

During my PhD, I have learnt enormously from my supervisor, Nigel Cooper. I am deeply indebted to him for his academic guidance, support and patient teaching. His insight into physics has been a constant inspiration to me, and it has been a pleasure and a privilege to work with him over the last few years.

Thank you to everyone in TCM for creating a vibrant and stimulating community. Most of all, I am grateful for the companionship and counsel of my officemates: Richard Brierley, William Belfield, Sam Greenbury, Wave Ngampruetikorn and Marianne Bauer. There are too many people to thank in TCM for interesting and useful conversations, but in particular I would like to mention Stefan Baur, Jonathan Edge, Anson Cheung, Felix Nissen, Gunnar Möller, Johannes Hofmann, Tom Price and Gareth Conduit. A special thank you also to Ben Simons and Zoran Hadzibabic for inspiring me as an undergraduate, and to David Khmelnitskii for his wonderful graduate lectures. I am indebted to the unparalleled computing support of Michael Rutter and Daniel Corbett, who, together with our administrators over time: Tracey Ingham, Helen Verrechia and David Taylor, have kept TCM running smoothly.

Finally, my heartfelt appreciation goes to my friends and family. I would like to thank Nalini, Alice, Keir, James, Sarah and Charlotte for their wonderful friendship over the years. To Andrew I owe a huge debt for so much happiness. Most of all, my deepest love and thanks go to my parents and my brother for their constant support and encouragement.

Summary

Topological phenomena arise in a wide range of systems, with fascinating physical consequences. There is great interest in finding new ways to measure such consequences in ultracold atomic gas experiments. These experiments have significant advantages over the solid-state as ultracold atoms are controllable, tuneable and clean. They can also be used to investigate properties which are inaccessible in other quantum systems.

We explore some of the novel features of topological energy bands and topological solitons in ultracold gases. Topological energy bands have important geometrical properties described by the Berry curvature. Bands with nonzero Berry curvature arise in key areas of current research, such as optical lattices with more than one band; strong artificial magnetic fields and 2D spin-orbit coupling. Topological solitons are also relevant to cutting-edge experiments as they can be created and studied with high temporal and spatial resolution.

In this thesis, we investigate the consequences of Berry curvature for the semiclassical dynamics of a wavepacket and the collective modes of an ultracold gas. We also study theoretically the dynamics of skyrmion-antiskyrmion pairs in a Bose Einstein condensate.

Firstly, we propose a general method by which experiments can map the Berry curvature across the Brillouin zone, and thereby determine the topological properties of the energy bands of optical lattices. The Berry curvature modifies the semiclassical dynamics and hence the trajectory of a wavepacket undergoing Bloch oscillations. Our general protocol allows a clean measurement from the semiclassical dynamics of the Berry curvature over the Brillouin zone. We discuss how this protocol may be implemented and explore the semiclassical dynamics for three relevant systems. We discuss general experimental considerations for observing Berry curvature effects before reviewing some of the progress in the field since the publication of our work.

Secondly, we show that the Berry curvature changes the hydrodynamic equations of motion for a trapped Bose-Einstein condensate, and causes significant modifications to the collective mode frequencies. We illustrate our results for the case of two-dimensional Rashba spin-orbit coupling in a Zeeman field, where we also apply both a sum rule and an operator approach to the dipole mode. Extending the operator method, we derive the effects of Berry curvature on the dipole mode in very general settings. We show that the sizes of these effects can be large and readily detected in experiment. Collective modes therefore provide a sensitive way to measure geometrical properties of topological energy bands.

Lastly, we study theoretically the dynamics of two-component Bose-Einstein condensates in two dimensions, which admit topological excitations related to the skyrmions of nuclear physics. We explore a branch of uniformly propagating solitary waves, which, at high momentum, can be viewed as skyrmion-antiskyrmion pairs. We study these solitary waves for a range of interaction regimes and show that, for experimentally relevant cases, there is a transition to spatially extended spin-wave states at low momentum. We explain how this can be understood by analogy to the two-dimensional ferromagnet and discuss how such solitary waves can be generated and studied in experiment.

Contents

Chapter 1

Introduction

1.1 Topological Phenomena in Quantum Mechanics

Topology is an important area of mathematics that studies the global characteristics of a manifold. Let us consider the surface of a torus. Locally, a torus is described by geometrical properties, such as the curvature of the surface. Globally, the curvature is related to a genus; an invariant which counts the number of "holes" in the surface. However, unlike local geometrical properties, the genus is a topological feature. It cannot be changed by continuously deforming or stretching the surface; instead, a new hole must be ripped in the torus or the old hole must be sealed up.

Topological features therefore have several very special properties. They are global, discrete and robust against small perturbations. They also allow us to classify and distinguish objects; for instance, tori have a genus of one, while spheres have a genus of zero. When applied to quantum mechanics, such properties have many powerful consequences. For example, topological robustness underlies the remarkable quantisation of conductance in the quantum Hall effect[4], while topological invariants have helped us to predict, classify and understand new quantum phases of matter, such as topological insulators[5, 6].

In this thesis, we discuss two classes of phenomena which are currently of great interest in ultracold atomic gases: solitons and energy bands. Physically, these phenomena are very different. On the one hand, solitons in ultracold gases are localised excitations of the Gross-Pitaevskii wave-function, $|\psi(\boldsymbol{r})\rangle$; types of solitons

include quantum vortices and skyrmions[7]. On the other hand, optical lattices can be used to impose periodic potentials on an ultracold gas. The eigenstates then form energy bands in momentum space. These are the Bloch functions over the Brillouin zone[8].

However, these seemingly disparate areas can be united through the mathematics of topology. Topological solitons are those defects which cannot be removed from the ground-state by continuously deforming the wave function. They are characterised by an integer topological index or winding number[7]. Likewise, energy bands can be described by topological invariants, which cannot be changed without closing the gap to another band[5, 6]. When non-zero, these invariants have fascinating consequences such as the quantum Hall effect and the topological insulators mentioned above[1].

Topology is an important unifying concept in quantum mechanics. As we discuss in Sections 1.1.1 and 1.1.2, both topological energy bands and topological solitons have many applications in condensed matter physics, and are currently of great interest in ultracold atomic gases. We introduce some relevant properties of ultracold gas experiments in Section 1.2, and outline in Section 1.3 how this thesis will explore the novel features of topological energy bands and topological solitons in ultracold atomic gases.

1.1.1 Topological Energy Bands

One of the most interesting and surprising developments in band theory was the realization that the physical properties of any resulting energy band are not only encoded in its energy spectrum, $E_n(\boldsymbol{p})$, for all momenta, $\boldsymbol{p}$, and bands, n (the "bandstructure" in the usual sense). In addition, there are important physical consequences related to the topology and geometry of the eigenstates that form the band[4, 5, 6].

[1] We can also see the underlying connections between these phenomena by considering mappings from a physical "base space" onto a "target manifold"[7]. For solitons, we map real space, $\boldsymbol{r}$, onto the wave function $|\psi(\boldsymbol{r})\rangle$, while for energy bands, momentum space, $\boldsymbol{p}$, is mapped onto $|\psi(\boldsymbol{p})\rangle$. Then, in both cases, mappings are topologically distinct if they cannot be continuously deformed into each other. Classifying mappings in this way is known as homotopy theory[7].

As hinted at above, there is a deep connection between topology and geometry. In this section, we begin by introducing the local geometrical Berry curvature (which is the central focus of Chapters 3 and 4). We show how this can be connected to the global topology of the band, and discuss some of the exotic phenomena that can result when a band has nontrivial geometrical and topological properties.

The Berry Phase & the Berry Curvature

To understand the Berry curvature, we shall begin with the Berry phase. A system picks up a Berry phase when the parameters of its Hamiltonian are varied adiabatically around a closed contour[9]. We consider a general single-particle Hamiltonian, $H(\boldsymbol{p})$, which has eigenstates, $|n\boldsymbol{p}\rangle$, and non-degenerate eigenvalues, $E_n(\boldsymbol{p})$. This energy dispersion could be from an optical lattice, where $\boldsymbol{p} = \hbar\boldsymbol{k}$ is the crystal momentum in the Brillouin Zone, or a spin-orbit coupling Hamiltonian, where $\boldsymbol{p}$ is the single-particle momentum.

Under the application of a weak external force, the momentum, $\boldsymbol{p}$, evolves with time. For sufficiently slow evolution, $\boldsymbol{p}(t)$, the quantum adiabatic theorem states that a system initially in eigenstate $|n\boldsymbol{p}(t=0)\rangle$, will remain in an instantaneous eigenstate $|n\boldsymbol{p}(t)\rangle$ up to a phase factor, i.e. there will be no transitions between bands[2][10]. Therefore at a time t, the state of the particle is:

$$|\psi_n(t)\rangle = e^{i\gamma_n(t)} e^{-\frac{i}{\hbar}\int_0^t dt' E_n(\boldsymbol{p}(t'))} |n\boldsymbol{p}(t)\rangle \tag{1.1}$$

where the second exponential is the dynamical phase factor that depends on how fast the particle moves. The first exponential is a geometrical phase factor, which only depends on the path travelled. This can be seen by substituting Eq. 1.1 into the time-dependent Schrodinger equation, $i\hbar\frac{\partial}{\partial t}|\psi_n(t)\rangle = H(\boldsymbol{p}(t))|\psi_n(t)\rangle$, and multiplying by $\langle n\boldsymbol{p}(t)|$. Then:

$$\gamma_n = \int_{\mathcal{C}} d\boldsymbol{p} \cdot \boldsymbol{A}_n(\boldsymbol{p}) \tag{1.2}$$

$$\boldsymbol{A}_n(\boldsymbol{p}) \equiv i\langle n\boldsymbol{p}|\frac{\partial}{\partial \boldsymbol{p}}|n\boldsymbol{p}\rangle, \tag{1.3}$$

[2]The adiabaticity conditions are that the eigenstates remain non-degenerate at all times and that $\hbar|\langle m\boldsymbol{p}|\frac{\partial H}{\partial t}|n\boldsymbol{p}\rangle| \ll |E_m(\boldsymbol{p}) - E_n(\boldsymbol{p})|^2$, where m, n are two different bands.

where γ_n is the Berry phase, $\boldsymbol{A}_n(\boldsymbol{p})$ is the gauge-dependent Berry connection and $\mathcal{C}$ is the path travelled. For an open contour, this phase can always be gauged away[3] [11]. However, the geometric phase is gauge-invariant (modulo 2π) for cyclic evolution along a closed contour[4][9]. This is commonly known as the Berry phase:

$$\gamma_n = \oint_{\mathcal{C}} d\boldsymbol{p} \cdot \boldsymbol{A}_n(\boldsymbol{p}) = \int_{\mathcal{S}} d\mathbf{S} \cdot \boldsymbol{\Omega}_n(\mathbf{p}) \tag{1.4}$$

$$\boldsymbol{\Omega}_n(\boldsymbol{p}) \equiv \boldsymbol{\nabla}_p \times \boldsymbol{A}_n(\boldsymbol{p}) = i\frac{\partial}{\partial \boldsymbol{p}} \times \langle n\boldsymbol{p}|\frac{\partial}{\partial \boldsymbol{p}}|n\boldsymbol{p}\rangle, \tag{1.5}$$

where $\mathcal{S}$ is the surface enclosed by the contour, and we have used Stokes' theorem to introduce the Berry curvature, $\boldsymbol{\Omega}_n(\boldsymbol{p})$ (see also Figure 1.1). The Berry curvature is a local geometrical property of the eigenstates; it is gauge-invariant and so observable. It vanishes when both time-reversal and inversion symmetries are present. The Berry phase is similar to the Aharonov-Bohm phase, with the Berry curvature playing the role of a magnetic field in momentum space.

Hereafter, we consider the two-dimensional(2D) xy plane, where the Berry curvature is a scalar: $\boldsymbol{\Omega}_n(\boldsymbol{p}) = \Omega_n(\boldsymbol{p})\hat{\boldsymbol{z}}$. The Berry curvature can also be written as:

$$\Omega_n(\boldsymbol{p}) \equiv i\sum_{n'\neq n} \frac{\langle n\boldsymbol{p}|\frac{\partial H}{\partial p_x}|n'\boldsymbol{p}\rangle\langle n'\boldsymbol{p}|\frac{\partial H}{\partial p_y}|n\boldsymbol{p}\rangle - \langle n\boldsymbol{p}|\frac{\partial H}{\partial p_y}|n'\boldsymbol{p}\rangle\langle n'\boldsymbol{p}|\frac{\partial H}{\partial p_x}|n\boldsymbol{p}\rangle}{(E_n - E'_n)^2} \tag{1.6}$$

where we have used the relation $\langle n|\frac{\partial H}{\partial \boldsymbol{p}}|n'\rangle = \langle\frac{\partial n}{\partial \boldsymbol{p}}|n'\rangle(E_n - E'_n)$ on Eq. 1.5 [12]. This gives additional physical insight into the origin of this geometrical property. Under the adiabatic approximation, we project our system into a single band. The effect of higher bands is then represented by the Berry curvature. Another way to view this is in terms of "fast" and "slow" evolving wave functions. The motion of the "fast" subsystem alters the behaviour of the "slow" subsystem through the Berry effects. A good example of this is in the Born-Oppenheimer procedure, where a Berry connection appears naturally when the fast electronic motion is separated

[3]Under a gauge transformation $|n\boldsymbol{p}\rangle \to e^{i\zeta(\boldsymbol{p})}|n\boldsymbol{p}\rangle$, the Berry connection transforms as $\boldsymbol{A}_n(\boldsymbol{p}) \to \boldsymbol{A}_n(\boldsymbol{p}) - \frac{\partial}{\partial \boldsymbol{p}}\zeta(\boldsymbol{p})$. The Berry phase is changed by $\zeta(\boldsymbol{p}(t=0)) - \zeta(\boldsymbol{p}(t=T))$, where T is the final time. The gauge, ζ, can be chosen to cancel out the geometric phase accumulated along an open path.

[4]For cyclic evolution, the initial point, $\boldsymbol{p}(t=0)$, and the final point, $\boldsymbol{p}(t=T)$ is the same. However, we require at every point that $e^{i\zeta(\boldsymbol{p})}$ is single-valued. This implies that $\zeta(\boldsymbol{p}(t=0)) - \zeta(\boldsymbol{p}(t=T)) = 2\pi \times$ integer. Therefore the geometric phase can only be changed by 2π under a gauge transformation for a closed contour.

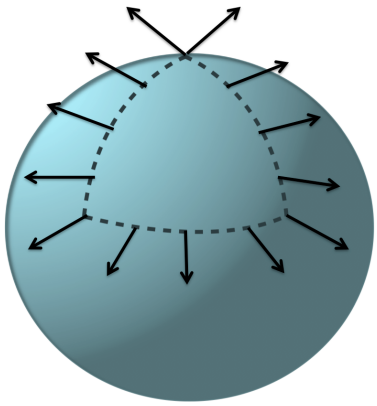

Figure 1.1: An intuitive example of a geometrical phase factor: the rotation of a vector after parallel transport around a closed path on a sphere. The mismatch angle (anholonomy) depends on the surface enclosed and its Gaussian curvature. The Berry phase is the analogous phase factor that arises from quantum mechanical parallel transport.

from the slow nuclear motion[9, 13, 14].

Finally, we note that a degenerate sub-space of bands can be described by a matrix Berry curvature with *non-Abelian* gauge structure[15]. The Berry connection and curvature become:

$$\mathcal{A}_{mn}(\boldsymbol{p}) \equiv i\langle m\boldsymbol{p}|\frac{\partial}{\partial \boldsymbol{p}}|n\boldsymbol{p}\rangle, \tag{1.7}$$

$$\mathcal{F}(\boldsymbol{p}) \equiv \boldsymbol{\nabla}_p \times \mathcal{A}(\boldsymbol{p}) - i\mathcal{A}(\boldsymbol{p}) \times \mathcal{A}(\boldsymbol{p}) \tag{1.8}$$

where m and n are degenerate bands. In this thesis, we focus on non-degenerate bands, and so only consider the Abelian Berry curvature (Eq. 1.5). However, we shall return to these concepts briefly when discussing the generation of spin-orbit coupling in ultracold gases (Section 2.2).

Connection to Topology

The deep connection between geometry and topology is well-known from mathematics. The Gauss-Bonnet theorem relates the Gaussian curvature of a closed manifold to the Euler characteristic, a global topological invariant related to the genus of the surface. We shall now see that a similar relation holds between the Berry curvature and the Chern number, a topological invariant of an energy band[16].

Let us consider the 2D Brillouin Zone of a periodic lattice, where $\boldsymbol{p} = \hbar\boldsymbol{k}$ is the crystal momentum. As $\boldsymbol{k}$ is also periodic, this manifold is a torus; e.g. for a unit cell of dimensions $a \times a$, the BZ is defined as $-\pi/a < k_{x/y} \leq \pi/a$. If we choose the surface in Eq. 1.4 to be the whole BZ, we are integrating the Berry curvature over a

closed manifold. The contour, $\mathcal{C}$, is then equivalent to a point, and the Berry phase must be quantised as $2\pi \times$ integer (Figure 1.2). This integer is called C, the Chern number. It is a topological invariant: its value cannot be changed by continuous evolution of the physical system without closing the gap to another band. The Chern number can be nonzero when time-reversal symmetry is broken. For systems with additional global symmetries (time reversal, particle/hole, or chiral) other forms of topological invariant can appear[5, 6].

Physical Consequences of Topological Energy Bands

The importance of the topological features of energy bands was first pointed out in the seminal work of Thouless *et al.*[4] in the context of the integer quantum Hall effect. The integer quantum Hall effect is the exact quantisation of the Hall conductivity, σ_{xy}, of a 2D electron system in a strong magnetic field. In their work, Thouless *et al.* showed that this remarkable quantisation was topological: a filled band has $\sigma_{xy} = C\frac{e^2}{\hbar}$, corresponding to the existence of C chiral edge modes. Since this discovery, topological invariants have been found to have many other important physical consequences. For example, they underlie the quantum spin Hall effect and topological insulators[5, 6].

The local geometrical properties of the eigenstates can also have direct physical

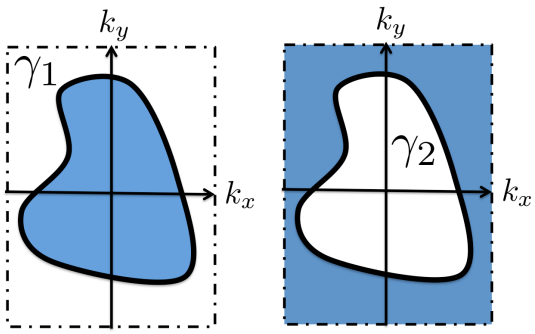

Figure 1.2: How to see the quantisation of the Berry phase intuitively. The dashed rectangle indicates the Brillouin zone. To find γ for the black contour, we integrate over the surface in blue. For the left hand picture, this gives γ_1, and for the right, γ_2 (as the Brillouin zone is a closed manifold). The Berry phase is defined modulo 2π, and so $\gamma_1 - \gamma_2 = 2\pi \times$ integer. If the contour encloses the whole Brillouin zone, the left surface grows to fill the dashed rectangle and the right vanishes. Then $\gamma_2 \to 0$ and γ_1 is quantised.

effects when a band is partially filled. The Berry curvature plays an important role in the anomalous quantum Hall effect [17, 18, 19]. This is the appearance of a large spontaneous Hall current in a ferromagnet in an electric field but without a magnetic field. There has been much controversy over the interpretation of this effect and there are various mechanisms responsible (for a recent review, see Ref. [20]). One of these is the so-called intrinsic contribution, originally due to Karplus and Luttinger[21]. This has since been interpreted in terms of the Berry curvature of the energy bands due to the spin-orbit(SO) interaction (for more about SO coupling and the Berry curvature see Section 2.2)[18, 17]. The anomalous contribution to the Hall conductivity is found by integrating the Berry curvature over all occupied states below the Fermi energy in the partially filled bands[5]. Therefore, in some sense this is an "unquantized" quantum Hall effect [12].

In this thesis, we will focus on two other important physical consequences of the Berry curvature. Firstly, the Berry curvature can strongly modify the semiclassical dynamics of a wavepacket[22, 23, 24] as we shall introduce in Chapter 3. Secondly, in Chapter 4, we derive how the Berry curvature changes the hydrodynamic equations of motion for a trapped Bose-Einstein condensate, and causes significant modifications to the collective mode frequencies.

1.1.2 Topological Solitons

Above, we have discussed how the topology of a band can affect even a single non-interacting particle. Now we turn to collective many-body physics and the topological excitations of a condensate which rely intrinsically on mean-field interactions. A soliton or solitary wave is a localised, non-singular excitation that can move through a system without distortion[6] [25, 8]. These excitations are possible when both dispersion and nonlinearity are present. Bose-Einstein condensates can support solitons as the nonlinearity is provided by the weak interactions and the dispersion by the

[5] Haldane also incorporated this into Landau-Fermi liquid theory by showing that the Hall conductivity is a Fermi surface property; it can be found from the Berry phase of the Fermi surface quasiparticles (modulo 2π) [19].

[6] We use the terms soliton and solitary wave interchangeably as is common in the literature of BECs[8]. Formally, however, solitons are a sub-class of solitary waves, with the extra property that they can interact with each other and emerge undistorted. Solitons can have this property when the underlying field theory is integrable, which is not applicable to the 2D BEC considered here.

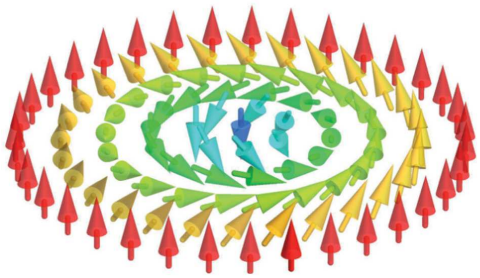

Figure 1.3: Figure taken from [31]. Schematic illustration of a skyrmion configuration. Arrows indicate the local spin vector field, $\vec{\ell}(\boldsymbol{r})$. The spins sweep over the unit sphere and rotate by π from the centre to the outer edge.

kinetic energy (see the mean-field Gross-Pitaevskii equation below: Eq. 1.11). A solitary wave is also topological if it cannot be removed by continuous deformation of the wavefunction.

Topological defects have long been a very rich and interesting subject in theoretical physics, with applications in many disciplines[26]. The simplest topological defect is a vortex, around which the phase of an order parameter winds in units of 2π. In a superfluid, the density drops to zero in the core of a vortex, while outside, the circulation is quantised[8]. If there are extra degrees of freedom, even more exotic topological solitons are possible, such as the skyrmion. The skyrmion was first introduced in the 1960s as a topological soliton describing nuclei[27] and variants have since been found to be important in condensed matter systems: they describe the charged excitations of certain quantum Hall ferromagnets[28]; and lattices of skyrmions have been observed in chiral magnets[29, 30].

In this thesis, we study a branch of uniformly propagating solitary waves in a 2D Bose Einstein condensate, which at large momentum are skyrmion-antiskyrmion pairs. For two spatial dimensions, a skyrmion is a topological soliton in the local spin vector field, $\vec{\ell}(\boldsymbol{r})$, characterised by a non-zero topological index of the map $S^2 \to S^2$ (in 3D, the map is $S^3 \to S^3$[27])[7]. A non-zero index arises when the local spin vector field rotates by π from the centre to the outer edge of the soliton, such that the 2D configuration sweeps over the unit sphere (Figure 1.5). An antiskyrmion carries a topological index of the opposite sign. In ultracold gases, such a local spin vector field, $\vec{\ell}(\boldsymbol{r})$, can be defined for a multi-component condensate (Section 1.2.2). Then skyrmions are a type of coreless vortex, analogous to the Anderson-Toulouse vortex in ^{3}He-A[32].

[7]For a full introduction to homotopy theory and topological excitations in Bose-Einstein condensates see Ref. [7].

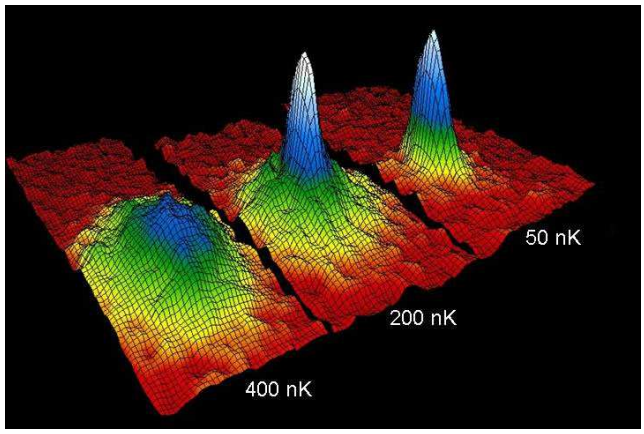

Figure 1.4: Velocity distribution of rubidium as the gas is cooled through the transition into a Bose-Einstein condensate(Figure from Ref. [43])[33]. In the centre and right pictures, the BEC appears as a peak around zero momentum, as the lowest energy state becomes macroscopically occupied.

1.2 Ultracold Atomic Gases

Ultracold atomic gases are dilute clouds of atoms cooled close to zero temperature, where quantum effects are important[8]. For sufficiently low temperatures, bosons condense into a Bose-Einstein condensate (BEC)[33, 34, 8], while fermions can form a degenerate Fermi gas[35, 36]. BECs were first experimentally created in 1995, for a gas of rubidium[33] and a gas of sodium atoms[34]. Since then, the Nobel prize has been awarded for these important achievements and there has been an explosion of experimental and theoretical research in the field. There is an accompanying wealth of resources; key books include Refs. [37, 8, 7], while some useful review articles are Refs. [38, 39, 40, 36, 41, 42].

Ultracold gases have been used to study many important areas of quantum physics, such as superfluidity and vortices[44], matter-wave interference[45], the effects of dimensionality[46, 47] and the superfluid-Mott insulator transition[48, 49]. This has been possible because ultracold atomic gases are excellent experimental systems: they are controllable, tunable and clean, and they can be studied with high temporal and spatial resolution. Thanks to these properties, ultracold atomic gases provide the opportunity now and in the future to explore interesting phenomena from solid-state systems in new and exciting ways. In particular, ultracold gases should open up new possibilities for research into strongly correlated physics in quantum many-particle systems. For the purposes of this thesis, we briefly intro-

[8]This is when $\lambda_T > \bar{a}$ where $\bar{a}$ is the average interparticle distance, $\lambda_T = \sqrt{\frac{2\pi\hbar^2}{Mk_BT}}$ is the thermal de Broglie wavelength, M is the particle mass, k_B is the Boltzmann constant and T is the temperature[8].

duce some relevant aspects of Bose-Einstein condensates[9]. We begin by discussing trapping, dimensionality and interactions, before turning to multi-component BECs and the creation and detection of skyrmions. We then introduce optical lattices and explore how they may be used to realise energy bands with nontrivial Berry curvature.

1.2.1 Trapping, Dimensionality and Interactions

Trapping and Dimensionality

Ultracold atoms can be trapped by magnetic and optical fields. For typical experimental traps, the resulting potential is well approximated by a simple harmonic potential:

$$V(x,y,z) = \frac{1}{2}M(\omega_x^2 x^2 + \omega_y^2 y^z + \omega_z^2 z^2) \tag{1.9}$$

where $\omega_{x,y,z}$ is the harmonic trapping frequency along that direction[10]. By controlling the trapping frequencies, the dimensionality of the cloud can be changed. For example, the motion along the z direction is frozen out for bosons if $\hbar\omega_z \gg k_B T$, where $k_B T$ is the thermal energy. This corresponds to requiring that the thermal energy is much less than the energy difference between the ground and first excited state[8]. Freezing out the motion along one direction leads to a quasi-2D condensate, while freezing out along two leads to a quasi-1D system. This is important as in this thesis we primarily consider quasi-2D systems. An alternative route to lower dimensions is provided by optical lattices, as discussed below.

Interparticle Interactions

Interactions in dilute BECs can be effectively described by two-body scattering. This is because for cold temperatures and low densities, the inter-particle separations are typically several orders of magnitude larger than the length scale of the inter-

[9]For a discussion of Fermi gases, see, for example, Refs. [8, 36].

[10]Many common experimental traps will be anisotropic. For example the time-averaged orbiting potential(TOP) trap, has $\omega_z/\omega_{x,y} = \sqrt{8}$, where the axis of symmetry is chosen along $\hat{z}$.

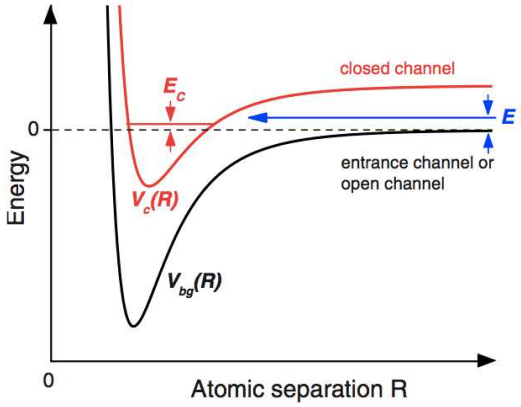

Figure 1.5: Figure taken from [50]. The two-channel model for a Feshbach resonace. Two atoms interact with energy E, in the open channel (represented by the background potential curve, V_{bg}). They couple resonantly to the molecular bound state at energy E_c in the closed channel (represented by V_c). This coupling mixes the channels and shifts the scattering length.

atomic interaction[11] [8]. At low energies, two-body interactions can be replaced by an effective contact interaction. In 3D, for particles of equal mass this is:

$$g_{\text{eff}}(\boldsymbol{r}, \boldsymbol{r}') = g\delta(\boldsymbol{r} - \boldsymbol{r}') = \frac{4\pi\hbar^2 a_s}{M}\delta(\boldsymbol{r} - \boldsymbol{r}') \tag{1.10}$$

where δ is a Dirac delta function, a_s is the scattering length and M is the particle mass[8]. A BEC is stable for repulsive interactions and a positive a_s. The scattering length can be tuned by changing the atomic species or by using a Feshbach resonance. A Feshbach resonance occurs if the energy of a scattering state in an open channel approaches the energy of a molecular bound state in a closed channel[12] [8, 50]. By changing the energy of the atomic scattering state relative to the molecular state, the coupling, and hence the effective scattering length, is varied. This can be controlled, for example, by an external magnetic field if the magnetic moments of the states are different. The Feshbach resonance has consequently become a very important tool in ultracold atomic gases, as it can tune the effective interaction for a large range of positive and negative values[50].

A weakly interacting BEC at zero temperature can be described by the mean-field Gross-Pitaevksii equation[8]. The Hartree approximation assumes that all N particles are condensed in the same single-particle state, $\psi(\boldsymbol{r})$ (normalised such that $\int d\boldsymbol{r}|\psi(\boldsymbol{r})|^2 = N$). Then the many-body wave-function is $\Psi(\boldsymbol{r}_1, \boldsymbol{r}_2, ...\boldsymbol{r}_N) \propto$

[11] The requirement of diluteness can be expressed as $|a_s| \ll \rho^{-1/3}$, where a_s is the scattering length and ρ is the density[37].

[12] Channels represent the sets of possible internal states of the atoms in the scattering process[8]. Two incoming particles have an energy, E. If this is larger than the dissociation energy of two particles in that channel, the channel is "open" and if this is less, than the channel is "closed"[50].

$\prod_{i=1}^{N} \psi(\boldsymbol{r}_i)$, and the Gross-Pitaevskii equation is:

$$-\frac{\hbar^2}{2M}\boldsymbol{\nabla}^2\psi(\boldsymbol{r}) + V_{\text{ext}}(\boldsymbol{r})\psi(\boldsymbol{r}) + g|\psi(\boldsymbol{r})|^2\psi(\boldsymbol{r}) = \mu\psi(\boldsymbol{r}) \tag{1.11}$$

where V_{ext} is any external potential, μ is the chemical potential and $\psi(\boldsymbol{r})$ is the condensate wave-function. This is a non-linear Schrödinger equation which takes into account interactions through the mean-field potential, $g|\psi(\boldsymbol{r})|^2$. This equation can exhibit some types of topological excitations, including vortices. However, more degrees of freedom are required to support skyrmions; therefore we now introduce multicomponent BECs.

1.2.2 Multicomponent Bose-Einstein Condensates

A multicomponent BEC consists of two or more bosonic species. These can be different atoms, isotopes or hyperfine states[13]. With these additional degrees of freedom, the wave-function becomes a "spinor". For two species, it is:

$$\begin{pmatrix} \psi_1(\boldsymbol{r}) \\ \psi_2(\boldsymbol{r}) \end{pmatrix} = \sqrt{\rho_0} \begin{pmatrix} \chi_1(\boldsymbol{r}) \\ \chi_2(\boldsymbol{r}) \end{pmatrix} \tag{1.12}$$

where ψ_i is the condensate wave function in component i, ρ_0 is the total density and $\boldsymbol{r}$ is the spatial position. As the name "spinor" suggests, this extra degree of freedom plays the role of the spin, i.e. a local spin vector field, $\vec{\ell}$, can be defined as a function of position $\boldsymbol{r}$[51, 52] (Section 5.1.1). Multicomponent BECs provide a rich area for the study of skyrmions in three dimensions (3D)[53, 54] and two dimensions[44, 51, 55, 56]. At zero temperature and for weak interactions, the two-component system is described by two coupled Gross-Pitaesvkii equations:

$$-\frac{\hbar^2}{2M}\boldsymbol{\nabla}^2\psi_i(\boldsymbol{r}) + V_{\text{ext}}(\boldsymbol{r})\psi_i(\boldsymbol{r}) + \sum_j g_{ij}|\psi_j(\boldsymbol{r})|^2\psi_i(\boldsymbol{r}) = \mu_i\psi_i(\boldsymbol{r}). \tag{1.13}$$

[13] Hyperfine states are internal states of the atoms; they are eigenstates of the hyperfine interaction $\propto \boldsymbol{I}\cdot\boldsymbol{J}$ where $\boldsymbol{I}$ and $\boldsymbol{J}$ are respectively the operators for the nuclear spin and electronic angular momentum[8]. The eigenvalues of $\boldsymbol{F}^2$ (where the total angular momentum operator $\boldsymbol{F} = \boldsymbol{I} + \boldsymbol{J}$) are $F(F+1)$: F is a good quantum number as the hyperfine energy splitting is generally much larger than the BEC transition temperature[7]. The transitions between hyperfine states can be well controlled by lasers and external magnetic fields, so different hyperfine levels can represent different bosonic species.

The interaction strength of different species will not be the same in general (i.e. $g_{11} \neq g_{12} \neq g_{22}$). As we shall see in Section 5, these interaction imbalances can have interesting physical effects.

Creating and Studying 2D Skyrmions in BECs

Multicomponent BECs present an exciting opportunity to study skyrmions in ultracold gases. In this thesis, we investigate theoretically the dynamical properties of a 2D skyrmion-antiskyrmion pair in a two-component condensate. Our work is motivated by the recent experimental advances in the field, which will allow skyrmions to be imprinted in a gas and their dynamical properties to be studied.

Skyrmions can be created in two-dimensional BECs using various experimental techniques[44, 51, 57, 58]. For example, a 2D skyrmion has been imprinted in an untrapped BEC of ^{87}Rb using two spatially modulated Raman beams[51]. In this experiment, the BEC was initially prepared as a spin-polarized gas in the $|F{=}2, m_F{=}2\rangle$ hyperfine state. The Raman lasers coupled this state with the $|F{=}2, m_F{=}-2\rangle$ and $|F{=}2, m_F{=}0\rangle$ hyperfine states to create a multicomponent condensate[14]. The density and phase profile of a 2D skyrmion was imprinted over the three states by choosing the spatial variation and orbital angular momentum of the Raman lasers appropriately. Even more exotic spin textures, including a skyrmion-antiskyrmion pair, have been imprinted using holographically produced Raman lasers[57]. However, a limitation of these schemes is that the gas is untrapped when the texture is imprinted. Therefore another experiment has used a spin rotation technique[15] to imprint a 2D skyrmion in a trapped polar BEC of ^{23}Na[58, 60].

The dynamical properties of skyrmion-antiskyrmion pairs would then be directly accessible in experiments, as BECs can be imaged and controlled with high temporal and spatial resolution[61, 63]. For example, the real-time dynamics of vortices can

[14] In a Raman process, an atom absorbs a photon from one beam, and emits a photon into a second beam. By tuning the frequency difference of the lasers to the hyperfine level splitting, the atoms are transferred from one state to another via a (virtual) excited state. Raman transitions are thus very important tools in the manipulation of ultracold gases.

[15] Adiabatically varying a real magnetic field drives transitions between the hyperfine states and imprints a state-dependent Berry phase[9, 58]. The result is to rotate the local spin vector field. Note a similar method was used much earlier to prepare 2D coreless vortices with Mermin-Ho boundary conditions[59].

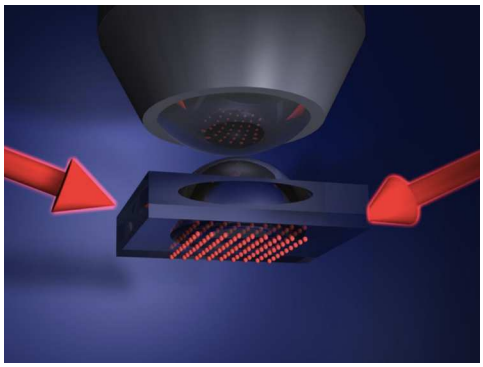

Figure 1.6: Sketch of the quantum gas microscope[61] (Figure taken from Ref. [62]). The 2D quantum gas is placed in a high aperture optical system. In this schematic there is also a holographically produced lattice potential. The atoms are measured in-situ with an optical resolution $\sim$ 600nm.

be observed by repeatedly extracting, expanding and imaging small fractions of a trapped cloud[63]. Alternatively, the quantum gas microscope images 2D ultracold gases with a spatial resolution of $\sim$ 600nm[61] (Figure 1.6). This has already been used to study the superfluid-to-Mott insulator transition at the single atom level, where fast local dynamics could be resolved[49]. It is now intended to combine this technique with the imprinting of spin textures using holographically produced Raman beams[57]. This would allow for a full study of the dynamical properties of these excitations.

1.2.3 Optical Lattices

Optical lattices are another crucial ingredient of many ultracold atom experiments (for reviews see Refs. [8, 40, 41, 64, 65]). These periodic potentials enable experiments to mimic and explore the behaviour of electrons moving through crystalline materials. For example, optical lattices have been able to simulate such important condensed matter models as the quantum Ising model[66] and the Bose-Hubbard model with its superfluid-to-Mott insulator transition[48, 49].

An optical lattice is created through the interference of laser beams. The atoms experience an a.c. Stark shift as the oscillating electric field of the light induces a dipole moment in each atom. The interaction shifts the energy of the atom, as if it were moving in a potential[8, 41]:

$$V = -\frac{1}{2}\alpha'(\omega)\langle \mathcal{E}(\boldsymbol{r},t)^2\rangle_t \tag{1.14}$$

where α' is the real part of the dynamical polarizability of the atomic level and ω is

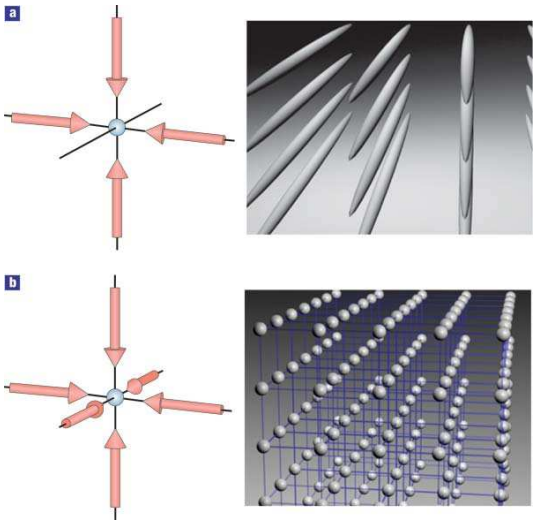

Figure 1.7: Optical lattices of different dimensionalities: figure taken from Ref. [67]. (a) A 2D lattice splits the cloud into many tightly-confined quasi 1D systems. (A 1D lattice, which is not shown here, would split the cloud into many 2D systems). (b) A 3D lattice leads to a cubic 3D array of harmonic oscillator potentials at each site.

the frequency of the electric field, $\mathcal{E}(\boldsymbol{r}, t)$. The brackets $\langle\rangle_t$ denote an average over a time much longer than the period. This potential is periodic in space if $\langle\mathcal{E}(\boldsymbol{r}, t)^2\rangle_t$ is periodic. However, in addition to this conservative potential, there is also dissipation and heating due to spontaneous emission of photons. This is minimised by ensuring a large detuning between the laser beams and any atomic resonances[16][64]. In optical lattices, the natural energy scale is set by the recoil energy, $E_R = h^2/2m\lambda^2$, where λ is the optical wavelength[8]. Similarly, we can define a recoil velocity, $v_R = h/m\lambda$, and a unit of force, $F_R = h^2/2m\lambda^3$.

Optical lattices are very controllable and adaptable experimental tools. The geometry, lattice constants and barrier heights can all be tuned directly in experiments, for instance, by varying the intensity, frequency or phase of the laser beams[8, 65]. By combining several lasers, optical lattices can also be created in one, two or three dimensions[8, 41] (Figure 1.7). This is directly relevant to this thesis, as we focus primarily on quasi-2D systems. Most importantly, as we shall now describe, optical lattices can also be engineered to have energy bands with nonzero Berry curvature.

Optical Lattices with Multiple Sites per Unit Cell

The Berry curvature vanishes for the simplest forms of optical lattice that have only one site per unit cell and hence only one energy band (see Eq. 1.6). Thanks to recent

[16]The photon scattering rate can be estimated as $\propto I/\Delta^2$ where I is the intensity, and Δ is the detuning[64]. The dipole potential is correspondingly $\propto I/\Delta$. Large detuning minimises photon scattering relative to the potential strength.

advances, optical lattices with multiple sites per unit cell are now realisable, including triangular[68], hexagonal[69, 70] and Kagomé[71] lattices as well as superlattice structures[72]. These systems have multiple energy bands and the Berry curvature can be non-zero, provided either inversion or time-reversal symmetry is broken[17].

To illustrate this, we consider the tuneable honeycomb lattice, created experimentally in Ref. [70] and used as one of our example systems[18] in Section 3.3.1. A honeycomb lattice has two sites per unit cell, and its two lowest bands touch at two "Dirac" points in the Brillouin zone[19]. By adjusting the lattice anisotropy, the Dirac points were moved experimentally around the BZ, and for high enough anisotropy, merged and annihilated[70]. This experiment was also able to introduce an onsite energy difference between the two sites in the unit cell. This energy difference breaks inversion symmetry, which is protecting the Dirac points. When inversion symmetry is broken, band gaps open at the Dirac points, and the energy bands have nonzero Berry curvature[12]. While the effects of Berry curvature were not studied in this experiment, this system will allow for the future investigation of the geometrically nontrivial bands as proposed, for example, in Section 3.3.1.

Breaking inversion or time-reversal symmetry is also closely linked to the pursuit of artificial gauge fields. For example, time-reversal symmetry must be broken to generate an artificial magnetic field in an ultracold gas, while Rashba spin-orbit coupling requires broken inversion symmetry. Energy bands with nontrivial geometrical and topological properties therefore play an important role in systems with artificial gauge fields. This is a key motivation for our work on topological energy bands, and so we introduce the concepts and schemes behind artificial gauge fields in more depth in the next chapter.

[17] The Chern number can only be nonzero if time-reversal symmetry is broken.

[18] To be precise, we shall study the asymmetric hexagonal lattice. The honeycomb lattice in this experiment does not have the full hexagonal symmetry although it shares the qualitative features.

[19] At a Dirac point, two bands intersect with a linear dispersion. The particles close to a Dirac point can be described by the relativistic Dirac equation for massless spin-1/2 particles. Dirac points are particularly important in graphene, for which the asymmetric hexagonal lattice serves as a simple model[73].

1.3 Outline of Thesis

In this chapter, we have introduced topological band theory, topological solitons, and ultracold atomic gases. We have seen how energy bands can have important geometrical features encoded in the Berry curvature, with remarkable physical consequences. We have discussed how such bands can arise for optical lattices with multiple sites per unit cell. In addition, we have introduced skyrmions: topological excitations with applications in many areas of physics. We have also described how skyrmions may be experimentally created and studied in multicomponent Bose-Einstein condensates.

In Chapter 2, we continue our introduction by reviewing artificial gauge fields in ultracold gases. This is a very important area of current research, where many schemes involve energy bands with nontrivial topological and geometrical properties. The purpose of this chapter is two-fold; we shall further motivate our work on topological energy bands, and introduce many of the experimental systems that will be used later as examples.

The experimental interest in realising topological energy bands in ultracold gases presents an excellent opportunity to study the properties of these bands in new ways. We propose in Chapter 3 a general "time-reversal" protocol for mapping out the Berry curvature from the semiclassical dynamics of a wavepacket. This method would allow experiments to measure the Berry curvature over the Brillouin zone for the first time. We demonstrate this protocol on three experimentally relevant models, discuss general experimental considerations and, finally, review developments in the field since the publication of our work.

We also show that the Berry curvature has other novel physical consequences in ultracold gases. In Chapter 4, we demonstrate that the Berry curvature changes the hydrodynamic equations of motion for a trapped Bose-Einstein condensate, and causes significant modifications to the collective mode frequencies. We illustrate our results for an example system and discuss various alternative theoretical approaches. Using an operator method, we derive the effects of Berry curvature on the dipole mode in very general settings, and show that these effects may be large. Collective

modes may therefore be a powerful tool for determining the geometrical properties of the condensate wave function.

Finally, in Chapter 5, we explore the dynamical properties of a two-component two-dimensional Bose-Einstein condensate. We identify a uniformly propagating branch of solitary waves, which at high momentum, can be viewed as skyrmion-antiskyrmion pairs. These solitary waves could be imprinted and studied with the experimental techniques described above. We study the dynamical properties of these excitations, and show that they are within current experimental capabilities.

Chapter 2

Artificial Gauge Fields

The pursuit of artificial gauge fields in ultracold atoms brings with it many fresh opportunities for studying energy bands with nontrivial topological and geometrical properties. The Berry curvature can only be non-zero if either time-reversal or inversion symmetry is broken. These are also the symmetries we break to create artificial magnetic fields and artificial Rashba spin-orbit coupling respectively. The current interest in generating artificial gauge fields is therefore a key motivation for our work on energy bands with interesting geometry and topology.

The aim of this chapter is to briefly introduce the main ideas and experiments in this area, and to provide the background for many of the example systems explored later in the thesis. We first discuss artificial magnetic fields in Section 2.1, before turning to artificial spin-orbit coupling in Section 2.2.

2.1 Artificial Magnetic Fields

Ultracold atoms are electrically neutral and do not experience the Lorentz force in a magnetic field[1]. Without this, phenomena such as the quantum Hall effect are inaccessible. Simulating artificial magnetic fields is therefore an important step towards exploring bands with interesting topology and nonzero Chern numbers.

The energy bands of a quantum Hall system are flat Landau levels. In flat

[1] A real magnetic field has other important physical effects on the atoms, for example, in the Zeeman shift on their internal energy levels.

bands, interactions dominate and strongly correlated many-body states can arise. Strong correlations can lead to the fractional quantum Hall(FQH) effect, where the conductance is quantised in rational fractions, rather than integer values, of e^2/h[74, 75]. FQH states can have many exotic properties, such as fractionalised excitations[75]. There is therefore also great interest in simulating quantum Hall physics in order to access interesting many-body physics in both fermionic and bosonic systems[76]. We shall consider the accessibility of strong correlations when reviewing current schemes.

2.1.1 Artificial Magnetic Fields in Rotating Gases

Artificial magnetic fields were first generated in rotating gases. The single-particle Hamiltonian of a trapped gas in a frame rotating at angular frequency, $\mathbf{\Omega}_r$, around the z axis is [76]:

$$\begin{aligned} H_r &= \frac{|\boldsymbol{p}|^2}{2M} + \frac{1}{2}M\omega_\perp^2(x^2+y^2) + \frac{1}{2}M\omega_\parallel^2 z^2 - \mathbf{\Omega}_r \cdot \boldsymbol{r} \times \boldsymbol{p} \\ &= \frac{|\boldsymbol{p} - M\mathbf{\Omega}_r \times \boldsymbol{r}|^2}{2M} + \frac{1}{2}M(\omega_\perp^2 - \Omega_r^2)(x^2+y^2) + \frac{1}{2}M\omega_\parallel^2 z^2 \end{aligned} \tag{2.1}$$

This is identical to the Hamiltonian of a particle with charge q in a magnetic field, $\boldsymbol{B} = 2M\mathbf{\Omega}_r/q$, and a modified harmonic trap: $V(\boldsymbol{r}) = \frac{1}{2}M(\omega_\perp^2 - \Omega_r^2)(x^2+y^2) + \frac{1}{2}M\omega_\parallel^2 z^2$. Therefore, rotation leads to an effective magnetic field in the rotating frame, with the Coriolis force mimicking the Lorentz force. Experimentally, a gas can be rotated at low frequencies by stirring it with laser beams[77, 78] or by rotating the confining magnetic potential[79]. Above a critical rotation frequency, the artificial magnetic field nucleates vortices and regular vortex arrays can be observed[77, 78]. For useful reviews discussing rotating gases see Refs. [76, 80, 40].

As $\boldsymbol{B}$ is proportional to $\mathbf{\Omega}_r$, rotating the gas faster generates larger artificial magnetic fields and higher vortex density. However, the centrifugal force appears in the modified trapping potential and so limits the rotation rate. When $\Omega_r > \omega_\perp$, the modified trap disappears and the atoms fly apart[2]. Achieving the rapid rotation limit is experimentally demanding[76, 80, 40]. It can be done, for example,

[2]At the centrifugal limit, when $\Omega_r = \omega_\perp$, the gas is effectively 2D and uniform perpendicular to the rotation axis, so the eigenstates are macroscopically degenerate Landau levels.

with an additional quartic trapping potential[81] or using an evaporative spin-up technique[82].

To explore strongly correlated physics, the 2D particle density must be comparable to the mean vortex density[3][76]. The centrifugal limit places an upper bound on the vortex density: $n_v = |\boldsymbol{B}_{\max}|q/h = 2M\omega_\perp/h$. However, in practice this is very small compared to the achievable particle densities for large particle numbers[76]. Therefore the strongly correlated regime is so far inaccessible in rotating gases[4]. Another key disadvantage of this approach is that the magnetic field generated is in the rotating frame. Any non-axisymmetric perturbations in the lab frame will translate into time-dependent potentials in the rotating frame[76]. These are difficult to treat and can lead to heating. To avoid this problem, focus has shifted towards simulating effective magnetic fields in the lab frame, for example, by using the dressed state schemes that we shall now discuss.

2.1.2 Artificial Magnetic Fields with Dressed State Schemes in the Continuum

These schemes use a spatially varying atom-light coupling to generate an artificial magnetic field. In Eq. 1.5, we saw that the Berry curvature, $\Omega(\boldsymbol{p})$, acts like a magnetic field in momentum-space. This definition could equally be applied to any parameter-space of the Hamiltonian. Replacing the momentum, $\boldsymbol{p}$, in Eq. 1.5 with the position, $\boldsymbol{r}$, we specify a *real-space* Berry curvature[5] which is then analogous to a magnetic field in co-ordinate space. Dressed state schemes aim to engineer nonzero real-space Berry curvature and hence realise an artificial real-space magnetic field. These schemes have three main characteristics:

1. The system contains two or more internal states that are coupled and split in energy.

[3]The mean vortex density perpendicular to the axis of rotation, n_v, is equivalent to the effective magnetic flux density as $n_v = 2M\Omega/h = |\boldsymbol{B}|q/h$.

[4]Rotating optical lattices will be discussed in Section 2.1.3. There is also promise in recent proposals that discuss how to achieve strongly correlated states using three-body dissipation[83] or deformations of the trapping potential[84], rather than trying to access the centrifugal limit.

[5]Note: real-space and momentum-space Berry curvature are not mutually exclusive.

2. There is an appropriate basis of states with respect to which the particles are moving adiabatically in one state[6]. The effects of Berry curvature arise from adiabatically eliminating all other states. The Schrodinger equation for the remaining state contains the real-space Berry connection[7][42].

3. The state in which the atoms are moving adiabatically varies spatially in such a way that both its real-space Berry connection and curvature are nonzero.

In an ultracold gas, the internal states can be different hyperfine electronic states of the atom[85, 42]. These may have different energies, or their energies can be split by the Zeeman effect in a real magnetic field. The states can then be coupled via optical lasers. As the name of this section suggests, a useful basis is that of the dressed states: the eigenstates of the atom-light coupling. If we assume that interactions are negligible and that the kinetic energy and trap potential are small compared to the dressed state energy spacing, the atoms move adiabatically in a dressed state[85]. These states inherit spatial dependence from the optical coupling, so a nonzero real-space Berry curvature can be achieved with a suitable spatial variation of the coupling lasers.

Let us illustrate the above for the simplest case of a ground, $|g\rangle$, and excited state, $|e\rangle$, coupled by a laser[42]. In the rotating wave approximation, the atom-light coupling has the form:

$$U = \frac{\hbar\Omega_R}{2}\begin{pmatrix} \cos\theta & e^{-i\phi}\sin\theta \\ e^{i\phi}\sin\theta & -\cos\theta \end{pmatrix} \tag{2.2}$$

in the basis $\{|g\rangle, |e\rangle\}$ and where Ω_R is the Rabi frequency, ϕ is the phase of the laser, $\Omega_R\cos\theta$ is the detuning from atomic resonance and $\Omega_R\sin\theta$ is the atom-laser

[6]Isolating a degenerate sub-space of states rather than a single state produces non-Abelian Berry curvature and hence non-Abelian gauge fields, such as spin-orbit coupling (Section 2.2). We also note that the condition of adiabaticity can be relaxed for the optical flux lattices (Section 2.1.3).

[7]The real-space Berry phase is then like the Aharanov-Bohm phase, completing the analogy. Note: in general, there will also be an additional geometric scalar potential, but, for simplicity, we shall not discuss this further here.

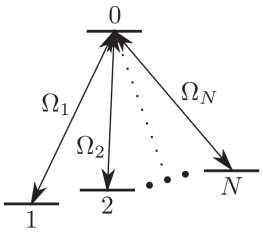

Figure 2.1: A multipod configuration coupling (Figure taken from Ref. [87]). Lasers couple an excited state to N different atomic states. Diagonalising the atom-light interaction leads to the dressed states. There is a $N-1$ manifold of degenerate dark states.

coupling strength. The dressed states are then:

$$|\chi_1\rangle = \begin{pmatrix} \cos(\theta/2) \\ e^{i\phi}\sin(\theta/2) \end{pmatrix}, \qquad |\chi_2\rangle = \begin{pmatrix} -e^{-i\phi}\sin(\theta/2) \\ \cos(\theta/2) \end{pmatrix}. \tag{2.3}$$

Upon adiabatically eliminating $|\chi_2\rangle$, atoms in the dressed state, $|\chi_1\rangle$, experience an artificial magnetic vector potential and field[8]:

$$q\boldsymbol{A}(\boldsymbol{r}) = i\hbar\langle\chi_1|\frac{\partial}{\partial\boldsymbol{r}}\chi_1\rangle = \frac{\hbar}{2}(\cos\theta - 1)\boldsymbol{\nabla}\phi, \qquad q\boldsymbol{B}(\boldsymbol{r}) = q\boldsymbol{\nabla}\times\boldsymbol{A}(\boldsymbol{r}) = \frac{\hbar}{2}\boldsymbol{\nabla}(\cos\theta)\times\boldsymbol{\nabla}\phi \tag{2.4}$$

It is important to note that, as expected, the effective magnetic field, $\boldsymbol{B}(\boldsymbol{r})$, is geometrical: it does not depend on the laser intensity, but only on the spatial variation of the laser through θ and ϕ[42]. For this model, a nonzero effective magnetic field requires that θ and ϕ have nonzero and non-collinear gradients. For the discussion of schemes to implement this model, see the recent review paper Ref. [42] and references within. We also mention that adding weak interactions to such a model can lead to a density-dependent vector potential with novel consequences[86].

An important consideration of this simple scheme is that the dressed state is a weighted combination of $|g\rangle$ and $|e\rangle$. Practically, this requires the rate of spontaneous emission from $|e\rangle$ to be negligible on the time-scales considered, to make the excited state very long-lived and to avoid excessive heating. This assumption is reasonable for the intercombination line of ytterbium or alkaline earth atoms, where this lifetime is typically on the order of seconds or longer[42].

One way to eliminate the contribution from excited states is to use the so-called "dark" state(s)[85, 42]. For the coupling of N ground states to one excited

[8]Note that the definition of the magnetic vector potential and field differ from the Berry connection and curvature by the effective charge, q. We shall use these terms interchangeably in what follows, but this distinction should be kept in mind.

state, there are $N-1$ eigenstates with zero energy which are uncoupled from the excited state and so are robust with respect to spontaneous emission (Figure 2.1). For the "lambda" scheme, $N=2$ and there is a single dark state. As before, the other dressed states can be adiabatically eliminated, leading to an artificial magnetic field and vector potential (similar to Eq. 2.4). Various proposals describe how a non-zero effective magnetic field could be achieved using lasers with orbital angular momentum[88, 89] or spatially shifted light beams[90, 91].

Alternatively, an artificial magnetic field can be realised using two-photon couplings with sufficient detuning from the excited states. Experimentally, this has been achieved with the scheme in Figure 2.2[92]. Instead of a dark state, this scheme uses the lowest dressed eigenstate of the hyperfine basis $\{|m_F{=}1\rangle, |m_F{=}0\rangle, |m_F{=}-1\rangle\}$ for the $F{=}1$ states of ^{87} Rb. Contributions from the excited state manifold are reduced by ensuring that Δ, the single-photon detuning from the manifold, is very large compared to the Rabi frequencies. The real-space Berry curvature for the lowest dressed state can be controlled, for example, through the spatial variation of the two-photon detuning, δ (c.f. the simpler model, Eq. 2.4). This detuning derives from a real magnetic field which Zeeman-shifts the energies of the sublevels, breaking the degeneracy. If the "Zeeman field" is uniform, the effective vector potential is uniform and the effective field is zero[93]. However, if the Zeeman field is inhomogeneous, the detuning varies spatially and the effective magnetic field is nonzero[9][92]. By making the vector potential time-dependent, a synthetic electric field can be generated[95]. However, a key drawback is the significant heating and loss due to spontaneous photon emission[10][94].

Finally, we note the intrinsic difficulty of reaching the strongly correlated regime with these schemes. As mentioned above, the spatial variation in the dressed states derives from the optical coupling fields. Following Ref. [96], if the wavelength of the atom-light coupling is λ, the vector potential will vary smoothly as $|q\boldsymbol{A}| \lesssim h/\lambda$

[9] We note that this experiment can also be discussed within a complementary framework applicable even outside the adiabatic approximation[92, 94]. The adiabatic limit requires that the Rabi frequencies are much larger than the photon recoil energy.

[10] For large detunings, both the photon scattering rate and the two-photon Raman coupling strength decrease approximately as I/Δ^2, where I is the light intensity, for alkali atoms[42]. Therefore while spontaneous photon emission is reduced by increasing the detuning, this comes at the cost of the coupling strength.

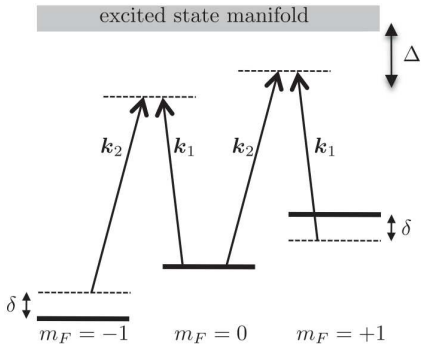

Figure 2.2: Scheme of [92](Figure from Ref. [42]). Two lasers, with wavevectors $\boldsymbol{k}_1$ and $\boldsymbol{k}_2$ couple the F=1 sub-levels in ^{87}Rb. In the two-photon Raman process, an atom absorbs a photon from one beam and emits into the second by stimulated emission. Δ is the single-photon detuning from the excited states and δ is the spatially-varying two-photon detuning.

(see Eq. 2.4). Using Stokes' theorem, this can be related to the mean magnetic flux density, $\bar{n}_\phi$, through a region of sides L_x, L_y:

$$\int n_\phi d^2\boldsymbol{r} = \bar{n}_\phi L_x L_y = \frac{q}{\hbar}\oint \boldsymbol{A}\cdot d\boldsymbol{r} \lesssim \frac{(L_x+L_y)}{\lambda}. \tag{2.5}$$

Then $\bar{n}_\phi \lesssim 1/L\lambda$, where $L = \min(L_x, L_y)$[96]. These schemes are in the continuum, so L is set by the radius of the cloud. For typical values, $L \simeq 10\mu$m and $\lambda \simeq 500$nm, the mean flux density is: $\bar{n}_\phi \lesssim 2\times 10^7 \text{cm}^{-2}$. For strongly correlated physics, the 2D particle density must be comparable to the mean flux density, but this is too low to be experimentally realisable. As we shall now see, much stronger magnetic fields are possible when considering schemes with optical lattices.

2.1.3 Artificial Magnetic Fields With Optical Lattices

Magnetic Fields in Tight-Binding Lattices

Before discussing specific proposals, we briefly review how magnetic fields affect particles in deep lattices. A magnetic vector potential can be incorporated into the Hamiltonian via the substitution: $\boldsymbol{p} \to \boldsymbol{p} - \frac{q}{c}\boldsymbol{A}$. Atoms then gain a Peierls phase factor when tunnelling between sites on a lattice[97]. The phase, θ, can be viewed as the Aharanov-Bohm phase accumulated while tunnelling:

$$\theta_{n,m} = \frac{q}{\hbar}\int_{\boldsymbol{r}_{n,m}}^{\boldsymbol{r}_{n+1,m}} \boldsymbol{A}\cdot d\boldsymbol{s}, \tag{2.6}$$

where $d\boldsymbol{s}$ joins the sites of a 2D lattice and $\boldsymbol{A} = (-By, 0, 0)$: the Landau gauge for a perpendicular magnetic field, $B\hat{\boldsymbol{z}}$. As in Section 1.1.1, this phase is only gauge-

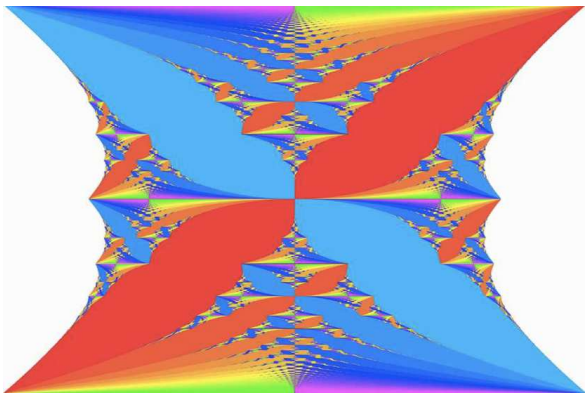

Figure 2.3: The coloured Hofstadter butterfly (Figure from Ref. [98]). The horizontal axis is the chemical potential, while the vertical is the flux per plaquette (running between 0 and 1). For rational flux, (i.e. $n_\phi = p/q$ with $p, q \in \mathbb{N}$), the lowest band splits into q magnetic sub-bands. For non-rational n_ϕ, the spectrum is fractal. Warm colours indicate positive Chern numbers, and cool colours negative.

invariant and physical if we consider hopping around a plaquette (which we now take to be of dimensions $a \times a$). Then:

$$\sum_{\square} \theta_{n,m} = \frac{qBa^2}{\hbar} = 2\pi n_\phi \tag{2.7}$$

where n_ϕ is the flux per plaquette and $\square$ indicates that the sum is around a plaquette. For sufficiently strong lattice potentials, when the bandwidth is much less than the energy gaps between bands, the Hamiltonian can be described by a single-band (non-interacting) tight-binding model:

$$H = -J \sum_{n,m,\pm} e^{\pm i\theta_{n,m}} \hat{a}^\dagger_{n\pm1,m} \hat{a}_{n,m} - J \sum_{n,m,\pm} \hat{a}^\dagger_{n,m\pm1} \hat{a}_{n,m} \tag{2.8}$$

where J is the tunnelling energy, $\hat{a}_{n,m}(/\hat{a}^\dagger_{n,m})$ is the annihilation(/creation) operator for a particle in the spatially localised state at site (n, m). The spectrum is the Hofstadter butterfly[99]. Thouless *et al.*[4] studied this Harper-Hofstadter model in their seminal work on the role of Chern numbers in the quantum Hall effect (Section 1.1.1). This can be visualised by colouring each state in the butterfly according to the quantised Hall conductance (Figure 2.3), revealing a remarkable phase diagram[98]. Many proposals in ultracold gases therefore seek to simulate an artificial magnetic field by engineering the Hamiltonian (Eq. 2.8) directly. The key challenge is to create the appropriate Peierls phase factors in the absence of the Lorentz force.

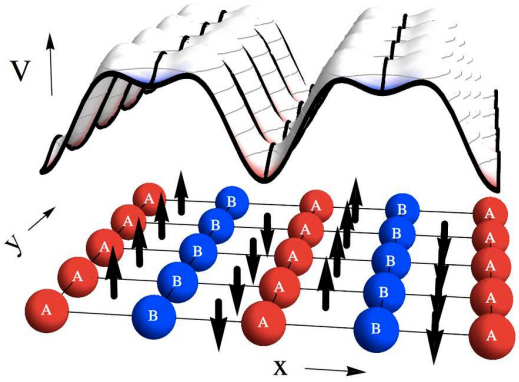

Figure 2.4: Figure from Ref. [103], describing the experiment of Ref. [101]. (Top) The optical lattice potential. There is an energy offset between alternate sites, A and B, along x. This offset is large compared to the bandwidth and so freezes tunnelling along this direction. (Hopping along y is unaffected). A pair of Raman laser beams couple A and B states, turning back on the tunnelling along x. This tunnelling gains a Peierls phase (like Eq. 2.8), which depends on $\delta\boldsymbol{k}$, the difference between the wave-vectors of the Raman beams. By varying the wavelength or angle between the beams, $\delta\boldsymbol{k}$ is varied and the "magnetic flux" is controlled. (Bottom) The arrows indicate the direction of the effective magnetic field. This alternates between sites because the sign of the phase factor switches between $A \to B$ and $B \to A$.

Laser-Assisted Tunnelling in Tight-Binding Lattices

One way to realise complex tunnelling phase factors is to use laser-assisted tunnelling, as first proposed in Ref. [100] and recently experimentally implemented in Refs. [101, 102] (Figure 2.4). Such schemes are able to reach very strong effective magnetic fields. In the experiment of Ref. [101], the magnetic flux density per plaquette[11] is $|n_\phi| = 1/4$. For electrons in condensed matter systems, such high flux densities are inaccessible, and so ultracold gas experiments will open the way for studying many novel phenomena[103].

However, in the experiment of Ref. [101], the artificial magnetic field is also staggered, with the sign of the flux alternating along the direction of laser-assisted tunnelling. Therefore, the spatial average of the magnetic field remains zero. The Bloch band has a Chern number of zero and is topologically trivial. While the Bose-Hubbard model with a staggered magnetic flux can still have novel properties[104,

[11] For comparison to the discussion above, this is of the order $|\bar{n}_\phi| \simeq 1 \times 10^8 \mathrm{cm}^{-2}$. Also note: the phase around a plaquette is defined modulo 2π, so the maximum flux density is $|n_\phi| = 1/2$.

105], there is great interest in extending these schemes to uniform fields where topologically nontrivial bands may be realised. In the new experiment of Ref. [102], the staggered flux was rectified by adding a linear tilt potential[12]; this development will allow experiments to study the Harper-Hofstadter model in ultracold atomic gases.

Optical Flux Lattices

Optical flux lattices provide an alternative route to access strongly correlated fractional quantum Hall physics. The optical flux lattices consist of a state dependent potential in register with an inter-species coupling, and lead to effective magnetic flux with a high non-zero average (with a non-zero integer number of magnetic flux quanta per unit cell)[96, 107, 108, 109]. Optical flux lattices have the advantage of requiring small numbers of lasers, and so can be easier to experimentally implement than other schemes[96]. They also apply outside of the tight-binding limit, i.e. for weaker lattice potentials and lower light intensities, and so suffer less from heating[65].

It is useful to connect optical flux lattices to the dressed states schemes of Section 2.1.2, although we emphasise that these are also valid outside of the adiabatic limit. As we saw in Eq. 2.5, the effective magnetic flux through a unit cell can be expressed as the integral of the real-space Berry connection of the lowest dressed state around the cell. If the Berry connection varies smoothly, this will vanish due to the periodicity of the cell. It will be nonzero only if there are singularities in $\boldsymbol{A}(\boldsymbol{r})$[96]. These singularities are gauge-dependent and contribute to a nonsingular effective magnetic field. (The Berry connection singularities are analogous to Dirac strings for a magnetic monopole[96].) In the optical flux lattices, the atom-light coupling is chosen such that these singularities are present. This allows the realisation of high effective magnetic fields[13].

The specific optical coupling depends on the geometry and atomic species chosen. For atoms with a ground state and long-lived metastable excited state, such

[12]This technique was first proposed in Ref. [100]. Alternatively a uniform flux could be achieved using an additional superlattice with a period of twice the lattice spacing[106].

[13]This can be seen by replacing L in Eq. 2.5 with λ (i.e. the flux density will be of the same order as the tight-binding lattices with laser-assisted tunnelling).

as an alkaline earth atom or ytterbium, a simple one-photon coupling scheme can be implemented[96]. For more commonly used atomic species, such as alkali atoms, two hyperfine states can be used with coupling via two photon processes[107]. In Section 3.3.2, we shall discuss an example of each: the square one-photon optical flux lattice and the $F = 1/2$ two-photon optical flux lattice. The lowest energy band in both lattices can have a Chern number of one and hence be topologically equivalent to the lowest Landau level. Optical flux lattices can also be designed with bands of Chern number greater than one or very narrow topological bands with highly uniform magnetic flux[108]. These narrow bands closely mimic Landau levels and so will be ideal for investigating fractional quantum Hall physics. This has been further explored in recent exact diagonalisation studies, which show that FQH many-body ground states can be realised for particular optical flux lattices with nearly dispersion-less bands[109].

Other Experimental Approaches

While Berry phase schemes rely on a separation of energy-scales, artificial magnetic fields can also be created using a separation of time-scales[110, 111, 112, 113]. An illustrative example is shown in Figure 2.5, where a 1D deep optical lattice is shaken periodically[114]. The period, T, is much shorter than any other timescale of the system, such as the time taken to tunnel between sites. Then the system on long timescales can be described by a time-independent Hamiltonian where the effective hopping gains a Peierls phase due to the shaking[114, 112]. The advantage of such a scheme is that it does not rely on the internal structure of the atoms, and so can be applied to a wide-range of species. In 1D, this Peierls phase is trivial as it can always be gauged away. However, this fast lattice shaking has also successfully been applied in 2D to generate artificial gauge fields and investigate both classical magnetism[111] and Ising-XY models[115] in a triangular lattice. Such schemes can also be generalised to generate non-Abelian gauge fields and topological insulators[116].

Alternatively, a Peierls phase can be introduced by rotating the lattice[76, 117, 118]. As we saw in Section 2.1.1, rotation gives rise to an effective magnetic vector potential, $\boldsymbol{A} \propto \boldsymbol{\Omega}_r \times \boldsymbol{r}$. In the deep lattice regime, this appears as the Peierls phase, as

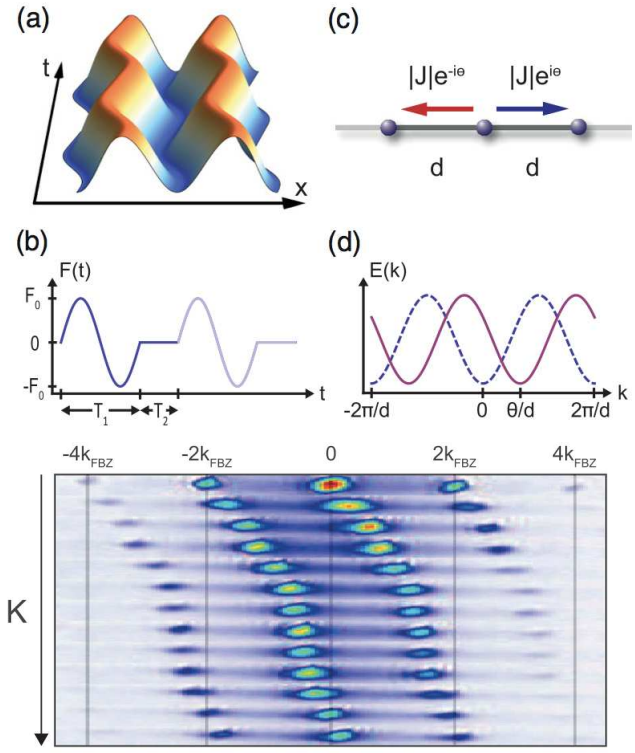

Figure 2.5: Figures taken from Ref. [114]. (a) A 1D lattice is shaken periodically by modulating one of the lattice beams. (b) Resulting periodic inertial force $\boldsymbol{F} = -m\ddot{\boldsymbol{x}}$, where $\boldsymbol{x}(t)$ is the path of the lattice shaking. This force has zero mean so there is no net acceleration of the lattice. By breaking reflection and shift symmetries, the Peierls phase, θ, can be varied smoothly between 0 and 2π by increasing the forcing amplitude, K (for sinusoidal forcing only: $\theta = 0$ or π). (c) The effective tunnellings with complex Peierls phases. (d) The effect of the artificial gauge potential, A, is to shift the single-particle dispersion from $k = 0$ to $k = A/\hbar = \theta/d$ (where d is the lattice spacing). (e) The quasimomentum distribution after 27ms time of flight. As K increases, θ increases and the dispersion minimum shifts[114].

explored experimentally in Ref. [118]. However, there are still key difficulties: there are many particles per vortex, so current experiments are far from the strongly correlated regime and there is significant heating from lattice imperfections and fluctuations[14] [118].

Finally a combination of radio frequency and Raman coupling fields can be

[14]Heating may be reduced by making the artificial magnetic field stationary in the lab-frame. In Ref. [119], it was proposed that a lattice of impurity atoms could be immersed in a rotating BEC. Collisions between the impurity atoms and the condensate atoms create phonons, inducing effective interactions between the impurity atoms. For a rotating condensate, these effective interactions led to Peierls phases for the impurity atoms in the lattice[119].

used to create a 1D "Zeeman" lattice for the $F = 1$ states of ^{87}Rb[120]. Under the rotating wave approximation, the combined fields contribute a "Zeeman"-like term to the Hamiltonian. (Note: there is no additional optical lattice, instead the 1D lattice potential arises from the spatially varying Zeeman energy shift.) This Zeeman-like term can be viewed as arising from an effective magnetic field coupling to $\hat{\boldsymbol{F}}$, the angular momentum operator for $F = 1$. As atoms tunnel between sites, the effective field precesses and atoms gain a Berry phase proportional to the solid-angle enclosed by the precession[15][120]. Tunnelling therefore gains a Peierls phase factor which is controllable through the Raman detuning from resonance. Again, this is only a 1D Peierls phase, but an extension to 2D has been proposed[120].

2.2 Spin-Orbit Coupling in Ultracold Gases

Energy dispersions with nontrivial geometrical properties can also arise in spin-orbit (SO) coupled systems. In particular, we will focus in Section 4.3 on 2D Rashba spin-orbit coupling:

$$H_R = \lambda_R(p_x\hat{\sigma}_y - p_y\hat{\sigma}_x), \tag{2.9}$$

where λ_R is the Rashba coupling and $\hat{\sigma}_{x/y}$ are the Pauli spin-1/2 matrices[16]. This breaks inversion symmetry while preserving time-reversal symmetry. When an external field lifts the degeneracy between the spin states, the energy dispersion has nonzero Berry curvature which can have important consequences. We therefore now introduce spin-orbit coupling in ultracold gases, focusing in particular on how 2D Rashba SO might be experimentally achieved.

Spin-orbit coupling links the spin of a particle to its momentum. In the solid-state, SO interactions are a relativistic quantum effect, arising from the motion of electrons through electric fields such as that of the charged nucleus or the crystal

[15]The geometric phase gained by a spin in a slowly changing magnetic field was first found by Berry in Ref. [9].

[16]In Section 4.3, we also include a Zeeman field to introduce an energy off-set between the spin states. This ensures that the usual Abelian non-degenerate formulation of the momentum-space Berry curvature(Eq. 1.5) can be applied.

field of a material[17]. To give an intuitive argument, an electric field leads to a magnetic field, $\boldsymbol{B}$, in the reference frame of the electron. Therefore the energy gains an additional momentum-dependent Zeeman interaction, $-\boldsymbol{\mu} \cdot \boldsymbol{B}$, where $\boldsymbol{\mu}$ is the magnetic moment of the electron parallel to the spin.

There is great interest in exploring spin-orbit coupling in ultracold atoms as it would allow the simulation of many fascinating condensed-matter phenomena. Spin-orbit interactions have important applications in spintronics and spin quantum computation[121], while most famously, spin-orbit coupling is essential for the quantum spin Hall effect and for many classes of topological insulators[5, 6]. It is expected that adding strong interactions could also lead to fractionalized topological insulators (analogous to the FQH effect) about which little is known[122, 123]. Ultracold gases would therefore provide an important way to learn about these new systems. In addition, spin-orbit coupled ultracold Fermi gases could support novel excitations such as Majorana[124] and Weyl[125] fermions. SO coupling in ultracold gases would also lead to physics with no solid-state analogue[123]. For example, spin-orbit bosons can have a degenerate ground-state, that could exhibit exotic many-body states[126, 123, 127].

2.2.1 Experimental Implementation of 1D Spin-Orbit Coupling

Spin-orbit coupling in ultracold gases cannot be achieved by simply mimicking solid-state physics, as the electric fields required are too high to be created in the laboratory[123]. Instead, experiments use two-photon Raman transitions to couple two internal "spin" states of an ultracold gas (see Figure 2.6 and 2.7)[129]. We note that this coupling can be interpreted as equal-parts Rashba and Dresslhaus. This technique has been successfully applied in both BECs[129, 130] and Fermi gases[131, 132]. However, this approach is limited by spontaneous emission of photons, which will lead to heating or loss. This dispersion also does not have interesting geometrical properties, as the Berry curvature (Eq. 1.5) is zero. Therefore we now turn to schemes for higher-dimensional SO coupling.

[17] In a crystal, SO-coupling requires there to be a broken spatial symmetry. If there is broken inversion symmetry, Rashba SO coupling is possible. If the material is non-centrosymmetric, there can be Dresselhaus SO coupling $\propto (\sigma_x p_x - \sigma_y p_y)$.

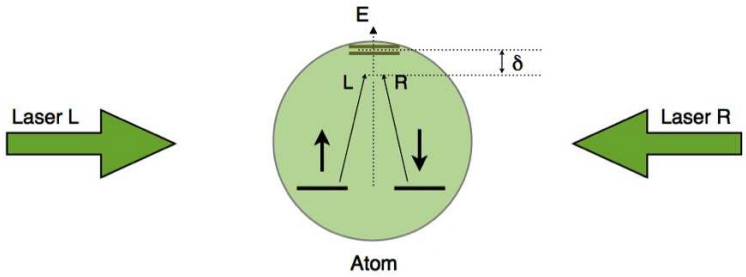

Figure 2.6: Figure from Ref. [128], describing the basic scheme for 1D spin-orbit coupling in an ultracold gas. A two-photon Raman transition couples the two spin states via an excited state (the detuning from resonance is δ). A spin-up atom flips its spin by absorbing a photon from laser L and emitting a photon into laser R. Momentum must also be conserved, as a photon carries a recoil momentum of magnitude $k_R = h/\lambda$. Therefore the Raman process couples states $|\uparrow, k_x{=}q + bk_R\rangle$ and $|\downarrow, k_x{=}q - bk_R\rangle$, where b is a numerical factor depending on laser-beam alignment and we have introduced a mapping onto q, the quasi-momentum. This is a 1D spin-orbit coupling as it depends only on the velocity along x.

2.2.2 Higher-Dimensional Spin-Orbit Coupling in Ultracold Gases

Dressed State Schemes

A series of proposals[133, 134, 87, 135, 136] build on the dressed state schemes for the continuum, as introduced in Section 2.1.2[42]. There, a real-space Berry connection acts as an artificial magnetic vector potential. Unlike magnetic fields, 2D Rashba spin-orbit coupling can be viewed as a non-Abelian gauge field[18]. Therefore, this can be generated by coupling a degenerate manifold of states to make the real-space Berry connection non-Abelian[42] (see Eq. 1.8). As two degenerate states can represent spin-1/2 particles, using more degenerate states would also generalise spin-orbit coupling to larger spins[87]. However, these schemes have disadvantages: some of them are susceptible to decay and relaxation as they do not work with the ground-state[133, 134, 87], while others require many coupling lasers[135, 136].

[18] A non-Abelian gauge field is a field, $\boldsymbol{A}$, with non-commuting components (i.e. $A_x A_y \neq A_y A_x$). For Rashba spin-orbit coupling, this is satisfied because of the non-commutativity of the Pauli spin matrices[137]. Note the 1D spin-orbit coupling described above is Abelian[138].

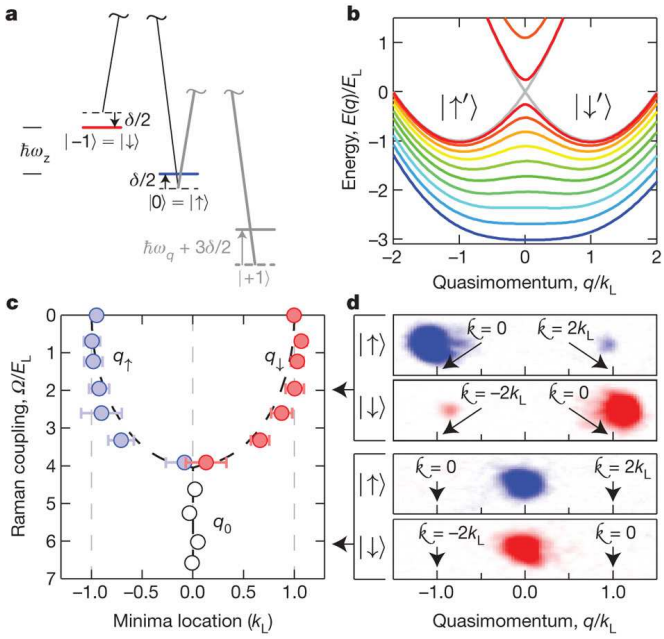

Figure 2.7: Figure taken from Ref. [129]: first experimental realisation of 1D SO coupling. (a) The level diagram. Note the similarities to Figure 2.2; here the $|m_F{=}1\rangle$ state has been neglected due to a large quadratic Zeeman shift, leaving an effective two-level system. (b) The computed energy dispersion for the quasi-momentum, q at $\delta = 0$ and a range of Raman strength couplings, Ω_R ($= 0{-}5E_R$). The grey curve indicates $\Omega_R = 0$, the uncoupled spectrum. At small non-zero coupling, the lower band has two minima at nonzero quasi-momenta, with associated dressed spin states $|\uparrow'\rangle$ and $|\downarrow'\rangle$. For large enough Raman coupling ($\Omega_R > 4E_R$) the double-well merges into a single minimum. (c) Experimentally measured minima corroborating the predicted dispersion. (d) Spin-momentum decomposition. These experimental results clearly show the coupling between spin and momentum.

Taking the 1D Experiment Further

Since the experimental realisation of 1D spin-orbit coupling, theoretical proposals have shown how similar set-ups can be extended to 2D coupling. In Ref. [139], two bichromatic lasers along x and y couple hyperfine states in the $F = 9/2$ manifold of ^{40}K. As in Figure 2.7, an effective two-level system is isolated via the quadratic Zeeman shift. The Raman lasers are reflected to create a periodic coupling, that depends spatially on the phase of the lasers. In the limit of small Raman coupling, the spin-orbit interaction can be tuned between 2D Rashba and Dresselhaus types. Operating at weak Ω_R also reduces heating from spontaneous emission. However, unlike previous schemes, the resulting spin-orbit coupling is not purely geometric;

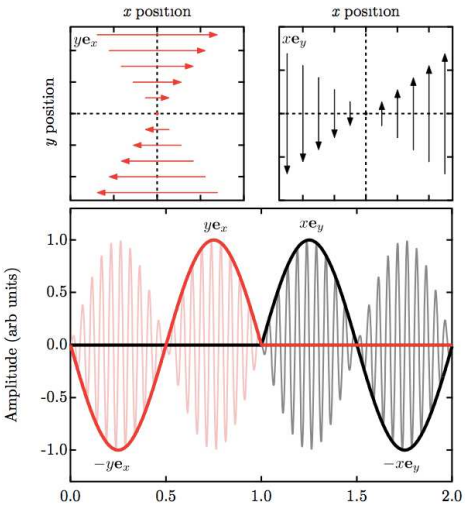

Figure 2.8: 2D Rashba SO-coupling through pulsed inhomogenous magnetic fields (Figure from [141]). The magnetic field, $\boldsymbol{B}$, during one pulse sequence. Top Left: Between $0 \leq t < \tau$, $|\boldsymbol{B}| \propto y\hat{x}$. Top Right: Between $\tau \leq t < 2\tau$, $|\boldsymbol{B}| \propto x\hat{y}$. Bottom: The amplitude modulation of $\boldsymbol{B}$ over the pulse sequence. The net result is to couple the momentum along y with the spin along x during the first half of the sequence and momentum along x and spin along y during the second.

it depends on the laser strength, Ω_R. Therefore SO coupling strength is limited in the regime of operation[139]. Another scheme[140] suggests dynamically switching between pairs of lasers like those used in the 1D experiment of Ref. [129]. By alternating fast pulse sequences and pseudo-spin rotations, the time-averaged effective Hamiltonian will have 2D spin-orbit coupling that is geometrical and is not limited by Ω_R.

Pulsed Inhomogeneous Magnetic Field Gradients

All the schemes discussed so far rely on Raman beams to couple internal states. Key disadvantages of these include the complicated coupling schemes required and the heating and loss associated with spontaneous emission. Recently, two related proposals have shown how these problems might be avoided in a fresh approach, using pulsed magnetic field gradients[142, 141]. For atoms in a (pseudo)spin-F hyperfine manifold, the interaction with a weak magnetic field, $\boldsymbol{B}$, is:

$$H_B(\boldsymbol{r}, t) = g_F \mu_B \boldsymbol{F} \cdot \boldsymbol{B}, \tag{2.10}$$

where $\boldsymbol{F}$ is the spin vector, g_F is the Landé g-factor and μ_B is the Bohr magneton. A magnetic field with a linear gradient[19] therefore imparts a uniform spin-dependent

[19] Linear-gradient magnetic fields cannot exist within an atomic cloud as the divergence and curl of $\boldsymbol{B}$ vanishes in the absence of currents. Refs. [141, 142] both suggest how this problem might be overcome in experiments.

force, coupling momentum and spin as required[141]. Sequential short pulses couple the momentum and spin along different directions. As the pulses are fast, the evolution of the system can then be approximated by an effective 2D spin-orbit coupled Hamiltonian on longer time-scales[141, 142]. An example protocol for generating 2D Rashba spin-orbit coupling is shown in Figure 2.8. These proposals have several other advantages over previous methods. They can implement arbitrary couplings, can be applied to any spin, F, and are straightforwardly generalised to 3D SO couplings. They also do not rely on the quadratic Zeeman shift (see Figure 2.7), which is absent for species with zero nuclear spin, such as ^{52}Cr and ^{164}Dy[142].

Spin-Orbit Coupling in Optical Lattices

Finally we briefly note that non-Abelian gauge fields could be realised in optical lattices by generalising concepts from Section 2.1.3[143, 144, 145, 42]. Previously, we saw that an artificial magnetic vector potential could be simulated via a complex tunnelling in the Hamiltonian, introduced, for example, by laser-induced hopping. A non-Abelian field requires there to be a degenerate manifold of states in the lattice. Then tunnelling is replaced by unitary matrices describing hopping along x and y. To be non-Abelian, these matrices must not commute. The tunnelling can then be interpreted in terms of a non-Abelian vector potential and an artificial spin-orbit coupling[143].

2.3 Summary

In summary, artificial gauge fields in ultracold gases are an important area of current research. Artificial magnetic fields have been realised experimentally in rotating gases, with dressed state schemes in the continuum, and with laser-assisted tunnelling in optical lattices. Furthermore, there are useful theoretical proposals for how to extend these achievements to reach the strongly correlated regime. When time-reversal symmetry is broken, energy bands in optical lattices can have nonzero Chern numbers. This nontrivial topology makes these ideal systems for investigating the novel consequences of Berry curvature discussed in this thesis. In particular, we

take the proposed optical flux lattices as relevant experimental example systems in the following chapters.

The outlook for achieving 2D Rashba spin-orbit coupling in ultracold gases is also promising. There is a great interest in this goal because of the many fascinating effects to be explored. While only 1D spin-orbit coupling has so far been achieved experimentally, there are a wide variety of proposals for achieving this in 2D. We therefore discuss the 2D Rashba Hamiltonian in a Zeeman field in Section 4.3 as a useful system in which to explore the effects of Berry curvature.

Chapter 3

Mapping the Berry Curvature from Semiclassical Dynamics in Optical Lattices

In this chapter, we present a general method for mapping the Berry curvature from the semiclassical dynamics of a wave packet. As introduced in Chapters 1 & 2, ultracold gas experiments can now explore optical lattices with nontrivial topological and geometrical features. This presents an excellent opportunity to study the topology of bands directly. To achieve this, new tools are required to characterise and study the novel properties of the lattices. Here, we propose how experiments would be able to use semiclassical dynamics to map the Berry curvature over the entire Brillouin zone for the first time. This work was published as Ref. [1].

We begin by introducing the Bloch oscillations of a wavepacket, and reviewing how the semiclassical dynamics are modified by the presence of Berry curvature (Section 3.1). We discuss the complications of two-dimensional Bloch oscillations and, in Section 3.2, outline a "time-reversal" protocol to map out the Berry curvature experimentally. We illustrate this discussion with numerical results for the Berry curvature and semiclassical dynamics for three interesting specific models: the asymmetric honeycomb lattice (Section 3.3.1) and two optical flux lattices (Section 3.3.2). In Section 3.4, we discuss general experimental considerations and time-of-flight experiments. Finally, in Section 3.5, we place our work in the context of the

wider field, focusing on important developments since our publication, such as the experimental measurement of the Zak phase using a similar method[146].

3.1 The Semiclassical Dynamics of a Wavepacket

The Semiclassical Dynamics of a Wavepacket without Berry curvature

To describe semiclassical dynamics, we consider a gas of non-interacting fermions or bosons that is prepared in a wavepacket with a centre of mass at position, $\boldsymbol{r}_c$, and momentum, $\boldsymbol{k}_c$ [147, 148]. For atoms initially prepared in the bottom of the lowest band, the temperature contributes to the initial momentum spread of the atoms. We therefore assume that the temperature is less than the bandwidth so that the wavepacket does not cover the whole Brillouin zone.

We consider the wavepacket under a constant external force, $\boldsymbol{F}$. In a solid state system, this force would usually be due to an electric field. However, ultracold gases are neutral, and this force may instead come from linearly accelerating the lattice[148, 149], from gravity[150, 151, 152, 153] or from a real magnetic field gradient [146]. It is assumed that the force is sufficiently small that the motion is adiabatic and that the atoms remain in the lowest band. This means that the rate of Landau-Zener tunnelling to the next lowest band must be small. The probability of a Landau-Zener transition where the bands almost touch is given by [154]:

$$p = e^{-a_c/a_F} \tag{3.1}$$

where a_F is the acceleration of the atoms moving under the external force, $a_c = (\delta E)^2\lambda/8\hbar^2$, λ is the optical wavelength and δE is the bandgap. This can therefore be neglected when the force is small or the bandgap is large.

The semiclassical equations of motion are [147]:

$$\begin{aligned} \dot{\boldsymbol{r}}_c &= \frac{1}{\hbar}\frac{\partial E(\boldsymbol{k}_c)}{\partial \boldsymbol{k}_c} \\ \hbar\dot{\boldsymbol{k}}_c &= \boldsymbol{F}. \end{aligned} \tag{3.2}$$

Under a constant force, $\boldsymbol{F}$, the wavepacket will execute Bloch oscillations. Bloch oscillations have not been observed for bulk crystalline electrons due to electronic scattering off lattice defects, but they have been seen in other physical systems including semiconductor superlattices [155] and ultracold gases [148, 150].

To demonstrate how Bloch oscillations arise from Equation 3.2, let us consider the motion of a wavepacket in a one-dimensional (1D) lattice. The momentum of the wavepacket evolves as $k_c(t) = k_c(0) + Ft/\hbar$. However, the crystal momentum lies within the Brillouin zone: $k_c \in]-\pi/a, \pi/a]$. Therefore, the evolution will have a periodicity, $\tau_B = h/(Fa)$ (where a is the lattice constant); this is the time taken for the wavepacket to evolve across the whole Brillouin zone. In real space, the wavepacket will perform periodic Bloch oscillations.

The Semiclassical Dynamics of a Wavepacket with Berry Curvature

The equations of motion are crucially modified by Berry curvature [23]:

$$\begin{aligned} \dot{\boldsymbol{r}}_c &= \frac{1}{\hbar}\frac{\partial E(\boldsymbol{k}_c)}{\partial \boldsymbol{k}_c} - (\dot{\boldsymbol{k}}_c \times \hat{\boldsymbol{z}})\Omega(\boldsymbol{k}_c), \\ \hbar\dot{\boldsymbol{k}}_c &= \boldsymbol{F}. \end{aligned} \tag{3.3}$$

We shall refer to the first term in Eq. 3.3 as the group velocity and to the second as the Berry velocity[1]. We note that these semiclassical equations are further modified if there is an external "magnetic" field[23] in addition to the external force $\boldsymbol{F}$. We shall not discuss this further here, assuming that any magnetic field has the periodicity of the lattice and is incorporated into the bandstructure through the (magnetic) Bloch states $|n\boldsymbol{k}\rangle$ (see Section 3.3.2). The effect of a magnetic field on Bloch oscillations has also been analysed directly from the tight-binding Hamiltonian in Refs. [157, 158]. Equations 3.3 were first derived using the Lagrangian formalism for a semiclassical wavepacket[23]. Recently a more transparent and elementary derivation has been presented for the Harper-Hofstadter model[2] in an external electric field[156].

[1] We note that there exist variants of these equations in the literature with different signs [156, 12]. We believe this to be the correct version as stated in [23].

[2] This model was introduced briefly in Section 2.1.3.

To theoretically simulate the semiclassical dynamics, we must be able to calculate the Berry curvature. In general, a simple analytic expression is not possible and the Berry curvature is calculated numerically. This requires a discretised version of (1.5), as eigenfunctions are found computationally over a grid in k-space. There is an inherent phase ambiguity in the Bloch states, and so a gauge must be chosen to calculate the Berry connection. The Berry curvature is gauge-invariant, and can be found on this grid by the method of Fukui *et al.*[159], which applies a geometrical formulation of topological charges in lattice gauge theory, where the Berry curvature is calculated from the winding of $U(1)$ link variables around each plaquette in the Brillouin zone. We have used this method throughout this chapter for the numerical calculations.

It is of interest to note that the effects of Berry curvature also arise in the semiclassical dynamics of a wavepacket in a time-dependent one-dimensional optical lattice [12, 113, 160]. The Berry curvature is then defined over a 2D parameter space made up of the one-dimensional quasi-momentum and time. The Bloch oscillations of a wavepacket in such a potential were theoretically studied in Ref. [160].

3.1.1 Lissajous-like Bloch Oscillations in 2D

The pioneering experiments on Bloch oscillations in ultracold gases were (quasi-)one dimensional [148, 150], and only recently has the extension to 2D been investigated [70]. In 2D, Bloch oscillations have various interesting features in their own right, even before the Berry curvature is considered.

One important consequence of dimensionality is that the real-space Bloch oscillations in 2D become Lissajous-like [161, 162, 163]. For separable potentials, 1D Bloch oscillations along the x and y axes are simply superposed. For an arbitrary force $\boldsymbol{F} = (F_x, F_y)$, the wavepacket's motion is periodic along k_i with periods $\tau_{Bi} = h/|F_i|a$ (where i runs over x,y). The ensuing motion depends on the ratio $F_x : F_y$.

We illustrate this with the example of a wavepacket in a simple dispersion:

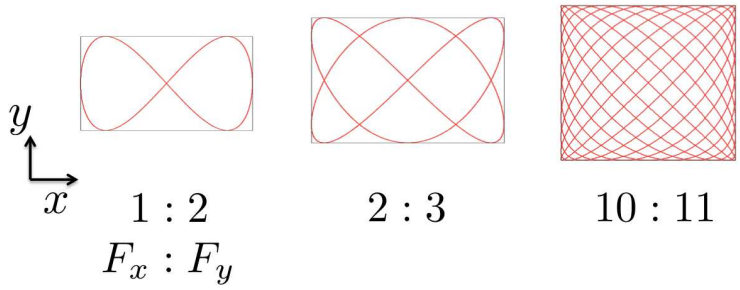

Figure 3.1: The real space motion of a wavepacket in the energy dispersion, $E(\boldsymbol{k}_c) = -2J[\cos k_x a + \cos k_y a]$, under a constant external force. The trajectories are shown for three different ratios of $F_x : F_y$. (The figures are not to the same scale). These are Lissajous curves and even for a simple 2D energy dispersion, the resulting trajectories can be complicated.

$E(\boldsymbol{k}_c) = -2J[\cos k_x a + \cos k_y a]$, where $2J$ is the bandwidth. The velocity is:

$$\dot{\boldsymbol{r}}_c = \frac{1}{\hbar}\frac{\partial E(\boldsymbol{k}_c)}{\partial \boldsymbol{k}_c} = \frac{2Ja}{\hbar}(\sin k_x a, \sin k_y a) = \frac{2Ja}{\hbar}\left(\sin\frac{F_x t a}{\hbar}, \sin\frac{F_y t a}{\hbar}\right). \quad (3.4)$$

In Figure 3.1, we show the corresponding trajectories for different ratios of $F_x : F_y$. Each trajectory will have a bounding box of lengths: $2J/|F_i|$, or more generally, the ratio of the bandwidth to the component of the force. For nonseparable potentials, studies show that similar behaviour can be expected when the force applied is weak and Landau-Zener tunnelling is negligible [161, 162]. Figure 3.2 gives one such example for the experimentally-relevant square optical flux lattice (Section 3.3.2).

The real-space Bloch oscillations can therefore be complicated two-dimensional Lissajous-like figures. For the Berry curvature to change this trajectory significantly, it would be necessary to wait until the wavepacket drifts outside of the bounding box. As a result, experiments would measure only the net Berry curvature encountered along a path. Information would be lost about how the Berry curvature is distributed in momentum space and notably whether its sign changes.

Furthermore, in 2D there can be an additional drift in the wavepacket's position, independent of the Berry curvature, if the wavepacket does not start at high symmetry points such as the zone centre $\boldsymbol{k}_0 = (0, 0)$ [163, 164]. Thus, merely observing a transverse drift is not, by itself, conclusive evidence of nonzero Berry curvature.

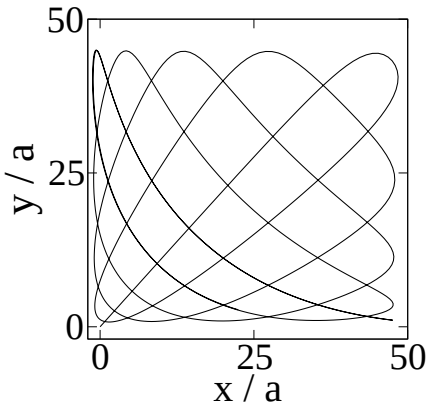

Figure 3.2: An example of a Lissajous-like figure for the square optical flux lattice (Section 3.3.2). The ratio $F_x : F_y$ is 9 : 10, and a low force of $|\boldsymbol{F}| = 0.05F_R$ is used to minimise the effects of Berry curvature over one oscillation ($F_R = h^2/2m\lambda^3$ where λ is the optical wavelength and m is the mass of the atomic species). The Lissajous-like figure is approximately bounded by the Bloch oscillation lengths, and so it obscures the effects of Berry curvature within this box.

3.2 A "Time Reversal" Protocol to Extract The Berry Curvature

Berry curvature effects can be isolated by considering the dynamics under a reversal of "time". In doing so, it is important to be able to measure the velocity of the wavepacket. We shall discuss in Section 3.4 how this may be done in experiments: for instance through tracking the position of the wavepacket in real space or through the momentum distribution, as in the seminal paper of Ben Dahan *et al.*[148].

We consider first measuring the velocity for a given force, $\boldsymbol{F}$, at a particular point, $\boldsymbol{k}$, in the Brillouin zone. This can be achieved in an experiment in which the wavepacket has evolved according to $\boldsymbol{k}(t) = \boldsymbol{k}(0) + \boldsymbol{F}t/\hbar$. This velocity is uniquely defined (within the single band approximation) at each point $\boldsymbol{k}$ along the trajectory and we denote it as $\boldsymbol{v}_{\boldsymbol{k}}(+\boldsymbol{F})$. We now consider measuring the velocity in an experiment in which the wavepacket passes through the same point $\boldsymbol{k}$, but with opposite direction of the force, $-\boldsymbol{F}$, which we denote $\boldsymbol{v}_{\boldsymbol{k}}(-\boldsymbol{F})$. This can be achieved, for example, by evolving along the line $\boldsymbol{k}(0) + \boldsymbol{F}t/\hbar$ for a time T that moves past the point of interest (e.g. to the Brillouin zone boundary), and then retracing this path using the reversed force $-\boldsymbol{F}$. From (3.3), we can see that the Berry velocity

changes sign, while the group velocity remains invariant. The two effects can then be separated:

$$\boldsymbol{v}_{k}(+\boldsymbol{F}) - \boldsymbol{v}_{k}(-\boldsymbol{F}) = -\frac{2}{\hbar}(\boldsymbol{F} \times \hat{\boldsymbol{z}})\Omega(\boldsymbol{k}) \tag{3.5}$$

$$\boldsymbol{v}_{k}(+\boldsymbol{F}) + \boldsymbol{v}_{k}(-\boldsymbol{F}) = \frac{2}{\hbar}\frac{\partial E(\boldsymbol{k})}{\partial \boldsymbol{k}} \tag{3.6}$$

This transformation is equivalent to a time reversal operation, and it cleanly removes the effects of the complex Lissajous-like figures in 2D.

The Berry curvature can now be found at each point along the wavepacket's path. By varying the path across the whole Brillouin zone, the Berry curvature is mapped out and the Chern number is directly measured. The path of the wavepacket may be chosen in various ways, two of which are illustrated in Figure 3.3. Firstly, the alignment of the force with the lattice may be rotated so that different trajectories are successively explored. In such a scheme, the measurement time can be short, corresponding to the time taken for the wavepacket to travel once across the Brillouin zone. However, it would be important to align the force precisely each time. An alternative scheme would be to make the ratio $F_x : F_y$ large. The wavepacket will cover a large area of the Brillouin zone during a single Bloch oscillation. The force needs to be aligned only twice (for $+\boldsymbol{F}$ and $-\boldsymbol{F}$) but longer measurement times would be required. A combination of these methods may be most suitable.

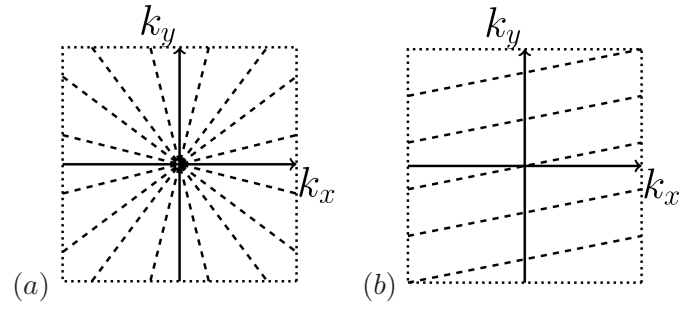

Figure 3.3: Two methods for mapping the Brillouin zone. (a) Rotating the force with respect to the lattice between experiments allows each wavepacket to travel a different path. (b) With a large ratio $F_x : F_y$, a single wavepacket successively travels many paths within the Brillouin zone.

3.2.1 Relation to the Chern Number

By this approach, measurements of the velocity of the wave packet can be used to extract the Berry curvature. Measurements of the net drift of the wave packet in position space can be used to measure the Chern number of the band. To illustrate the idea, it is convenient to consider a BZ of rectangular symmetry, and the set of paths $\boldsymbol{k} = (0, k_y) \to (K_x, k_y)$ that are traced out by a force $+F$ in the x-direction, for different values of the initial wave vector k_y. Here K_x denotes the size of the reciprocal lattice vector in the x direction, so the path traverses the full width of the Brillouin zone once. The net drift of the wave packet in the y direction, $\Delta y = \int v_y dt$, is:

$$\Delta y(k_y, +F) = \int_0^{K_x} \frac{1}{F}\frac{\partial E}{\partial k_y} dk_x + \int_0^{K_x} \Omega(k_x, k_y) dk_x. \tag{3.7}$$

Note that, for general k_y, there is a transverse displacement not only from the Berry curvature but also from the group velocity[163, 164]. Reversing the force, such that the set of paths run in the opposite direction, over $\boldsymbol{k} = (0, k_y) \to (-K_x, k_y)$, the displacement becomes:

$$\Delta y(k_y, -F) = \int_0^{K_x} \frac{1}{F}\frac{\partial E}{\partial k_y} dk_x - \int_0^{K_x} \Omega(k_x, k_y) dk_x. \tag{3.8}$$

Thus, the contribution from the group velocity stays the same, but the contribution from the Berry curvature changes sign. Averaging the difference:

$$\frac{\Delta y(k_y, +F) - \Delta y(k_y, +F)}{2} = \int_0^{K_x} \Omega(k_x, k_y) dk_x \tag{3.9}$$

extracts the part that depends on the Berry curvature. It is interesting to note that this contribution is independent of the magnitude of the force. The size of the transverse displacement is just set by the length scale of the underlying lattice (the lattice constant), and a numerical factor that involves the average Berry curvature along the trajectory. Furthermore, the total Chern number can be found by summing over the set of trajectories with different values of k_y, which can be used to represent an evaluation of the integral:

$$C = \frac{1}{2\pi} \int_0^{K_y} dk_y \int_0^{K_x} dk_x \Omega(k_x, k_y) \tag{3.10}$$

at discrete points in k_y. (Clearly this approach can be readily adapted to a lattice of any symmetry, provided the set of paths spans the entire Brillouin zone once.)

Note that, if instead of a wavepacket, the band is filled (e.g. by non-interacting fermions) the Chern number may be measured from the net current density when a force, $\boldsymbol{F}$, is applied:

$$\boldsymbol{J} = \frac{1}{2\pi h}\int_0^{K_y} dk_y \int_0^{K_x} dk_x \Omega(k_x, k_y)(\boldsymbol{F} \times \hat{\boldsymbol{z}}) = \frac{C}{h}(\boldsymbol{F} \times \hat{\boldsymbol{z}}). \tag{3.11}$$

For a trapped gas, this result can be applied locally, with $\boldsymbol{F}$ set by the local potential gradient to give equilibrium currents.

3.3 Example Systems

In this section, we illustrate our proposed method for measuring the Berry curvature for three example systems that are of experimental interest: the asymmetric hexagonal lattice; and two optical flux lattices[96, 107] for which the Chern number is nonzero.

The magnitude of the external force significantly affects the dynamics, as discussed further in Section 3.4. In previous experiments, the force has been introduced by linearly accelerating the lattice [148, 149], where the magnitude can be varied, or by gravity [150, 151, 152, 153]. In our units, $|m\boldsymbol{g}| = 0.7F_R$ for ^{174}Yb and for $\lambda = \lambda_0 \approx 578$ nm, the resonance wavelength coupling the ground and excited state in ^{174}Yb [106]. This choice of parameters is especially relevant to the optical flux lattices discussed below. We therefore primarily focus on the representative case $|\boldsymbol{F}| = 1F_R$. We also note that, as discussed above, the rate of Landau-Zener tunnelling must be small for the evolution to be adiabatic (Eq. 3.1).This will be the case when the force is small or the bandgap is large.

3.3.1 The Asymmetric Hexagonal Lattice

The tight-binding hexagonal lattice has long been studied in condensed matter physics as a simple model for graphene [73]. Thanks to recent advances, optical

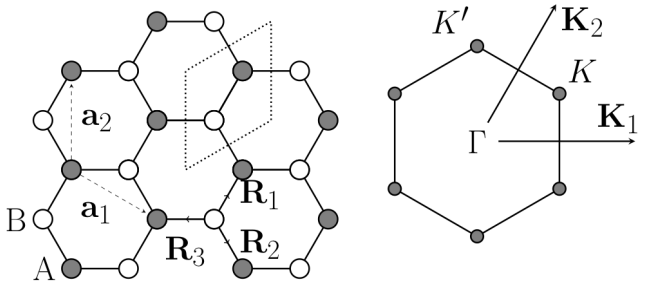

Figure 3.4: The asymmetric hexagonal lattice in real space (on the left) and reciprocal space (on the right). The real space lattice vectors are $\boldsymbol{a}_1 = a(\sqrt{3}/2, -1/2)$ and $\boldsymbol{a}_2 = a(0, 1)$ where a is the lattice spacing (and for this geometry, $a = 2\lambda/3$). The sublattices are connected by $\boldsymbol{R}_1 = a(1/2\sqrt{3}, 1/2)$, $\boldsymbol{R}_2 = a(1/2\sqrt{3}, -1/2)$ and $\boldsymbol{R}_3 = a(-1/\sqrt{3}, 0)$. The dotted lines indicate the unit cell. The reciprocal lattice vectors are then $\boldsymbol{K}_1 = (4\pi/\sqrt{3}a)(1, 0)$ and $\boldsymbol{K}_2 = (4\pi/\sqrt{3}a)(1/2, \sqrt{3}/2)$.

lattices of hexagonal symmetry (or closely related forms) can be imposed on ultracold gases and phenomena associated with the interesting band topology can be directly studied [69, 70, 165] (Section 1.2.3).

In the presence of both inversion and time-reversal symmetry, the bands touch at two Dirac points in the corners of the hexagonal Brillouin zone. If either of these symmetries is broken, band gaps open and Berry curvature appears at these points, as in the Haldane model where time reversal symmetry is broken [166]. The Chern number has also been observed experimentally for time-reversal symmetry breaking in graphene [167, 168].

The asymmetric hexagonal lattice instead breaks inversion symmetry by introducing an onsite energy difference between the two lattice sites, A and B. The opening of band gaps with asymmetry has already been studied experimentally in graphene[169], but Berry curvature effects have not been observed directly. Theoretically, the Berry curvature can lead to a quantum valley Hall effect, which may be useful for valley-based electronic applications [73, 170, 12]. It would therefore be of great interest to study this system in ultracold gases, where it is already very relevant to current experiments (see Section 1.2.3).

The honeycomb lattice can be viewed as two interpenetrating triangular sublattices, for A and B, each with one site per unit cell (Figure 3.4). With onsite

energies of $\pm W$ on A/B sites, and including only nearest neighbour hoppings, the Hamiltonian is:

$$H(\boldsymbol{k}) = \begin{pmatrix} W & V(\boldsymbol{k}) \\ V^*(\boldsymbol{k}) & -W \end{pmatrix} \tag{3.12}$$

where $V(\boldsymbol{k}) = -J[e^{i\boldsymbol{k}\cdot\boldsymbol{R}_1} + e^{i\boldsymbol{k}\cdot\boldsymbol{R}_2} + e^{i\boldsymbol{k}\cdot\boldsymbol{R}_3}]$. The two energy bands are then:

$$E(\boldsymbol{k}) = \pm\sqrt{W^2 + |V(\boldsymbol{k})|^2}\,. \tag{3.13}$$

For $W = 0$, the energy bands have two Dirac points at which $|V(\boldsymbol{k})| = 0$: these are at $\boldsymbol{k} = (4\pi/\sqrt{3}a)(1/2, 1/2\sqrt{3})$ and $\boldsymbol{k} = (4\pi/\sqrt{3}a)(0, 1/\sqrt{3})$ which we label as K and K'. Near each of the Dirac points, the effective Hamiltonian takes a simple form. Close to the Dirac point K, writing $\boldsymbol{k} = (4\pi/\sqrt{3}a)(1/2, 1/2\sqrt{3}) + \boldsymbol{q}$, the effective Hamiltonian is:

$$H(\boldsymbol{q}) = \begin{pmatrix} W & -\hbar v_F(q_x - iq_y) \\ -\hbar v_F(q_x + iq_y) & -W \end{pmatrix} \tag{3.14}$$

where $\hbar v_F = (\sqrt{3}/2)aJ$: a Dirac equation with mass. The bandstructure is shown in Figure 3.5(a) for $W = 0.5E_R$ and $J = 1.0E_R$. For this value of W, the bandgap at the Dirac points is $1.0E_R$ and the Landau-Zener tunnelling probability is less than 0.05 for $|\boldsymbol{F}| = m\boldsymbol{g}$ or less than 0.09 for $|\boldsymbol{F}| = 1F_R$. Near the Dirac point, the Berry curvature is [12]:

$$\Omega(\boldsymbol{q}) = \frac{\hbar^2 v_F^2 W}{2(W^2 + \hbar^2 v_F^2 q^2)^{3/2}} \tag{3.15}$$

For the Dirac point K', writing $\boldsymbol{k} = (4\pi/\sqrt{3}a)(0, 1/\sqrt{3}) + \boldsymbol{q}$, the Berry curvature has the same form but opposite sign.

The resulting map of Berry curvature for the asymmetric hexagonal lattice is displayed in Figure 3.5(b). This was previously found analytically in Ref. [171]. The Berry curvature around points K and K' has opposite signs such that the net Chern number of the band is zero. This vanishing Chern number is required by the fact that the system is time-reversal invariant.

From the Berry curvature and bandstructure, we can now calculate the semi-classical motion of a wavepacket in this system (Figure 3.6). To illustrate clearly

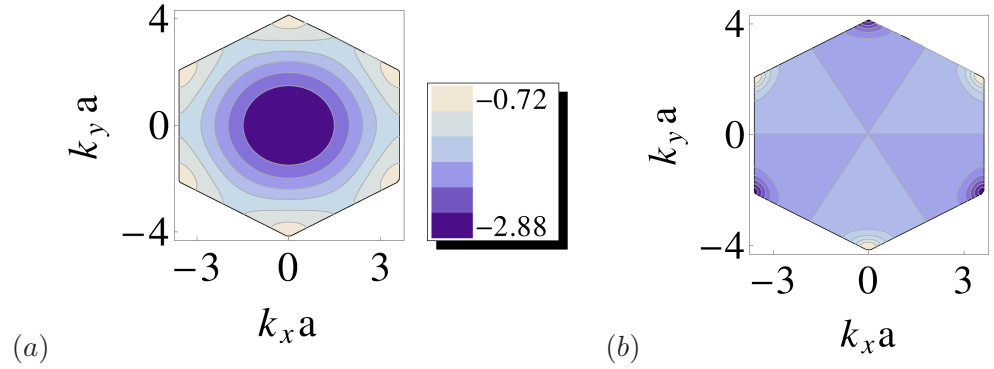

Figure 3.5: (a) Bandstructure of the lowest band of the asymmetric hexagonal lattice for $W = 0.5E_R$ and $J = 1.0E_R$, and the energy in units of E_R (for this geometry, $a = 2\lambda/3$). Due to the asymmetry, gaps have opened at the Dirac points at the corners of the Brillouin zone. (b) The Berry curvature mapped out for $W = 0.5E_R$, using the method of Ref. [159]. Light shading indicates $\Omega > 0$ and dark shading indicates $\Omega < 0$. Positive and negative regions cancel, giving a net Chern number of zero.

the effects of Berry curvature, we start the wavepacket at $\boldsymbol{k} = (0, 0)$ and consider a force aligned along the y-direction, so that the 2D Bloch oscillation is also simply directed along y. This real space trajectory was previously obtained in Ref. [172], where the effects of a perturbing "magnetic" field were also discussed.

The velocities along x and y are shown in Figure 3.7. As the wavepacket passes through K', the negative Berry curvature gives it a positive velocity in the x direction. In between K' and K, there is no curvature and it moves with a group

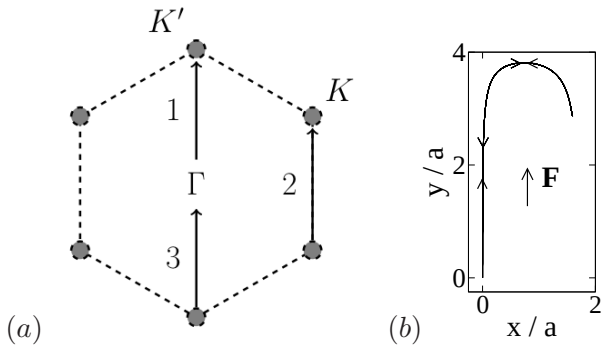

Figure 3.6: (a) The trajectory of a semiclassical wavepacket through the Brillouin zone, starting from $\boldsymbol{k} = (0, 0)$ with $\boldsymbol{F} = (0.0, 1.0F_R)$. The numbers indicate the order in which the path is travelled. (b) The corresponding real-space trajectory of the wavepacket, starting from the origin, for $W = 0.5E_R$. This result was previously obtained in Ref. [172]. The motion along x is due to the Berry curvature, while that along y is due to the bandstructure.

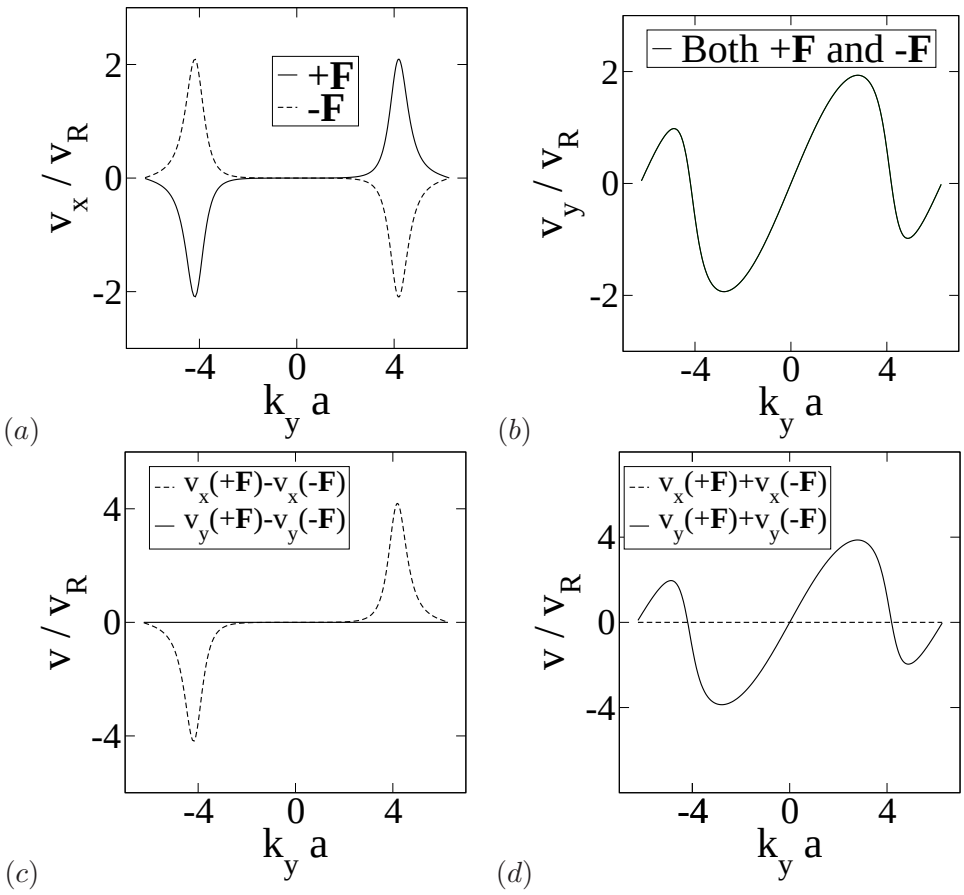

Figure 3.7: (a) Velocity along x of a wavepacket moving under the force $\boldsymbol{F} = \pm(0.0, 1.0F_R)$ with $W = 0.5E_R$. k_y is measured along the path travelled (which is periodic in 4π). (b) Velocity along y. (c) Applying the time-reversal protocol to extract the Berry velocity: $\boldsymbol{v}(+\boldsymbol{F}) - \boldsymbol{v}(-\boldsymbol{F}) = -2/\hbar(\boldsymbol{F} \times \hat{\boldsymbol{z}})\Omega(\boldsymbol{k})$. (d) Applying the time-reversal protocol to extract the group velocity: $\boldsymbol{v}(+\boldsymbol{F}) + \boldsymbol{v}(-\boldsymbol{F}) = (2/\hbar)\partial\epsilon(\boldsymbol{k})/\partial\boldsymbol{k}$

velocity along y. When it passes through K, the positive curvature gives it negative x velocity. As the regions of curvature have the same magnitude, the effects cancel and there is no net drift.

For $\boldsymbol{F} = (0, F)$ it is simple to determine the Berry curvature because the group and Berry velocities are perpendicular. For more general directions of the force, Lissajous-like oscillations will make it difficult to extract any information about the Berry curvature from the real space motion.

As proposed above, the Berry curvature may be cleanly mapped from the velocities using a time-reversal protocol. This is illustrated in Figure 3.7(c) and (d). Here the velocities along x and y for $+\boldsymbol{F}$ and $-\boldsymbol{F}$ are combined to show the Berry velocity and the group velocity respectively.

3.3.2 Optical Flux Lattices

One of our main motivations for mapping the Berry curvature is to find a way of experimentally characterising optical flux lattices. These have been introduced in Section 2.1.3, as schemes to access fractional quantum Hall physics in ultracold gases [96, 107, 109]. Here we discuss the one-photon square optical flux lattice, which would be suitable for alkaline earth atoms or ytterbium, and the $F = 1/2$ two-photon scheme for alkali atoms.

One-Photon Square Optical Flux Lattice

In this scheme, the electronic ground state and a long-lived excited state are coupled via a single photon process[106]. The Hamiltonian in the rotating wave approximation is:

$$\hat{H} = \frac{\boldsymbol{p}^2}{2m}\hat{1} + \hat{V}(\boldsymbol{r}), \tag{3.16}$$

where $\hat{1}$ and $\hat{V}$ are 2×2 matrices acting on the two internal states of the atom. We neglect interactions, an assumption that is discussed further in Section 3.4. The square optical flux lattice is generated when [96]:

$$\hat{V}_{sq} = V(\cos(\kappa x)\hat{\sigma}_x + \cos(\kappa y)\hat{\sigma}_y + \sin(\kappa x)\sin(\kappa y)\hat{\sigma}_z) \tag{3.17}$$

where V sets the energy scale of the potential, $\kappa = 2\pi/a$ and the lattice vectors are $\boldsymbol{a}_1 = (a, 0)$, $\boldsymbol{a}_2 = (0, a)$. The flux density is everywhere of the same sign, and leads to a total flux per unit cell of $N_\phi = 2$ [96].

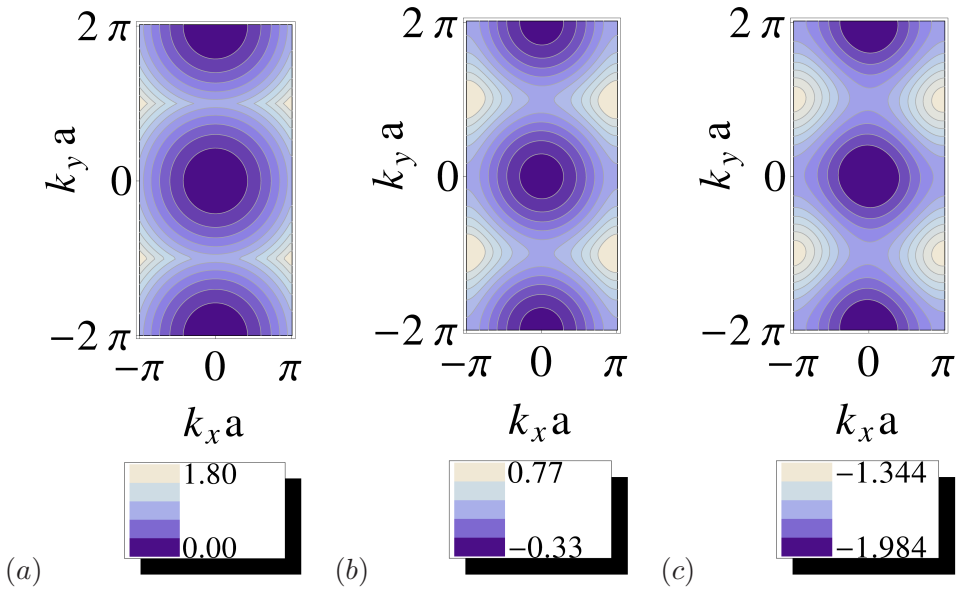

Figure 3.8: Bandstructure of the lowest band in the magnetic Brillouin zone for the one-photon square optical flux lattice with (a) $V = 0.0E_R$, (b) $V = 1.0E_R$ and (c) $V = 3.0E_R$, and the energy in units of E_R. At $V = 0.0E_R$, the lowest band touches the second lowest band at $k = (\pi/a, \pm\pi/a)$. As V is turned on, band gaps open at these points and Berry curvature is formed.

We consider the regime where $V \lesssim \hbar^2\kappa^2/2m = 4E_R$ (for this geometry $a = \lambda/2$). We expand the periodic Bloch functions over a set of reciprocal lattice vectors, $\boldsymbol{K}$:

$$u_{n,\boldsymbol{k}}(\boldsymbol{r}) = \frac{1}{\sqrt{N}} \sum_{\boldsymbol{K}} e^{-i\boldsymbol{K}\cdot\boldsymbol{r}} \begin{pmatrix} c_{\boldsymbol{K}}^{1(n,\boldsymbol{k})} \\ c_{\boldsymbol{K}}^{2(n,\boldsymbol{k})} \end{pmatrix} \tag{3.18}$$

and diagonalise the resulting Hamiltonian to find the bandstructure. As we consider low V, a small, finite set of $\boldsymbol{K}$ vectors will give the eigenfunctions and values to within the required numerical accuracy.

The eigenfunctions are everywhere two-fold degenerate, corresponding to two magnetic sub-bands. To distinguish between these states, we reinterpret the system within the magnetic Brillouin zone (MBZ) [173, 23, 96]. The optical coupling is

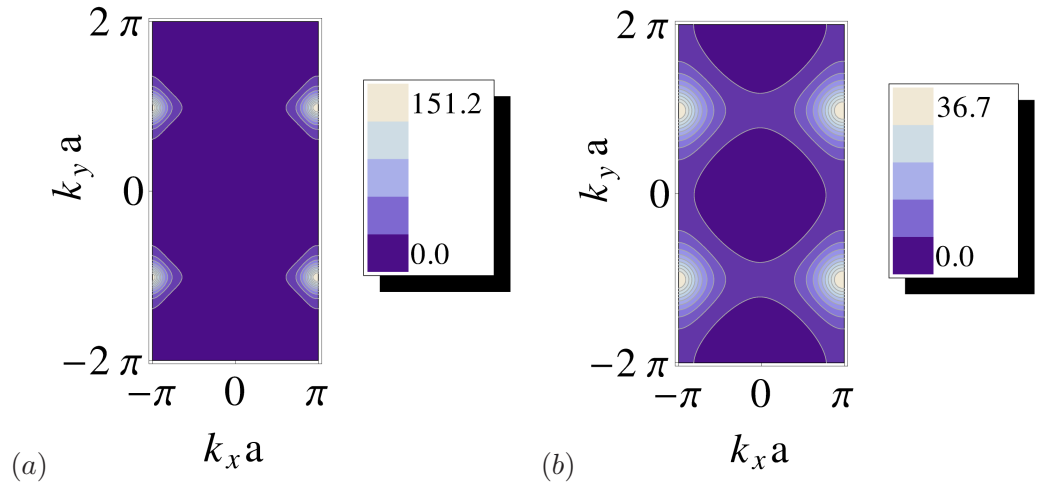

Figure 3.9: Contour maps of the Berry curvature, $\Omega(\boldsymbol{k})$, for the square optical flux lattice when (a) $V = 1.0E_R$ and (b) $V = 3.0E_R$. Ω is in units of 1/[MBZ area] $= a^2/8\pi^2$. Ω is concentrated at points $k = (\pi/a, \pm\pi/a)$, spreading out with increasing V.

invariant under the magnetic translation operators:

$$\hat{T}_1 \equiv \hat{\sigma}_y e^{\frac{1}{2}\boldsymbol{a}_1\cdot\nabla} \qquad \hat{T}_2 \equiv \hat{\sigma}_x e^{\frac{1}{2}\boldsymbol{a}_2\cdot\nabla} \tag{3.19}$$

which do not commute but satisfy $\hat{T}_2\hat{T}_1 = -\hat{T}_1\hat{T}_2$. These operators represent rotations in spin space and translations by $\frac{1}{2}\boldsymbol{a}_{1,2}$, which enclose half a flux quantum (as $N_\phi = 2$) [96, 173]. The magnetic Brillouin zone is defined by a unit cell containing an integer number of flux [173]; we choose a cell containing a single flux with vectors $\boldsymbol{a}_1$ and $\boldsymbol{a}_2/2$. The corresponding commuting operators are $\hat{T}_1^2$ and $\hat{T}_2$, with eigenvalues $e^{i\boldsymbol{k}\cdot\boldsymbol{a}_1}$ and $e^{i\boldsymbol{k}\cdot\boldsymbol{a}_2/2}$. This defines the Bloch wavevector, $\boldsymbol{k}$, and the associated magnetic Brillouin zone [96]. Now the first Brillouin zone covers $-\pi/a < k_x \leq \pi/a$ and $-2\pi/a < k_y \leq 2\pi/a$, doubling in size. Thanks to this unfolding, the lowest band is nondegenerate at each Bloch wavevector $\boldsymbol{k}$. The resulting bandstructure is shown in Figure 3.8 for $V = 0.0E_R$, $V = 1.0E_R$ and $V = 3.0E_R$.

The Berry curvature is shown over the magnetic Brillouin zone for the lowest band in Figure 3.9, for $V = 1.0E_R$ and $V = 3.0E_R$. For nonzero V, the Chern number of this band is one, so it is analogous to the lowest Landau level. For small V the Berry curvature, Ω, is highly peaked at positions $k = (\pi/a, \pm\pi/a)$; as V increases, Ω spreads out while remaining centered on these two points.

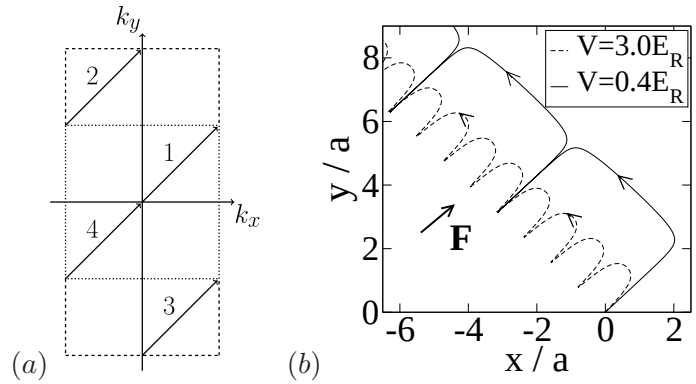

Figure 3.10: (a) The trajectory of a semiclassical wavepacket through the magnetic Brillouin zone, starting from $\boldsymbol{k} = (0,0)$ with $|\boldsymbol{F}| = 1.0F_R$ directed along (1,1). The numbers indicate the order in which the path is travelled. The dotted line indicates the simple Brillouin zone, while the dashed lines shows the extension into the magnetic Brillouin zone. (b) The corresponding real-space trajectory of the wavepacket starting from the origin, for $V = 0.4E_R$ and $V = 3.0E_R$. The motion perpendicular to $\boldsymbol{F}$ is due to the Berry curvature, while that parallel is due to the bandstructure.

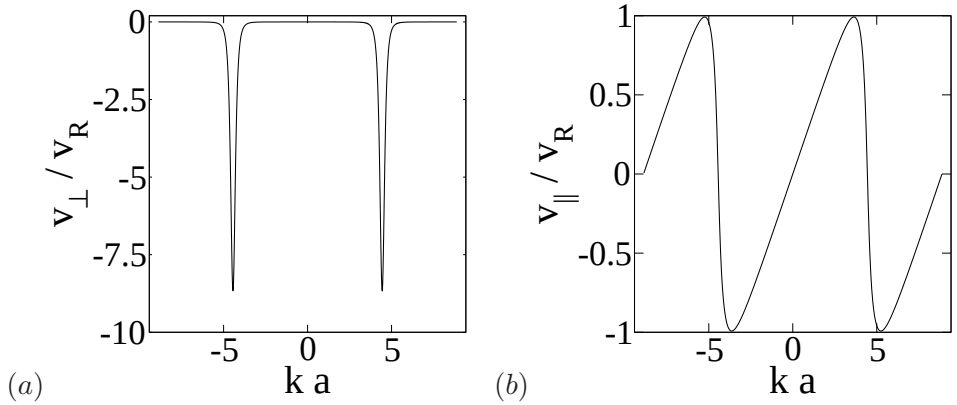

Figure 3.11: The velocity of the wavepacket (a) perpendicular and (b) parallel to the applied force for $|\boldsymbol{F}| = 1.0F_R$ directed along (1,1) and $V = 0.4E_R$. k is measured along the path travelled. For this simple alignment of the force, (a) contains the effects of Berry curvature along the path, while (b) shows the group velocity.

In Figure 3.10(b) we illustrate the real-space trajectory for semiclassical motion of a wavepacket in this optical flux lattice, for $V = 0.4E_R$ and $V = 2.0E_R$. As discussed above, we take $|\boldsymbol{F}| = 1.0F_R$, which is representative of the gravitational force $|\boldsymbol{F}| = m\boldsymbol{g}$ for ^{174}Yb and $\lambda = 578$ nm, parameters which are particularly relevant for this scheme [96, 106]. As shown in Figure 3.10(a), in momentum space the wavepacket starts at $\boldsymbol{k} = (0, 0)$ and moves under a force $\boldsymbol{F}$ parallel to the $(1, 1)$ direction such that it passes through the points $\boldsymbol{k} = (\pi/a, \pm\pi/a)$ at which there is large positive Berry curvature. With $\boldsymbol{F}$ aligned along (1,1), the group velocity is parallel to the force, while the Berry velocity is perpendicular (Figure 3.11).

As the Berry curvature is everywhere positive, there is a net drift as successive regions of high Ω are traversed. For low potentials such as $V = 0.4E_R$ and $V = 2.0E_R$, the bandgap is small and the probability of Landau-Zener transitions on crossing the Brillouin zone boundaries is large. In an experiment where $|\boldsymbol{F}| = m\boldsymbol{g}$, this probability can be reduced below 0.1 by increasing the potential above $V = 3.2E_R$. With higher V, the Berry curvature spreads out and hence the trajectory bends along more of its length. For clarity, we therefore discuss $V = 0.4E_R$ where the effects of Berry curvature and the group velocity are easiest to understand. The

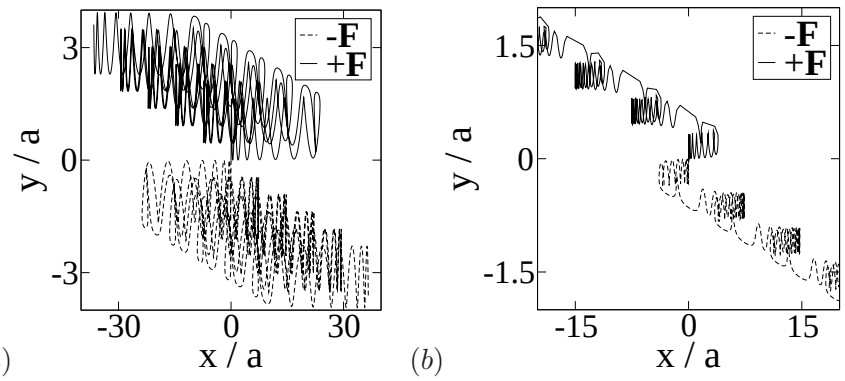

Figure 3.12: Trajectory for a wavepacket travelling with (a) $|\boldsymbol{F}| = 1.0F_R$ and (b) $|\boldsymbol{F}| = 5.0F_R$ where the force is aligned such that $F_x : F_y = 1 : 16$ and $V = 0.4E_R$. The Bloch motion is no longer purely along the direction of the force, and the resultant trajectory is complex. The net drift between Bloch oscillations is a measure of the total Berry curvature along a path, but other information is obscured. The trajectory due to the group velocity increases in size relative to the trajectory due to the Berry curvature with decreasing force (Section 3.4), leading to more complicated motion in (a) than (b).

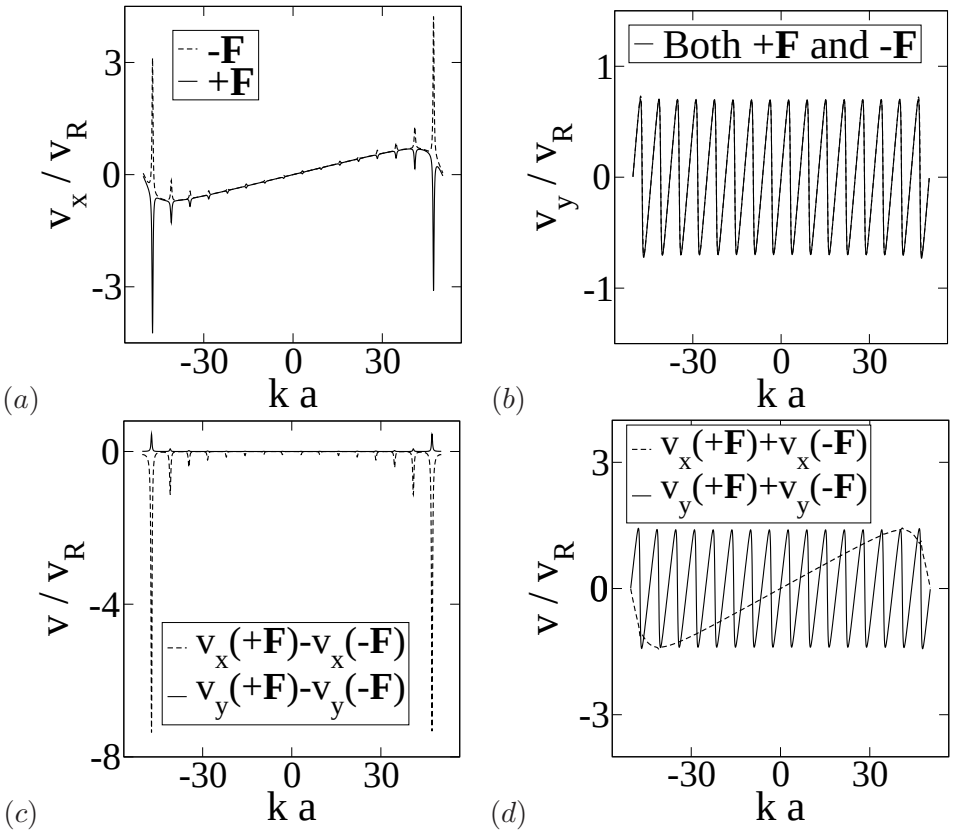

Figure 3.13: (a) Velocity along x of a wavepacket moving under the force $|\boldsymbol{F}| = 1.0F_R$ with $F_x : F_y = 1 : 16$ and $V = 0.4E_R$. k is measured along the path travelled. (b)Velocity along y. (c) Applying the time-reversal protocol to extract the Berry velocity. The Berry velocity calculated from v_x and v_y differ by a factor of 16 from the ratio of the forces, and by a sign, due to the cross product. (d) Applying the time-reversal protocol to extract the group velocity. As expected, there are 16 oscillations from v_y for every one from v_x.

dynamics will be qualitatively the same for higher V, and we discuss the dependence of the motion on both V and $|\boldsymbol{F}|$ in more detail in Section 3.4.

As before, the simplicity of the trajectories and velocities relies on the alignment of $\boldsymbol{F}$ along a special direction. More generally in 2D, the Bloch velocity will not be parallel to the force and complex Lissajous-like figures will be observed; an example of this was previously shown in Figure 3.2 for one oscillation at a low force, $|\boldsymbol{F}| = 0.05F_R$, where the effects of Berry curvature are small.

Here we demonstrate the effect of Lissajous-like figures on the motion for parameter ranges of interest. Figure 3.12 shows the real-space trajectories for (a) $|\boldsymbol{F}| = 1.0F_R$ and (b) $5.0F_R$, when the force is aligned such that $F_x : F_y = 1 : 16$.

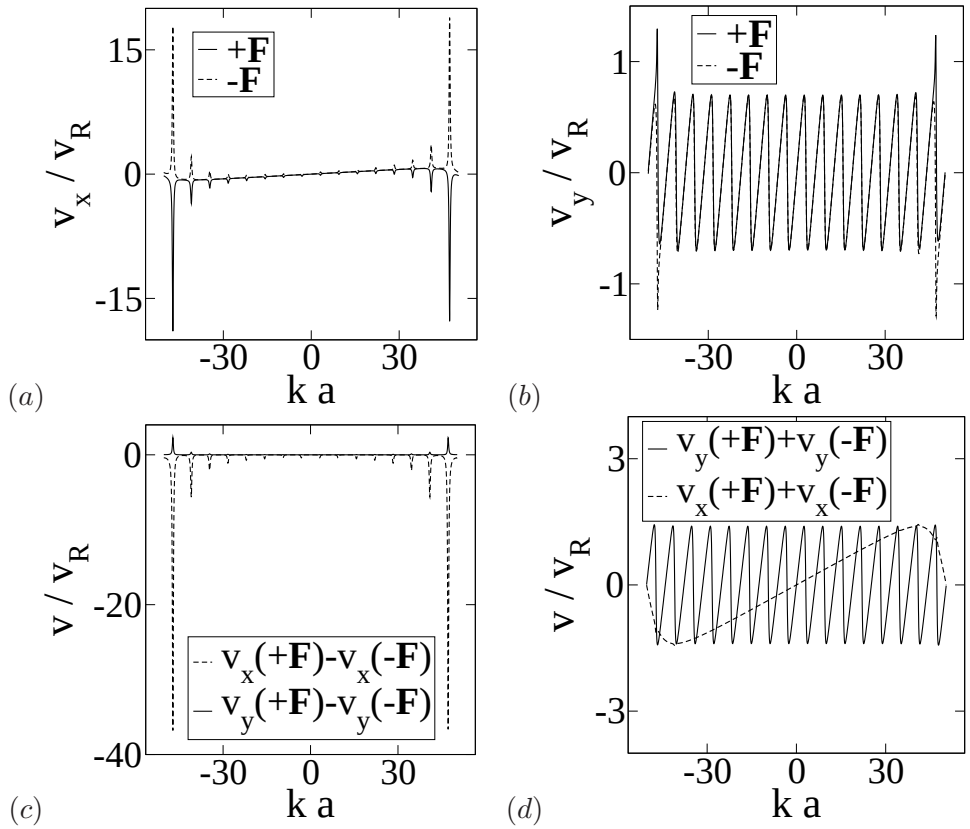

Figure 3.14: As in Figure 3.13 but now for $|\boldsymbol{F}| = 5.0F_R$.

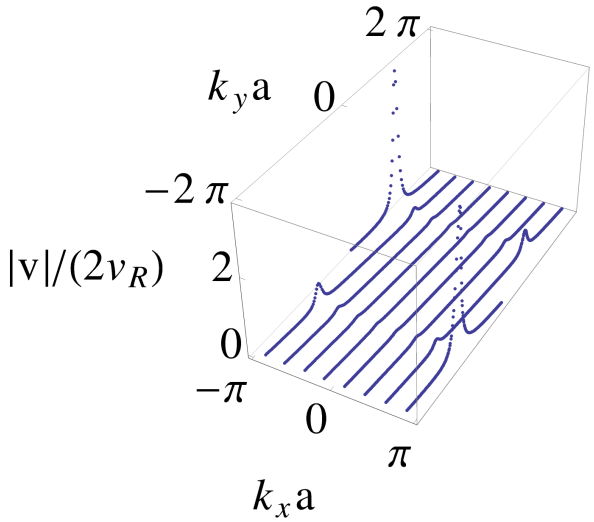

Figure 3.15: $|v_x(+\boldsymbol{F}) - v_x(-\boldsymbol{F})|/2 = 1/\hbar(F_y\Omega)$ plotted along the path taken by the wavepacket in the Brillouin zone for $|\boldsymbol{F}| = 1.0F_R$ with $F_x : F_y = 1 : 16$ and $V = 0.4E_R$. This technique will enable experiments to directly map out the Berry curvature.

The Bloch motion is no longer purely parallel to the force and while an average drift may be measured, the details of the motion due to Berry curvature have been lost.

We illustrate how our time-reversal protocol may be used to extract the local Berry curvature. Figures 3.13 and 3.14 show the velocities along x and y over the path through the Brillouin zone. By comparing the time-reversed velocities, quantities proportional to the Berry velocity and the group velocity are extracted. Figure 3.15 shows the resulting map of Berry curvature over the Brillouin zone for $|\boldsymbol{F}| = 1.0F_R$. The same result is obtained (up to a scale factor) from either of these two cases for different magnitudes of force.

Two-Photon Optical Flux Lattice for $F = 1/2$

To generate optical flux lattices for the more commonly used alkali atoms one must employ dressed states involving a two-photon coupling [107]. We consider the representative case of a lattice with triangular symmetry where the hyperfine states coupled have angular momentum $F = 1/2$, as in species like ^{171}Yb. Qualitatively similar semiclassical dynamics are expected for other values of F, such as the experimentally important case of $F = 1$ for ^{87}Rb [107]. The two-photon optical flux lattice we study leads to an net effective magnetic field in real space in which there is one flux quantum per unit cell. Semiclassical motion within a similar scheme has previously been studied in Ref. [143]. In that scheme, the artificial magnetic field is still locally non zero, but the flux per unit cell vanishes [143, 107] and the Chern number of each band is zero. For the optical flux lattice described here, the energy bands may have non-zero Chern numbers.

For the $F = 1/2$ optical flux lattice, two hyperfine ground states, $g_\pm$, with angular momentum $J_g = 1/2$, are coupled to an excited state, e, also with angular momentum $J_e = 1/2$, via an off-resonance excitation that ensures the population of e remains negligible. The Hamiltonian then acts in the $g_\pm$ manifold, with the form of (3.16). The details of the optical coupling and the resulting Hamiltonian are discussed in Ref. [107] and in Appendix A.

The final Hamiltonian can be written as:

$$\hat{H}' = \hat{U}^\dagger \hat{H} \hat{U} = \frac{(\boldsymbol{p} - \hat{\sigma}_z \hbar \boldsymbol{k}_3/2)^2}{2m} + \hat{V}', \tag{3.20}$$

where $\boldsymbol{k}_3 = k(0, 1, 0)$, and $\hat{U}$ is a unitary transformation that is applied to expose the full symmetry of the system. The transformed optical potential $\hat{V}'$ has the maximal translational symmetry, causing $\hat{\boldsymbol{p}}/\hbar$ to be conserved up to the addition of the reciprocal lattice vectors $\boldsymbol{K}_{1/2} = -k/2(\pm\sqrt{3}, 3, 0)$ (Appendix A). The resulting Brillouin zone, defined by $\boldsymbol{K}_{1/2}$, is equivalent to the asymmetric hexagonal lattice in Section 3.3.1. As can be seen, an important feature of the two-photon optical flux lattice is that, under this unitary transformation, the momenta of $g_\pm$ are offset by $\pm\hbar\boldsymbol{k}_3/2$. This offset does not affect the semiclassical equations of motion, which determine the rate of change of (crystal) momentum under an applied force (3.3), and which still apply for the bands formed from the eigenstates of $\hat{H}'$.

The optical coupling, $\hat{V}'$, is characterised by parameters ϵ and θ as well as the overall strength of the potential V (Appendix A). When $\theta = \epsilon = 0$, the optical potential does not couple the states g_+ and g_-, and acts on each simply as a scalar potential, with the same symmetries as the hexagonal lattice discussed above when inversion symmetry is unbroken. The offsets of the momenta of $g_\pm$ shift the Dirac points of these two states relative to each other. A small non-zero θ breaks inversion symmetry and opens up gaps at the Dirac points in such a way that the pairs of bands are topologically trivial, i.e. have a net Chern number of zero. Non-zero ϵ and θ together break time-reversal symmetry and lead to bands with non-zero Chern number.

We have numerically calculated the bandstructure and Berry curvature of the lowest band for a case of large coupling, when $V = 1.8E_R$, $\theta = 0.3$ and $\epsilon = 0.4$, for which this band has Chern number of one (Figure 3.16). Note that in this case, the energy minimum of the band is not at $\boldsymbol{k} = (0, 0)$. Applying the force along $(0, 1)$, the wavepacket will follow the same path as in the asymmetric hexagonal lattice (Figure 3.6). We choose $|\boldsymbol{F}| = 0.1F_R$ to ensure that the Landau-Zener tunnelling probability is small (below 0.1). The resulting real-space trajectory is shown in Figure 3.17. Due to the simple alignment of the force, we can again associate the

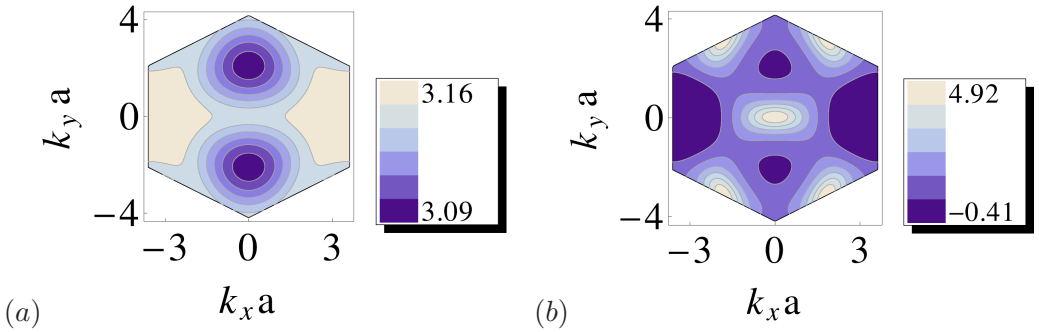

Figure 3.16: (a) The energy (measured in E_R) of the lowest band for $V = 1.8E_R$, $\theta = 0.3$ and $\epsilon = 0.4$. For these parameters, the lowest band has Chern number of one. (b) The corresponding Berry curvature. $\Omega(\boldsymbol{k})$ is in units of 1/[BZ area]. In this case, the Berry curvature is significant over much of the Brillouin zone and has regions of both positive and negative sign.

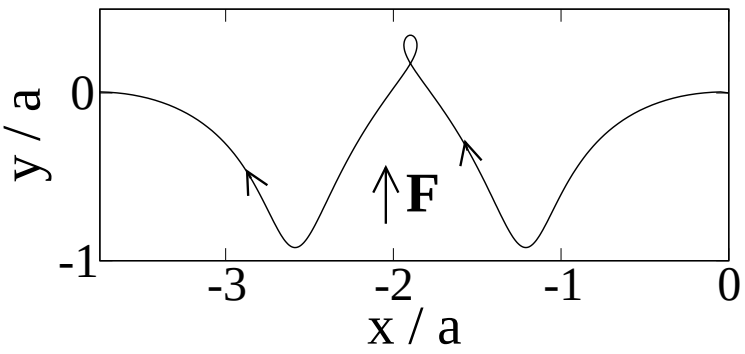

Figure 3.17: The real space trajectory of a wavepacket under a force $\boldsymbol{F} = (0.0, 0.1F_R)$ over one period, for $V = 1.8E_R$, $\theta = 0.3$ and $\epsilon = 0.4$. The wavepacket follows the path described in Figure 3.6. While the group velocity is again purely along y, the motion due to the Berry curvature is more complicated due to the varying sign of Ω.

y motion with the group velocity and the x motion with the effects of the Berry curvature.

As the Berry curvature is substantially spread out through the Brillouin zone (Figure 3.16), there is now a continual drift along x over the trajectory. Since the Chern number is one, the Berry curvature is (largely) of the same sign along the trajectory, leading to a net drift of the wavepacket over one period of the Bloch oscillation. In this lattice, there are also regions of both positive and negative Berry curvature. When the Berry curvature is positive, the wavepacket travels in the negative x direction, while when Ω is negative, the wavepacket moves along the positive x axis. The sign change will therefore not be detected if only the total drift is measured. Instead, the time-reversal procedure described above can again be applied to cleanly map out the local Berry curvature.

3.4 Experimental Considerations

We now consider how the velocity may be measured and how feasible it will be to observe the Berry curvature effects experimentally.

The mean atomic velocity may be extracted from the time-of-flight expansion image. This measures the momentum distribution[40], from which the mean momentum $\langle \boldsymbol{p} \rangle$ may be deduced by the weighted average. The mean atomic velocity of the initial wavepacket then follows from Ehrenfest's theorem as $\langle \boldsymbol{v} \rangle = \langle \boldsymbol{p} \rangle / m$. This approach was successfully experimentally applied by Ben Dahan *et al.*[148] to detect Bloch oscillations in a one-dimensional lattice. The same approach applies for dressed states of internal atomic states, governed by (3.16); in this case the mean velocity can be obtained from the average momentum over all internal states.

Alternatively, it is possible to extract the velocity directly from measurements of the centre of mass motion in real-space. Thanks to recent experimental advances, the position of the wavepacket's centre of mass may be imaged with a high resolution, on the order of a lattice spacing [174]. For bands with nonzero Chern number, the Berry curvature can cause the wavepacket to have a net drift in space over each period of the Bloch oscillation; this leads to large cumulative effects on the position

of the wavepacket over many oscillation periods. As described in Section 3.2.1, measurements of the position of the wavepacket therefore offer a sensitive way to show that the Chern number of the band is nonzero. Indeed measurements of these drifting trajectories in constant applied force are equivalent to measurements of the *edge states* that must arise for a band with non-zero Chern number.

To this end, we consider how to maximise the importance of the effects of the Berry curvature relative to those of the group velocity. In the cases described above where the bands almost touch, we can consider the bandgap, δE, as a small parameter. This applies to the hexagonal lattice when asymmetry is small and to the square one-photon optical flux lattice for small potential, V. (Note that the two-photon optical flux lattice is considered far from the band closing regime.) In the small bandgap limit, the momentum width, δk, over which the band is changed will be $\delta k \simeq \delta E/(\hbar v_R)$, where v_R is the typical group velocity at the zone boundary for vanishing bandgap. The Berry curvature is therefore nonzero over the area, $A \simeq (\delta k)^2$. Assuming the Berry curvature is uniform within this, the invariance of the Chern number means $\Omega \simeq 1/A \simeq 1/(\delta k)^2$. The Berry velocity is $\boldsymbol{v}_\Omega = (\dot{\boldsymbol{k}} \times \hat{\boldsymbol{z}})\Omega$ so, as the wavepacket traverses this region in one Bloch oscillation, the Berry curvature leads to a displacement of size $\int v_\Omega dt \simeq \delta k \Omega \simeq 1/\delta k \simeq \hbar v_R/\delta E$. Conversely, the typical group velocity is $\simeq v_R$ so over the period of one Bloch oscillation, $\tau_B \simeq h/(Fa)$, the typical amplitude of displacement is $v_R \tau_B \simeq h v_R/(Fa)$. Thus, these contributions to the real-space trajectory have different dependences on δE: the Berry curvature contribution scales as $1/\delta E$, while the contribution from the group velocity is independent of δE. This is found in our numerical results, but is shown only qualitatively in the results presented in Figure 3.10, as in this case δE is not that small. The effects of Berry curvature can therefore be maximised with respect to those of the group velocity by choosing a small bandgap. Note also that the two contributions have different dependences on the size of the force: the displacement due to the Berry curvature is independent of force, while that due to the group velocity is inversely proportional to it. Therefore, the Berry effects will be most evident for a high external force. Note, however, that there are some practical limitations on both the choice of force and bandgap. To ensure that the evolution of the wavepacket is adiabatic, the rate of Landau-Zener tunnelling to the next lowest

band should be negligible (3.1). The assumption of adiabatic evolution is therefore violated when the applied force is too high and the bandgap is too small. Also, for small δE, when the bands nearly touch, the Berry curvature becomes concentrated in small regions, of area $(\delta k)^2$. This then requires the momentum of the wavepacket and the alignment of the force to be precisely controlled in order to direct the wavepacket through this region. For intermediate bandgaps, the curvature is spread out. A natural compromise is to choose the bandgap such that δk is as small as the momentum uncertainty $1/w$ with which a wavepacket can be prepared (here w is the spatial width of the wavepacket); one then expects the displacement due to the Berry curvature to be $1/\delta k \simeq w$ on the order of the spatial extent of the wavepacket.

From our numerical calculations, we can quantitatively estimate the length-scales of the dynamics. For example, we consider the dynamics of ^{174}Yb atoms in the one-photon optical flux lattice, with $\boldsymbol{F} = m\boldsymbol{g}$ along (1,1), $\lambda = 578$ nm and $V = 3.2E_R$. For this choice of parameters, the Landau-Zener tunnelling probability given by (3.1) is approximately 0.1. The wavepacket follows the Brillouin zone path in Figure 3.10(a) and has a real-space trajectory similar to that of the dashed line in Figure 3.10(b). As the wavepacket moves along section 1 of its path (from $\boldsymbol{k} = (0, 0)$ to $\boldsymbol{k} = (\pi/a, \pi/a)$), it moves with an average group velocity of 1.0 mm s^{-1}, travelling approximately 0.6 μm in the direction of the force in real-space. For $V = 3.2E_R$, the Berry curvature is substantially spread out over the Brillouin zone, and so the wavepacket's trajectory bends as it travels, moving it 0.3 μm perpendicular to the force. As the wavepacket continues from $\boldsymbol{k} = (-\pi/a, \pi/a)$ to $\boldsymbol{k} = (0, 2\pi/a)$, the group velocity changes sign and the wavepacket travels 0.6 μm in the opposite direction to the force. The Berry velocity does not change sign, and so the wavepacket moves a further 0.3 μm perpendicular to the force. This behaviour repeats for sections 3 and 4 of its path. The average Berry velocity over one complete oscillation is therefore approximately 0.3 mm s^{-1}. If the force is slightly misaligned, the trajectory will instead be a Lissajous-like oscillation, approximately bounded by a box of diagonal length 0.6 μm. For the same Berry velocity, the wavepacket would then take approximately 2.0 ms to drift this distance. These length and time scales are within current experimental capabilities.

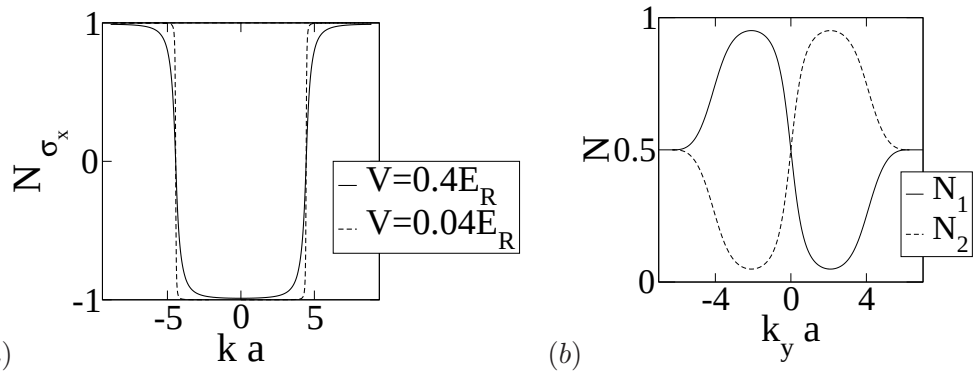

Figure 3.18: (a) Oscillation in expectation value of $\hat{\sigma}_x$ for the one-photon optical flux lattice, as the wavepacket travels along $(1, 1)$. The dashed line is for $V = 0.04E_R$, while the smooth line is $V = 0.4E_R$. The area over which the transfer occurs decreases with potential in a similar way to how the Berry curvature area decreases. k is measured along the path of the wavepacket. (b) Oscillation in population in the two states for the two-photon optical flux lattice as the wavepacket travels along $(0, 1)$ for $V = 1.8E_R$, $\theta = 0.3$ and $\epsilon = 0.4$. The maximum population imbalance appear to be around points K and K'. k_y is measured along the path of the wavepacket.

Two additional practical considerations are the effects of dispersion and interactions. The wavepacket will spread as it travels, and this dispersion could obscure the dynamics described. However, provided the centre of mass of the wavepacket can be measured to an accuracy greater than its width, this should not prevent the observation of Berry curvature effects.

Interactions destroy the coherence of a wavepacket over time and can have a strong dephasing effect on Bloch oscillations [151, 175, 150]. Nonlinearity in BECs can also lead to the collapse of the wavepacket into discrete solitons[3] [175, 176]. We have ignored the effects of interactions in our analysis, an approximation suitable over these time-scales for fermionic atoms [151], for species with low scattering lengths [153] or where the interaction strength can be tuned to zero by means of a Feshbach resonance [177, 152].

One can also look for distinct features in the momentum distributions of atoms undergoing Bloch oscillations in the optical flux lattices discussed above (Figure 3.18). In the two-photon optical flux lattice, the population of atoms oscillates between the two internal states as the wavepacket moves through the Brillouin zone.

[3]This is particularly important when the effective mass, M^*, of the optical lattice is negative[41]

Near the points K and K', the population imbalance is maximum but of opposite sign, reflecting the characteristics of the Berry curvature. In the one-photon optical flux lattice, the unfolding into the full magnetic Brillouin zone means the Bloch states are eigenstates of $\hat{\sigma}_x$. As a result, the oscillation takes place between those superpositions of the internal states that are eigenstates of $\hat{\sigma}_x$ (and not between the internal states themselves). The transfer between eigenstates occurs over an area which decreases with potential, in a similar way to how the Berry curvature area decreases.

3.5 Further Developments in Characterising the Topological Bands of Optical Lattices

In the last two years, there has been much theoretical and experimental interest in characterising the topological and geometrical features of energy bands of optical lattices in ultracold gases. Prior to our work, theoretical papers had shown how to detect the Chern number for certain tight binding models in time-of-flight measurements [178, 179]. Our protocol, published in Ref. [1], shows how the Berry curvature can be mapped over the Brillouin zone for any form of underlying lattice. We shall now briefly discuss some of the recent developments in the field since this published work.

One new method combines Bloch oscillations and Ramsey interferometry for particles with two internal "spin" states (an example protocol is described in Figure 3.19) [146, 180]. This procedure performs the evolution under $\boldsymbol{F}$ and $-\boldsymbol{F}$ simultaneously to separate out the Zak phase. The Zak phase is the total Berry phase along a closed trajectory, where the trajectory lies along some reciprocal lattice vector $\boldsymbol{G}_1$. A version of this method has been used to measure the Zak phase experimentally for a 1D dimerised optical lattice where the Zak phase can be viewed as the topological invariant of the band [146]. In 2D, this method could also be used to extract the Chern number of band [180]. While this protocol has the advantage of experimental simplicity, we note that there are constraints on its applicability. For instance, the dispersion must be symmetric with respect to $\boldsymbol{F}$ and $-\boldsymbol{F}$ in order to eliminate the

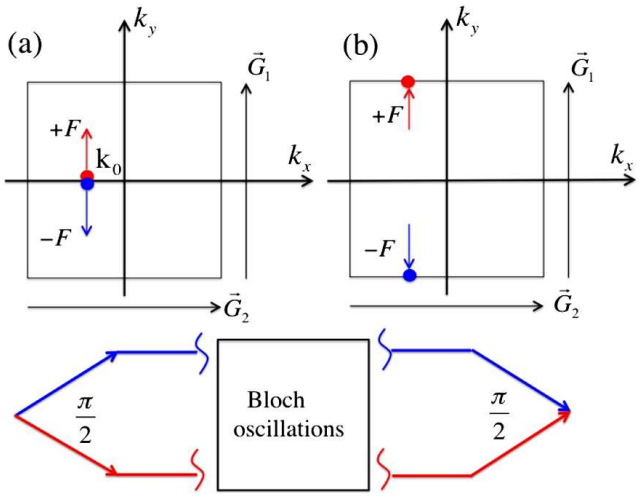

Figure 3.19: Bloch oscillations and Ramsey interferometry: figure taken from Ref. [180]. The wavepacket is initially prepared in a spin-up state at a given quasi-momentum, $\boldsymbol{k}_0$. (a) A $\pi/2$ pulse creates a coherent superposition of spins, $(|\uparrow\rangle + |\downarrow\rangle)/\sqrt{2}$, after which the spin-selective force (e.g. a real magnetic field gradient) is applied. This pushes the spins in opposite directions along the reciprocal lattice vector $\boldsymbol{G}_1$. (b) Following half a Bloch oscillation, the two spins are again at the same point in the BZ, and the $\pi/2$ pulse is repeated. The phase of the Ramsey interference fringes then contains the difference in geometrical phase picked up by the two species. This is the total Berry phase along the closed trajectory $\boldsymbol{G}_1$ (also known as the Zak phase).

effect of the dynamical phase from the Ramsey fringes [180]. Also additional steps may need to be introduced to remove the magnetic Zeeman phase, for example by combining the above with a spin-echo procedure [180, 146].

Another way to characterise the topology of a band is to directly detect its topological edge states. The bulk-boundary correspondence relates the Chern number, $\mathcal{C}$, of a bulk energy band to the number and chirality of robust gapless edge states on the boundary[4]. These edge states could be directly detected, for example, through light scattering [181, 182, 183]. By generalising Bragg spectroscopy to probe angular momentum, the topological edge states would be distinguished by their chirality [183]. Another recent theoretical proposal shows how to image the dynamics of the edge states through in-situ density measurements (Figure 3.20) [184].

Finally, there have been efforts to observe the quantum Hall effect directly in

[4]As mentioned above the measurements of drifting trajectories in our method are equivalent to measuring these edge states.

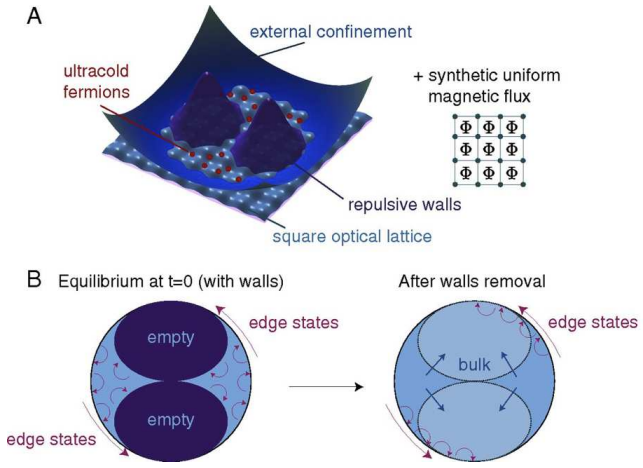

Figure 3.20: Measuring edge states: figure taken from Ref. [184]. (A) Cold trapped gas of fermions on an optical lattice with a synthetic uniform magnetic flux. The gas is confined by a circular potential and two additional repulsive regions. (B) The edge states travel around the inner walls and outer boundary. When the walls are removed suddenly at $t = 0$, the chiral edge states propagate around the new boundary, encircling the initially empty regions. For a dispersion-less band, the bulk is motionless and the states would be visible through in-situ imaging of the density. For dispersive bands, the bulk will also flow into the empty regions, and additional steps can be used to extract the contribution of the edge states.

ultracold gases. The current-carrying topological edges states lead to a quantised Hall conductance, σ_{xy}, which is proportional to the Chern number of a filled band. In the solid-state, σ_{xy} is measured through transport experiments as $j_x = \sigma_{xy} E_y$, where j_x is the current along $\hat{\boldsymbol{x}}$, and E_y is the electric field along $\hat{\boldsymbol{y}}$. In an ultracold gas, the analogous experiment is technically demanding, as it is difficult to couple an ultracold cloud to reservoirs and measure atomic currents. However, the first steps in this direction have been made with measurements of the conduction of fermions through a mesoscopic channel [185]. Alternatively, the Chern number might be measured from the drift of a cloud of fermions initially prepared as the filled band of a Chern insulator and confined in a sub-region of a larger trap [186]. Upon release into the larger trap, the velocity of the centre-of-mass is then proportional to the force applied and an approximate Chern number[5]. (This is Eq. 3.11 above.)

Another experiment has measured a superfluid Hall effect in a weak artificial magnetic field using collective modes[187]. They excite a mode along $\hat{\boldsymbol{x}}$ and, after

[5]The Chern number measured is approximate due to the effects of the finite-size of the initial region, non-linearity, band-mixing and variations in atomic filling fraction [186].

driving for a varying length of time, measure the atomic density either by time-of-flight or in-situ absorption imaging. It is then possible to reconstruct the motion of the cloud and observe correlated transport along $\hat{\boldsymbol{y}}$ when the magnetic field is present: the signature of the Hall behaviour. While the synthetic field is very weak (the system is still vortex-free), such a technique could be extended to explore quantum Hall physics. We shall show in Section 4 how in the general case of an atomic gas in a bandstructure with topological features there are important modifications of the collective modes. Our analysis will include systems threaded with many flux quanta, as well as optical lattices with uniform [100] or nonuniform flux [101].

3.6 Conclusions

In summary, we have proposed a general method for mapping the local Berry curvature over the Brillouin zone in ultracold gas experiments. The Berry curvature crucially modifies the semiclassical dynamics and so affects the Bloch oscillations of a wavepacket under a constant external force. In particular, the Berry curvature may lead to a net drift of the wavepacket with time. However, two-dimensional Bloch oscillations are interesting in their own right, and we may lose information about the Berry curvature due to the complicated Lissajous-like figures that may arise.

We have shown that this information can be recovered via a "time-reversal" protocol. The group velocity at a point in the Brillouin zone is invariant under a reversal of force, while the Berry velocity changes sign. As a result, the velocities under positive and negative force can be compared to extract either one or the other. This protocol will allow the local Berry curvature to be cleanly mapped out over the path of the wavepacket through the Brillouin zone.

We have demonstrated this protocol using the semiclassical dynamics of three model systems which are currently of experimental interest: the asymmetric honeycomb lattice and two optical flux lattices. We have also discussed various experimental considerations, including how the velocity may be measured and how to maximise the magnitude of the Berry curvature effects on the dynamics. Finally we

have reviewed recent efforts in the field to characterise the topological properties of energy bands. There are many promising avenues of research, including the successful experimental use of Bloch oscillations and Ramsey interferometry to measure geometrical phases.

Chapter 4

The Effects of Berry Curvature on the Collective Modes of Ultracold Gases

Collective modes are powerful tools for exploring the properties of ultracold gases[8]. The high precision with which oscillation frequencies can be measured [188] affords high sensitivity to the underlying physical properties, such as the equation of state over the BEC-BCS crossover[188, 189, 190, 36]. Recently, collective modes have been used to measure the superfluid Hall effect in a weak artificial magnetic field[187]. In this chapter, we show that, in the general case of an atomic gas in a bandstructure with topological features, there are important modifications of the collective modes which are entirely controlled by the Berry curvature. This work has been submitted for publication as Ref. [2].

In Section 4.2, we show how the Berry curvature shifts oscillation frequencies for a Bose-Einstein condensate and splits otherwise degenerate modes. We extend our analysis to other systems with a polytropic equation of state. The effects of Berry curvature are illustrated with the model of 2D Rashba spin-orbit coupling in Section 4.3. We also analyse this using sum rules (Section 4.4) and a dipole operator approach (Section 4.5). Furthermore, we demonstrate using the operator approach how the effects of Berry curvature arise naturally for a general multi-band Hamiltonian. Our results show that Berry curvature can have sizeable effects on experimental mode frequencies (Section 4.6). Hence measurements of the collective

modes of a trapped BEC can be used to determine the geometrical properties of the condensate wave function.

4.1 Introduction to Collective Modes

4.1.1 The Basic Properties of Collective Modes

Collective modes are emergent many-body oscillations of an ultracold cloud of atoms. The motion of a BEC is collective if the wavelength of the excitation is longer than the coherence length, $\xi = (\hbar^2/2M\rho g)^{1/2}$. At distances shorter than ξ, the kinetic energy is larger than the mean-field interaction energy, and the atoms behave like free particles[8]. Collective modes are therefore the low energy, long wavelength excitations of the BEC, dominated by interactions rather than the kinetic energy.

In a uniform untrapped gas, the collective modes are phonon-like at low frequency. The presence of a trap breaks translational invariance, so momentum is no longer a good quantum number. Instead, modes in a spherically symmetric 3D trap are characterised by l, the total angular momentum; m, the projection of angular momentum on the polar axis and n_r, the number of radial nodes. To neglect the kinetic energy in a trap, the BEC must contain a sufficiently large number of particles[8]. Then we can make the Thomas-Fermi approximation[1] and neglect the kinetic energy in the Gross-Pitaevskii equation:

$$[V(\boldsymbol{r}) + g|\psi(\boldsymbol{r})|^2]\psi(\boldsymbol{r}) = \mu\psi(\boldsymbol{r}). \tag{4.1}$$

Re-arranging this, we find the local density: $\rho(\boldsymbol{r}) = |\psi(\boldsymbol{r})|^2 = [\mu - V(\boldsymbol{r})]/g$, where $V(\boldsymbol{r})$ is the (harmonic) trapping potential and ρg is the interaction energy. This is valid provided that the wave function varies on length scales much longer than the local coherence length. This approximation also breaks down within a distance δ_c of the edge of the cloud, where the kinetic energy term is again important[8]. Therefore to describe collective behaviour in a trap, we use the Thomas-Fermi approximation and require that modes have wavelengths longer than the local ξ and

[1] This is valid when $Na_s/a_{\text{osc}} \gg 1$, for repulsive interactions in a harmonic trap (with $a_{\text{osc}} = \sqrt{\hbar/M\omega_0}$)[8].

are not concentrated in the boundary region, δ_c.

4.1.2 Collective Modes in Experiments

Collective modes can be excited in experiments by adding a small time-dependent perturbation to the trapping potential[191, 192, 193] or by modulating the interaction strength[194]. Different modes are induced by applying a driving force with the appropriate frequency and symmetry. The frequencies of the modes can then be extracted using, for example, in-situ phase-contrast imaging[193] or absorption imaging after expansion of the cloud[191, 188]. Thanks to the high precision possible in such measurements[188], collective modes serve as excellent experimental probes of the many-body physics of ultracold gases. As previously mentioned, collective modes have been used to measure the equation of state across the BEC-BCS crossover[189, 190, 36] and the effects of a weak magnetic field[187]. Other applications include the study of rotating gases[195, 196, 197], superfluidity[198, 199], lower dimensions[200] and random potentials[201].

Collective modes have a finite life-time due to interactions with thermal excitations or nonlinear interactions with other modes[8]. Damping rates $\simeq 2\text{s}^{-1}$ have been observed for low frequency modes of low temperature condensates[193, 188]. While we do not include thermal and nonlinear effects in our theoretical work, we do show that the effects of Berry curvature can be large and may be observed within these experimental constraints (Section 4.6).

4.1.3 Theoretical Approaches to Collective Modes

The dynamics of a weakly interacting dilute Bose-Einstein condensate are described at the mean-field level by the time-dependent Gross-Pitaevskii equation. This can be solved directly with numerical techniques[202] or a variational trial wave-function[8, 203, 204]. However, for small amplitude oscillations, the calculation is simplified by linearising the GP equation. This leads to the Bogoliubov equations for the quasiparticle amplitudes (see Refs. [37, 8]), or equivalently, the hydrodynamic equations

of motion for ρ, the local density and $\boldsymbol{v}$, the local velocity[2](Section 4.2).

Other complementary approaches do not require us to solve the full equations of motion. In Section 4.4, we discuss a sum rule approach, based on linear response theory, while in Section 4.5, we employ an operator method using the Heisenberg equations of motion. These methods also have the advantage of not relying intrinsically on the Thomas-Fermi approximation[3].

There can also be beyond-mean-field corrections, although we do not include these effects in our theoretical work. To lowest order, strong interactions lead to quantum depletion of the ground state, and introduce a correction to the equation of state[205, 206]. This shifts the frequencies of some collective modes by a few percent for relevant system parameters[207, 208]. Such beyond mean-field effects have been observed in precision measurements of the collective modes of a Fermi gas in Ref. [188].

4.2 The Hydrodynamic Equations of Motion

The Hydrodynamic Equations Without Berry Curvature

The standard hydrodynamic equations of motion for a weakly interacting dilute Bose-Einstein condensate at zero temperature are[8]:

$$\begin{aligned} &\dot{\rho} + \boldsymbol{\nabla} \cdot (\rho \boldsymbol{v}) = 0 \\ &M\dot{\boldsymbol{v}} = \boldsymbol{F} = -\boldsymbol{\nabla}\left(V + \rho g - \frac{\hbar^2}{2M\sqrt{\rho}}\boldsymbol{\nabla}^2\sqrt{\rho} + \frac{1}{2}Mv^2\right) \end{aligned} \tag{4.2}$$

where $\boldsymbol{F}$ is now the local force per particle. These resemble the classical equations of fluid dynamics. The first equation is the familiar continuity equation, expressing the conservation of mass. The second equation is analogous to the Euler equation, applied to potential flow of an ideal fluid with pressure: $P = \rho^2 g/2$ [37, 8]. This is a statement of the conservation of momentum.

[2]For vanishing Berry curvature, the hydrodynamic variables are introduced via the substitution $\psi(\boldsymbol{r}) = \sqrt{\rho}e^{i\phi}$ in the GP equation, where $\boldsymbol{v} = \frac{\hbar}{M}\boldsymbol{\nabla}\phi$. Then we obtain Eq. 4.2.

[3]This is particularly useful for attractive interactions, as the condensate collapses before the Thomas-Fermi limit, $Na_s/a_{\mathrm{osc}} \gg 1$, is reached[38].

However, unlike classical hydrodynamics, the second equation contains a quantum pressure term: $\frac{\hbar^2}{2M\sqrt{\rho}}\boldsymbol{\nabla}^2\sqrt{\rho}$. Whereas the other kinetic term, $\frac{1}{2}Mv^2$, describes particle currents, the quantum pressure captures 'zero point motion' and is a consequence of the Heisenberg uncertainty principle[8, 37]. This term can be neglected when the wave function varies on lengths much longer than the coherence length: $\xi = (\hbar^2/2M\rho g)^{1/2}$. This is the Thomas-Fermi approximation for large N introduced above. If we assume that the quantum pressure is negligible, the analogy to the Euler equation is complete[4]. For the standard treatment of the hydrodynamic equations without Berry curvature see Ref. [209, 37, 8].

The Hydrodynamics Equations with Berry Curvature

We now consider a BEC formed in a minimum of some single-particle energy dispersion, $E(\boldsymbol{p})$. This dispersion could be the lowest band of an optical lattice, where $\boldsymbol{p}$ is the crystal momentum, or of a spin-orbit coupling Hamiltonian (like Eq. 4.10). We assume that the radius of the cloud is much larger than any other length scale and that the band-gap is much larger than any other energy scale, such that all properties of the BEC are well-described by those at the minimum. The energy dispersion is characterised by the effective mass, $M^*_{\alpha\beta} = \hbar^2/\left(\partial^2 E/\partial p_\alpha \partial p_\beta\right)$, where α, β run over the spatial coordinates. This will renormalize the collective mode frequencies[210]. Furthermore, the eigenstates are characterised by the Berry curvature (Section 1.1.1):

$$\boldsymbol{\Omega}_n(\boldsymbol{p}) \equiv i\frac{\partial}{\partial \boldsymbol{p}} \times \langle n\boldsymbol{p}|\frac{\partial}{\partial \boldsymbol{p}}|n\boldsymbol{p}\rangle, \tag{4.3}$$

where $|n\boldsymbol{p}\rangle$ is the energy eigenstate in band n at $\boldsymbol{p}$ (i.e. the periodic Bloch function for an optical lattice)[12]. Thus, the energy minimum must also be characterized by the value of the Berry curvature at that point. To simplify presentation, we assume that the effective mass is isotropic, $M^*_{\alpha\beta} \equiv M^*\delta_{\alpha\beta}$, and choose axes such that the local Berry curvature is $\Omega\hat{\boldsymbol{z}}$, but all results can be readily extended to the anisotropic case.

[4]This analogy is very useful as it will allow us to analyse both condensates and normal gases within the same basic hydrodynamic framework in Section 4.2.1.

To determine the effects of Berry curvature on the collective modes, we derive the new hydrodynamic equations at zero temperature for a weakly interacting Bose condensate. By including the so-called "anomalous contribution" to the velocity [12] we find:

$$\begin{aligned} \dot{\rho} + \boldsymbol{\nabla} \cdot (\rho \boldsymbol{v}) &= 0 \\ \dot{\boldsymbol{v}} &= \frac{\boldsymbol{F}}{M^*} - \left(\frac{\dot{\boldsymbol{F}}}{\hbar} \times \hat{\boldsymbol{z}} \right) \Omega, \end{aligned} \tag{4.4}$$

where $\boldsymbol{F}$ is given in Eq. 4.2, and where we have included the modification by the effective mass[210]. We are interested in small deviations from equilibrium, $\rho = \rho_0 + \delta\rho$. We assume that the particle number, N, is large so that quantum pressure is negligible and the Thomas-Fermi approximation is valid. Then $\rho_0(\boldsymbol{r}) = |\psi(\boldsymbol{r})|^2 = [\mu - V(\boldsymbol{r})]/g$ and $\delta\boldsymbol{F} = -g\boldsymbol{\nabla}\delta\rho$. Linearizing Eq. 4.4 with respect to $\delta\rho$, we find:

$$\delta\ddot{\rho} = -\frac{\boldsymbol{\nabla}V \cdot \boldsymbol{\nabla}\delta\rho}{M^*} + \frac{\rho_0 g \boldsymbol{\nabla}^2 \delta\rho}{M^*} + \frac{\boldsymbol{\nabla}V \cdot (\boldsymbol{\nabla}\delta\dot{\rho} \times \hat{\boldsymbol{z}})\Omega}{\hbar}. \tag{4.5}$$

For a uniform gas, with no trap potential $V(\boldsymbol{r}) = 0$, the collective oscillations are sound modes, with frequencies $\omega = \sqrt{\rho_0 g/M^*}|\boldsymbol{k}|$ that are unaffected by Berry curvature.

For a harmonic trap, $V(\boldsymbol{r}) = \frac{1}{2}\kappa|\boldsymbol{r}|^2$, the modes have the form $\delta\rho = D(r)Y_{lm}(\theta,\varphi)e^{-i\omega t}$ where $Y_{lm}(\theta,\varphi)$ is a spherical harmonic[209, 38]. (As mentioned above, the three quantum numbers are: l, the total angular momentum, m, the projection of angular momentum on the polar axis and n_r, the number of radial nodes.) In Appendix B, we solve Eq. 4.5 to find:

$$\omega = -\frac{m\kappa\Omega}{2\hbar} + \frac{1}{2}\sqrt{\left(\frac{m\kappa\Omega}{\hbar}\right)^2 + \frac{4\kappa}{M^*}(l + 3n_r + 2n_r l + 2n_r^2)}. \tag{4.6}$$

The corresponding eigenstates have $D(r) \propto r^l F(-n_r, l + n_r + 3/2; l + 3/2, r^2/R^2)$, where F is the hypergeometric function and $R = \sqrt{2\mu/\kappa}$ the radius of the cloud. When $\Omega = 0$, we recover the expected mode energies [209, 38]. Non-zero Berry curvature affects the frequencies of only those modes with $m \neq 0$, breaking the

$(2m+1)$ degeneracy.

4.2.1 Polytropic Equation of State

We extend the hydrodynamic approach to a general polytropic equation of state: $P \propto \rho^{\gamma+1}$, where P is the pressure and $\boldsymbol{F} = -\frac{1}{\rho}\boldsymbol{\nabla}P - \boldsymbol{\nabla}V$. For the weakly interacting Bose condensate, $P = \frac{1}{2}g\rho^2$ and $\gamma = 1$. The exponent $\gamma = 2/3$ describes a dilute Fermi gas, an ideal normal Bose gas under adiabatic conditions and Bose and Fermi gases[5] in the strongly interacting (unitarity) limit [211, 212, 190]. In Appendix C, we derive the following equation for the velocity from the hydrodynamic equations with the polytropic equation of state:

$$\begin{aligned}\frac{\partial^2 \boldsymbol{v}}{\partial t^2} &= \frac{(\gamma+1)}{M^*}\frac{P_0}{\rho_0}\boldsymbol{\nabla}(\boldsymbol{\nabla}\cdot\boldsymbol{v}) - \frac{1}{M^*}\boldsymbol{\nabla}(\boldsymbol{\nabla}V\cdot\boldsymbol{v}) - \frac{\gamma}{M^*}\boldsymbol{\nabla}V(\boldsymbol{\nabla}\cdot\boldsymbol{v}) \\ &\quad -\frac{\Omega}{\hbar}\left[(\gamma+1)\frac{P_0}{\rho_0}\boldsymbol{\nabla}\left(\boldsymbol{\nabla}\cdot\frac{\partial\boldsymbol{v}}{\partial t}\right) - \boldsymbol{\nabla}\left(\boldsymbol{\nabla}V\cdot\frac{\partial\boldsymbol{v}}{\partial t}\right) - \gamma\boldsymbol{\nabla}V\left(\boldsymbol{\nabla}\cdot\frac{\partial\boldsymbol{v}}{\partial t}\right)\right]\times\hat{\boldsymbol{z}} \qquad (4.7)\end{aligned}$$

As is known without Berry curvature[211, 8], this equation differentiates between three classes of modes: incompressible modes ($\boldsymbol{\nabla}\cdot\boldsymbol{v} = 0$), which are system-independent; compressible modes with $\boldsymbol{\nabla}(\boldsymbol{\nabla}\cdot\boldsymbol{v}) = 0$, which depend only on γ, and all other modes which depend on both γ and the equilibrium properties of the gas through P_0/ρ_0. The Berry curvature contributes a divergence-free (and rotational) component to the velocity (Eq. 4.4) and so preserves these three classes. Below, we use this equation to derive the frequencies for important specific modes in a general system.

If the polytropic equation of state governs both variations in the density, $\delta\rho$, and the equilibrium density, ρ_0, we also find (Appendix C):

$$\frac{\partial^2\delta\rho}{\partial t^2} + \boldsymbol{\nabla}\cdot\left(\rho_0\left(-\frac{a_p(\gamma+1)}{M^*}\boldsymbol{\nabla}(\rho_0^{\gamma-1}\delta\rho) + \frac{a_p(\gamma+1)}{\hbar}\left(\boldsymbol{\nabla}\frac{\partial}{\partial t}(\rho_0^{\gamma-1}\delta\rho)\times\hat{\boldsymbol{z}}\right)\Omega\right)\right) = 0 \qquad (4.8)$$

where a_p is a dimensionful constant. This condition is fulfilled by a non interacting, low temperature Fermi gas (Appendix C) and a weakly interacting dilute Bose

[5] Our results can be extended to Fermi systems, provided the atoms only occupy states near the minimum of the energy dispersion, and so are described by the same effective mass and Berry curvature.

gas[6]. However, it is not valid for other systems, such as an ideal normal gas. The equilibrium properties of the gas are then isothermal, and P_0 and ρ_0 are set by the ideal gas law. The polytropic equation of state describes only adiabatic deviations of an ideal gas from equilibrium. With this restriction in mind, we solve Eq. 4.8 for the mode frequencies[7] of weakly interacting Bose and Fermi gases:

$$\omega = -\frac{m\kappa\Omega}{2\hbar} + \frac{1}{2}\sqrt{\left(\frac{m\kappa\Omega}{\hbar}\right)^2 + \frac{4\kappa}{M^*}(l + \gamma n_r(2l + 2n_r + 1) + 2n_r)}. \quad (4.9)$$

(Again, this is a more general form of Eq. 4.6.) Therefore, under these conditions, we see that the effects of Berry curvature on the collective mode frequencies do not depend on particle statistics.

4.2.2 Important Classes of Modes

The most important collective modes in experiments are those at low frequency which are easiest to excite and observe[8, 191]. One significant class of modes are the surface waves which have $n_r = 0$ and $\delta\rho \propto r^{l-1}Y_{lm}(\theta,\varphi)e^{-i\omega t}\frac{\partial\rho_0}{\partial r}$. These include the low frequency dipole ($l = 1$) and quadrupole modes ($l = 2$). We find that, as in the case without Berry curvature [211, 212], the mode frequencies are independent of the equation of state. This can be seen from Eq. 4.7, when we note that surface modes are incompressible, $\boldsymbol{\nabla}\cdot\boldsymbol{v} = 0$, and that all system-dependence drops out.

Surface modes are also valid solutions for an anisotropic trap: $V(x,y,z) = \frac{1}{2}\kappa^2(x^2+y^2) + \frac{1}{2}\kappa_z^2 z^2$. The anisotropy lifts the degeneracy between modes with different values of $|m|$. For example, without Berry curvature, the dipole modes for the weakly interacting Bose condensate are $\delta\rho \propto (x \pm iy) \propto rY_{1\pm1}(\theta,\varphi)$ at frequency $\omega = \sqrt{\kappa/M^*}$, and $\delta\rho \propto z \propto rY_{10}(\theta,\varphi)$ at frequency $\omega = \sqrt{\kappa_z/M^*}$ [38]. In what follows, we shall refer to $\delta\rho \propto (x \pm iy)$ as the (quasi)-2D dipole modes. Figure 4.1 shows schematically how the Berry curvature splits these modes. In the absence of Berry curvature, the quadrupole modes with $m = \pm2$ or $m = \pm1$ can also be linearly

[6] Eq. 4.8 becomes Eq. 4.5 when $\gamma = 1$ and $a_p = g/2$.

[7] The general density variation is: $\delta\rho \propto D(r)Y_{l,j}(\theta,\varphi)(R^2-r^2)^{(\gamma-1)/\gamma}e^{-i\omega t}$. The extra factor of $(R^2-r^2)^{(\gamma-1)/\gamma}$ is nonzero for Fermi gases but vanishes for weakly interacting Bose condensates as expected. This ensures that the density variation vanishes continuously at the edge of the cloud for a degenerate Fermi gas. This is important as, for this system, the kinetic energy of the wave function cannot be neglected. For a full discussion of this issue, see for example Ref. [213].

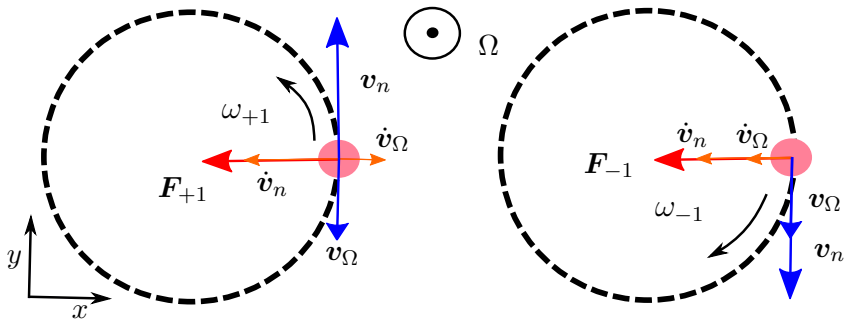

Figure 4.1: The Berry curvature splits degenerate modes, as shown here for the 2D dipole oscillations in a weakly interacting Bose gas: $\delta\rho_{\pm1} = (x \pm iy)e^{-i\omega t}$ (i.e. $n_r = 0$, $l = 1$, $m = \pm1$). An element of fluid (pink circle) feels a restoring force, $\boldsymbol{F}_{\pm1} = -g\boldsymbol{\nabla}\delta\rho_{\pm1} = -g\,(1, \pm i)\,e^{-i\omega t}$, around the dashed curve. Without Berry curvature, the acceleration, $\dot{\boldsymbol{v}}_n$, and velocity, $\boldsymbol{v}_n$, have the same magnitude for both modes and $\omega_{+1} = \omega_{-1}$. The Berry curvature couples to the time-dependent force, giving an additional acceleration, $\dot{\boldsymbol{v}}_\Omega$, and velocity, $\boldsymbol{v}_\Omega \propto (\boldsymbol{F} \times \hat{\boldsymbol{z}})\Omega$. This is analogous to the "guiding centre" velocity of a particle in electromagnetic fields (c.f. $\boldsymbol{v} \propto (\boldsymbol{E} \times \boldsymbol{B})$). The resultant frequencies are split; ω_{+1} is lowered and ω_{-1} is raised.

combined to give the scissors modes [198](with $\delta\rho \propto xy, yz, xz$). The existence of the scissors modes relies on the degeneracy between $\pm|m|$. Here these mode frequencies are split, and so the modes must retain their angular symmetry.

Another important low-lying mode is the breathing mode ($n_r = 1$ and $l = m = 0$). Without Berry curvature, the velocity field is purely radial ($\boldsymbol{v} \propto \boldsymbol{r}$), and the density oscillation resembles a "breathing" of the cloud [38]. The mode frequency now depends on the equation of state[8]: $\omega = \sqrt{(3\gamma + 2)\kappa/M^*}$[211, 212]. Solving Eq. 4.7, we find that this mode frequency is unchanged for $\Omega \neq 0$, since it has no angular momentum along $\hat{z}$. However, it is interesting to note that the mode velocity field is changed, gaining an extra rotational (divergence-free) component $\propto \boldsymbol{r} \times \hat{\boldsymbol{z}}$.

4.3 2D Rashba Spin-Orbit Coupling

We illustrate the effects of the Berry curvature on collective modes for a simple model of Rashba spin-orbit coupling. We have discussed the achievability of this coupling

[8]We note that the breathing mode falls into the second class of modes: it is compressible with $\boldsymbol{\nabla}(\boldsymbol{\nabla}\cdot\boldsymbol{v}) = 0$. Therefore its frequency depends on γ but is independent of the equilibrium properties of the gas.

in current and future ultracold gas experiments in Section 2.2. We consider a 2D interacting spin-1/2 gas described by the Hamiltonian

$$\hat{H} = \sum_i \hat{h}_0(i) + \frac{1}{2} g_{2\mathrm{D}} \sum_{i \neq j} \delta(x_i - x_j)\delta(y_i - y_j)$$
$$\hat{h}_0 = \frac{\boldsymbol{p}^2}{2M} + \lambda_R(p_x\hat{\sigma}_y - p_y\hat{\sigma}_x) - \Delta\hat{\sigma}_z + V(x,y). \tag{4.10}$$

where $g_{2\mathrm{D}}$ is the effective contact interaction in 2D, $i = 1, ..., N$ is the particle index, and $\hat{\sigma}_{x,y,z}$ are the Pauli spin matrices. We assume that the interaction strength is independent of spin, which is a good approximation for ^{87}Rb. The single-particle Hamiltonian, $\hat{h}_0$, is characterised by a Rashba spin-orbit coupling, λ_R, and a Zeeman field, Δ. The effects of spin-orbit coupling on the collective modes have previously been studied for 1D [130, 214, 215] (where there can be no Berry curvature) and for the 2D dipole mode in a thermal gas using a Boltzmann approach [216].

Without a trap, the single-particle energy spectrum is $\varepsilon_\pm = \frac{p^2}{2M} \pm \sqrt{\lambda_R^2 p^2 + \Delta^2}$. The corresponding Berry curvature is [12]:

$$\Omega_\pm = \mp \frac{\lambda_R^2 \Delta \hbar^2}{2(\lambda_R^2 p^2 + \Delta^2)^{3/2}}. \tag{4.11}$$

When $\zeta \equiv \frac{\lambda_R^2 M}{\Delta} < 1$, there is a single minimum in the lower band at $p = 0$. This minimum has effective mass $M^* = \frac{M}{1-\zeta}$, and Berry curvature $\Omega = \frac{\lambda_R^2 \hbar^2}{2\Delta^2}$ [12]. We consider the collective oscillations of a BEC formed in this single minimum. In addition to ζ, the mean-field theory for the Hamiltonian (Eq. 4.10) is characterised by two other dimensionless parameters: $\chi \equiv \frac{\hbar\omega_0}{\Delta}$ (where $\omega_0 = \sqrt{\kappa/M}$), which compares the trap and the band-gap, and $G \equiv \frac{N g_{2\mathrm{D}} M}{\hbar^2}$, which compares the interactions to the trap. We assume that $G \gg 1$ to justify the Thomas-Fermi approximation which improves with increasing particle number, N. We also take $\chi \lesssim 1$, to avoid mixing with higher bands.

4.3.1 Collective Modes from Hydrodynamics

The three lowest sets of 2D surface mode frequencies ($n_r = 0$, $l = |m| = 1, 2, 3$ in Eq. 4.6) are shown in Figure 4.2 for intermediate trapping, $\chi = 0.2$, where the splitting

due to Berry curvature is significant. Without Berry curvature (in the limit $\chi \ll 1$), the mode frequencies are $\omega/\omega_0 = \sqrt{(M/M^*)l}$ for both $m = \pm l$). As $\zeta \to 1$, the effective mass, $M^* = \frac{M}{1-\zeta}$, diverges and $\omega/\omega_0 \to 0$. This is the transition from the single minimum to the ring of degenerate minima at nonzero momenta in the energy spectrum. When Berry curvature is present, the modes split. The energy splitting between surface modes with $m = \pm l$ is $\frac{\delta\omega}{\omega_0} = \frac{1}{2}\zeta\chi l$ (Eq. 4.6). As discussed above, it is necessary that $\chi \lesssim 1$ and $0 < \zeta < 1$; this sets an upper limit of $\frac{\delta\omega}{\omega_0} \lesssim 50\% \times l$. Note that this splitting can be large (especially for large l). It is also interesting to note that, while the mode frequencies without Berry curvature all go to zero at $\zeta = 1$ (where $M^* \to \infty$), for non-zero Berry curvature there remain modes at nonzero frequency[9].

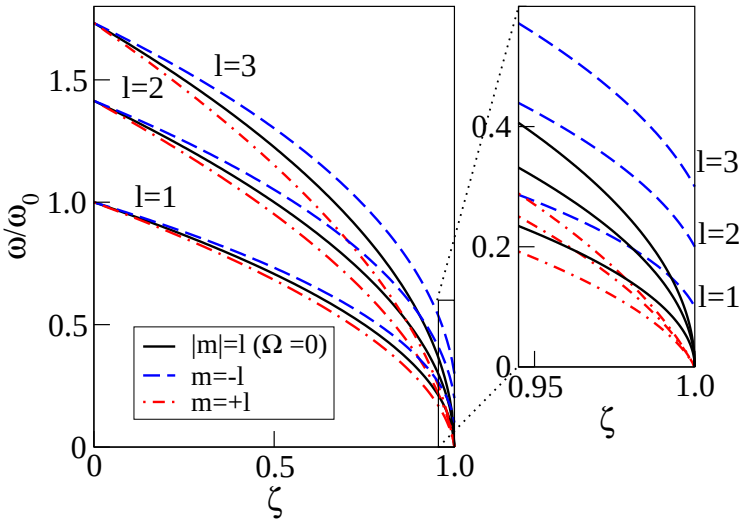

Figure 4.2: The three lowest-energy sets of 2D surface modes ($n_r = 0$, $l = |m| = 1, 2, 3$) for the Rashba Hamiltonian for a weakly interacting Bose condensate. The modes are shown in the single-minimum regime, $0 < \zeta < 1$, for intermediate trapping, $\chi = 0.2$ (the $\Omega_- = 0$ results are for weak trapping $\chi \ll 1$). The Berry curvature breaks the degeneracy and splits the modes.

Complementary Approaches

We now consider two other approaches for calculating the collective mode frequencies of this model. We first discuss a sum rule approach, which was used to investigate 1D spin-orbit coupling in Ref. [215]. We find that the 2D problem is much more

[9]For clarity, we have not shown higher-lying modes in Figure 4.2, although some of these go soft as the effective mass diverges.

difficult and so far we have not been able to explore the regime where the effects of Berry curvature are significant. Instead, we develop an operator method as an alternative approach.

We shall focus in both methods on the dipole mode: the lowest energy mode, which has $n_r = 0$, $l = 1$. For a gas in a harmonic potential, a dipole mode is a centre-of-mass mode, for which a generalised version of Kohn's theorem[217] can be applied[218]. Two-body interactions drop out and the motion of the centre-of-mass is equivalent to that of a single particle. Then the frequency of this mode without Berry curvature is simply equal to the trap frequency (see Eq. 4.6 for $\Omega = 0$ and $M^* = 1$)[38].

4.4 Sum Rules for 2D Rashba Spin-Orbit Coupling

Introduction to Sum Rules

To calculate collective modes directly, we need to solve the full equations of motion of the many-body system. Sum rules provide an ingenious alternative; this approach often only requires knowledge of the ground-state and its properties. The first application of this technique was in the Thomas-Reiche-Kuhn (TRK) sum rule, calculated in 1925 for the interactions of light with atoms[219, 220, 221]. Since then sum rules have found applications in many areas including the solid-state[222], nuclear[223], and particle physics[224].

Sum rules are used to evaluate the moments of the dynamic structure factor, $S_{\hat{F}}(\omega)$. For a sufficiently weak perturbation, the response of the system is directly proportional to the perturbing field and can be described by linear response theory. If the field couples to the system via the linear operator, $\hat{G}$, the perturbing Hamiltonian can be written as[37]:

$$H_{\text{pert}}(t) = -h\hat{G}e^{-i\omega t}e^{\eta t} - h^*\hat{G}^\dagger e^{i\omega t}e^{\eta t} \tag{4.12}$$

where h is the (weak) perturbing field strength, ω is the frequency of the field and η is positive and small so that $H_{\text{pert}}(-\infty) = 0$. This perturbation can cause deviations

from equilibrium in the expectation values of another linear operator, $\hat{F}^\dagger$:

$$\begin{aligned}\delta\langle\hat{F}^\dagger\rangle &= \langle\psi(t)|\hat{F}^\dagger|\psi(t)\rangle - \langle\psi(-\infty)|\hat{F}^\dagger|\psi(-\infty)\rangle \\ &= he^{-i\omega t}e^{\eta t}\chi_{\hat{F}^\dagger,\hat{G}}(\omega) + h^*e^{i\omega t}e^{\eta t}\chi_{\hat{F}^\dagger,\hat{G}^\dagger}(\omega) \end{aligned} \tag{4.13}$$

where $\chi_{\hat{F}^\dagger,\hat{G}}$ is the response function or the dynamic polarizability[10]. If $\hat{F} = \hat{G}$, the result can be written as:

$$\begin{aligned}\chi_{\hat{F}^\dagger,\hat{F}} = \chi_{\hat{F}} &\equiv -\int_{-\infty}^{+\infty} d\omega' \left[\frac{S_{\hat{F}}(\omega')}{\omega - \omega' + i\eta} - \frac{S_{\hat{F}^\dagger}(\omega')}{\omega + \omega' + i\eta}\right] \\ S_{\hat{F}}(\omega) &= \sum_n |\langle 0|\hat{F}|n\rangle|^2\delta(\hbar\omega - \hbar\omega_{n0}) \end{aligned} \tag{4.14}$$

where $|n\rangle$ and $\hbar\omega_{n0} = (E_n - E_0)$ are the eigenstates of the unperturbed Hamiltonian. $S_{\hat{F}}(\omega)$ is the dynamic structure factor (at zero temperature), which gives the excitation spectrum of the operator $\hat{F}$. We can define moments of the dynamic structure factor as[37]:

$$m_p(\hat{F}) = \hbar^{p+1}\int_{-\infty}^{+\infty} d\omega\omega^p S_{\hat{F}}(\omega) = \sum_n (E_n - E_0)^p |\langle 0|\hat{F}|n\rangle|^2. \tag{4.15}$$

These are very useful because they provide a rigorous upper bound on the lowest excitation energy, $\hbar\omega_{\min}$, of the operator $\hat{F}$:

$$(\hbar\omega_{\min})^r \leq \frac{m_p(\hat{F})}{m_{p-r}(\hat{F})}. \tag{4.16}$$

for any value of p and r. This upper bound will become an equality if there is only one excited state (with energy $\hbar\bar{\omega}$), such that $S_{\hat{F}}(\omega) \propto \delta(\hbar\omega - \hbar\bar{\omega})$. For positive values of p, the moments can often be related to commutators or anti-commutators

[10]The form of the response function is found by considering the time evolution of the system under the action of $H_{\text{pert}}(t)$ up to first order in h.

of the operator, $\hat{F}$, with $\hat{H}$, the total Hamiltonian[11]:

$$\begin{aligned} m_1(\hat{F}) &= \frac{1}{2}\langle 0|[\hat{F},[\hat{H},\hat{F}^\dagger]]|0\rangle \\ m_2(\hat{F}) &= \frac{1}{2}\langle 0|\{[\hat{F},\hat{H},],[\hat{H},\hat{F}^\dagger]\}|0\rangle \\ m_3(\hat{F}) &= \frac{1}{2}\langle 0|[[\hat{F},\hat{H}],[\hat{H},[\hat{H},\hat{F}^\dagger]]|0\rangle \end{aligned} \tag{4.17}$$

These sum rules demonstrate how the ground-state can be used to evaluate the dynamical properties and collective excitations of a system. However, moments with $p \geq 1$ are most sensitive to the large ω and short time behaviour[225]. If there is indeed only one excited state, Eq. 4.16 will give the lowest excitation energy regardless of the value of p used. However, usually this is not the case and so p must be chosen with care.

4.4.1 A Sum Rule Approach to the 2D Dipole Mode

We are interested in the dipole mode in the 2D Rashba spin-orbit coupled system. Using moments with $p \geq 1$, gives a large upper bound on the collective mode frequency that is insensitive to the effects of spin-orbit coupling and Berry curvature. This indicates that the single-mode approximation is not valid and that higher energy excitations contribute to the dynamic structure factor. To improve this calculation, we have therefore focused on:

$$\hbar\omega_{\min} \leq \sqrt{\frac{m_{-1}(\hat{D}_{\pm 1})}{m_{-3}(\hat{D}_{\pm 1})}} \tag{4.18}$$

where we have introduced the dipole operator $\hat{D}_{\pm 1} = \hat{X} \mp i\hat{Y}$ (corresponding to the modes $\delta\rho_{\pm 1}$) and the many-body particle operators: $\hat{X} = \sum_i \hat{x}_i$ (all defined at $t = 0$). The moments are sensitive to the low-energy part of the dynamic structure factor, and have been used to investigate the dipole mode in the 1D spin-orbit coupled system[215] described in Section 2.2.1, where there is no Berry curvature. In Appendix D, we derive the moments for the dipole operator and the Hamiltonian

[11] For more detail on when these relations are valid see Ref. [225].

in Eq. 4.10:

$$\begin{aligned} m_{-1}(\hat{D}_{\pm 1}) &= \frac{N}{\omega_0^2 M} \pm \frac{1}{\omega_0^2 \hbar M}\langle 0|\hat{L}_z|0\rangle \\ m_{-3}(\hat{D}_{\pm 1}) &= \frac{N}{M\hbar^2\omega_0^4} \pm \frac{1}{M\hbar^3\omega_0^4}\langle 0|\hat{L}_z|0\rangle + \sum_n \frac{4\lambda_R^2}{\hbar^2\omega_0^4(E_n - E_0)}|\langle 0|\hat{\Sigma}_{\mp}|n\rangle|^2 \\ &\quad \pm \frac{\lambda_R}{\hbar^3\omega_0^4}\langle 0|(\hat{X} + i\hat{Y})\hat{\Sigma}_- + \hat{\Sigma}_+(\hat{X} - i\hat{Y})|0\rangle \end{aligned} \tag{4.19}$$

where N is the number of particles in the ground-state $|0\rangle$, $\hat{\Sigma}_\pm$ are the many-body particle spin raising and lowering operators.

The $m_{-1}(\hat{D}_{\pm 1})$ moment is known as the inverse energy-weighted moment[12]. It is related to the static polarizability as[37]:

$$\begin{aligned} \chi_{\hat{D}_{\pm 1}}(0) &\equiv \chi_{\hat{D}_{\pm 1}}(\omega)_{\omega\to 0} = m_{-1}(\hat{D}_{\pm 1}) + m_{-1}(\hat{D}_{\pm 1}^\dagger) \\ &= m_{-1}(\hat{D}_{\pm 1}) + m_{-1}(\hat{D}_{\mp 1}) = \frac{2N}{\omega_0^2 M} \end{aligned} \tag{4.20}$$

where we have used that $\hat{D}_{\pm 1}^\dagger = \hat{D}_{\mp 1}$. As in the 1D SO case, this is insensitive to both the two-body interactions and the spin-orbit coupling[215].

The moments in Eq. 4.19 depend on both ground-state properties and:

$$\sum_n \frac{|\langle 0|\hat{\Sigma}_{\mp}|n\rangle|^2}{(E_n - E_0)} = m_{-1}(\hat{\Sigma}_{\mp}). \tag{4.21}$$

This quantity is related to the static spin polarizability per particle as: $\chi_{\hat{\Sigma}_{\mp}}(0) = m_{-1}(\hat{\Sigma}_+) + m_{-1}(\hat{\Sigma}_-)$. Guided by this connection, we find that this term can be calculated by applying linear response theory to the ground-state wave function (see Appendix E). Therefore, only knowledge of the ground-state is needed to find an upper bound on the lowest excitation energy (Eq. 4.18). However, this is still non-trivial as the ground-state depends on two-body interactions. In Section 4.4.3, we shall therefore employ an appropriate ansatz for the wave-function. Before this, we shall confirm Eq. 4.19 by exploring the single-particle problem, which can be easily solved numerically.

[12]For the density operator, this is known as the compressibility sum rule, as the static density response can sometimes be related to the thermodynamic compressibility[37].

4.4.2 The Non-Interacting Case

We consider the single-particle Hamiltonian:

$$\hat{h}_0 = \frac{\boldsymbol{p}^2}{2M} + \lambda_R(p_x\hat{\sigma}_y - p_y\hat{\sigma}_x) - \Delta\hat{\sigma}_z + V(x,y). \tag{4.22}$$

The collective modes can be directly calculated from the numerically obtained eigenenergies. This allows us to confirm the expressions in Eq. 4.19. The dipole operator, $\hat{D}^\dagger_{\pm1}$, changes the angular momentum of the system ($m \to m \pm 1$). Therefore, we consider a spin-1/2 particle in a 2D quantum harmonic oscillator potential, where the eigenstates are characterised by the spin, a radial quantum number, n_r, and the azimuthal angular momentum, m. In this basis, we can recast Eq. 4.22 as:

$$\hat{h}_0 = \hbar\omega_0(\hat{a}^\dagger_d\hat{a}_d + \hat{a}^\dagger_g\hat{a}_g + 1)\hat{1} - \hat{\sigma}_z\Delta + \lambda_R\sqrt{M\hbar\omega_0}\left[\hat{\sigma}_+(\hat{a}^\dagger_g - \hat{a}_d) + \hat{\sigma}_-(\hat{a}_g - \hat{a}^\dagger_d)\right] \tag{4.23}$$

where we have introduced the 2D operators:

$$\begin{aligned}
\hat{\sigma}_+ &= \tfrac{1}{2}(\hat{\sigma}_x + i\hat{\sigma}_y) \qquad & \hat{\sigma}_- &= \tfrac{1}{2}(\hat{\sigma}_x - i\hat{\sigma}_y)\\
\hat{a}_d &= \tfrac{1}{\sqrt{2}}(\hat{a}_x - i\hat{a}_y) \qquad & \hat{a}_g &= \tfrac{1}{\sqrt{2}}(\hat{a}_x + i\hat{a}_y)\\
\hat{a}^\dagger_d &= \tfrac{1}{\sqrt{2}}(\hat{a}^\dagger_x + i\hat{a}^\dagger_y) \qquad & \hat{a}^\dagger_g &= \tfrac{1}{\sqrt{2}}(\hat{a}^\dagger_x - i\hat{a}^\dagger_y)
\end{aligned}$$

based on the usual 1D ladder operators:

$$\hat{a}_x = \sqrt{\frac{M\omega_0}{2\hbar}}\left(\hat{x} + \frac{i}{M\omega_0}\hat{p}_x\right), \qquad \hat{a}^\dagger_x = \sqrt{\frac{M\omega_0}{2\hbar}}\left(\hat{x} - \frac{i}{M\omega_0}\hat{p}_x\right) \tag{4.24}$$

(and similarly for y). The Hamiltonian can be visualised in Figure 4.3. The azimuthal angular momentum is $\hat{a}^\dagger_d\hat{a}_d - \hat{a}^\dagger_g\hat{a}_g = m$. In this basis, the dipole operators can be written as:

$$\hat{d}_{+1} = \hat{x} - i\hat{y} = \sqrt{\frac{\hbar}{M\omega_0}}(\hat{a}_d + \hat{a}^\dagger_g), \qquad \hat{d}_{-1} = \hat{x} + i\hat{y} = \sqrt{\frac{\hbar}{M\omega_0}}(\hat{a}_g + \hat{a}^\dagger_d) \tag{4.25}$$

The spin-orbit interaction couples infinite ladders of states of increasing energy. The lowest six states in the ground-state ladder is shown in Figure 4.3. For sufficiently weak λ_R, the Hamiltonian can be diagonalised numerically to high accuracy with a finite number of states. The dipole frequency can be directly determined by

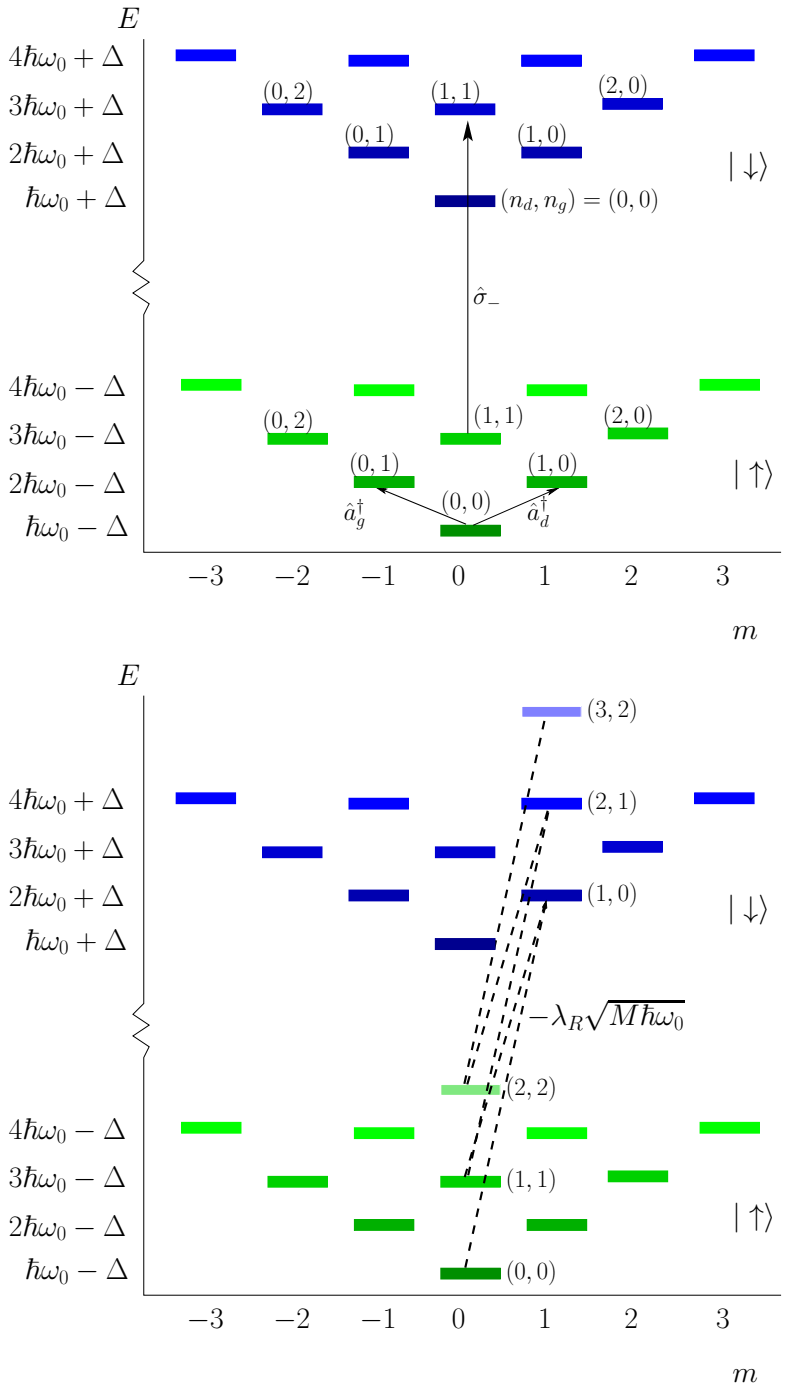

Figure 4.3: (**Above**) A schematic of the lowest single-particle, 2D harmonic oscillator energy levels for each spin state. Each state can be labelled by the spin and (n_d, n_g), where $n_d = \hat{a}_d^\dagger \hat{a}_d$ and $n_g = \hat{a}_g^\dagger \hat{a}_g$. These 2D operators are defined in the main text and are related to the azimuthal angular momentum as: $\hat{a}_d^\dagger \hat{a}_d - \hat{a}_g^\dagger \hat{a}_g = m$. Note that $\Delta \gtrsim \hbar\omega_0$ (i.e. $\chi \lesssim 1$). (**Below**) The spin-orbit coupling flips the spin and couples states with different azimuthal momentum. This links the states in infinite ladders (shown here are the first six states of the ground-state ladder). To find the energies with spin-orbit coupling, we numerically diagonalise the single-particle Hamiltonian within each ladder.

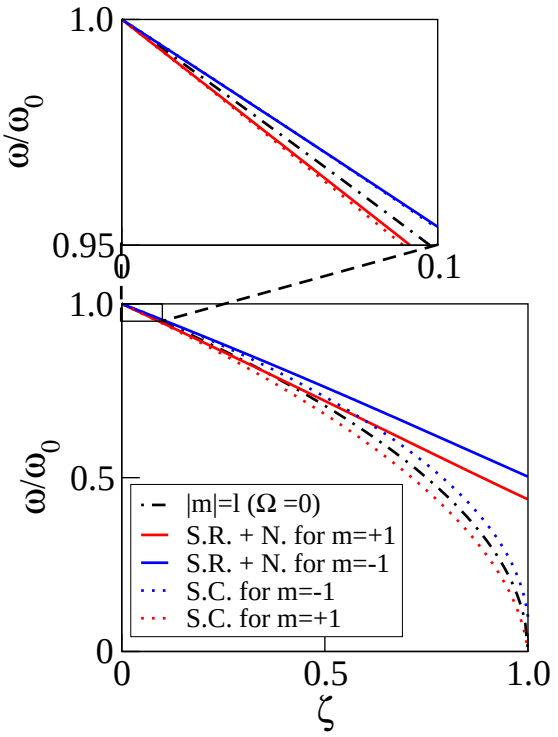

Figure 4.4: The dipole mode for the 2D Rashba Hamiltonian in the non-interacting case ($n_r = 0$, $|m| = 1$). The modes are shown in the single-minimum regime, $0 < \zeta < 1$, for intermediate trapping, $\chi = 0.2$ (the $\Omega_- = 0$ results are for weak trapping $\chi \ll 1$). The dotted lines indicate the semiclassical results (S.C.), while the smooth lines are the sum rule and numerical results (S.R. & N.). The red lines indicate the mode excited by $\hat{d}_{+1}$ and the blue those excited by $\hat{d}_{-1}$. The splitting due to Berry curvature appears for all approaches, with excellent agreement for very small ζ.

comparing the numerical energies of the ground and first excited states.

We compare this with the sum rule approach (Eq. 4.19):

$$\begin{aligned} m_{-1}(\hat{d}_{\pm 1}) &= \frac{N}{M\omega_0^2} \pm \frac{1}{\hbar M\omega_0^2}\langle 0|\hat{l}_z|0\rangle \\ m_{-3}(\hat{d}_{\pm 1}) &= \frac{N}{M\hbar^2\omega_0^4} \pm \frac{1}{M\hbar^3\omega_0^4}\langle 0|\hat{l}_z|0\rangle + \sum_n \frac{4\lambda_R^2}{\hbar^2\omega_0^4(E_n - E_0)}|\langle 0|\hat{\sigma}_\mp|n\rangle|^2 \\ &\quad \pm \frac{\lambda_R}{\hbar^2\omega_0^4 M}\sqrt{\frac{M}{\hbar\omega_0}}\langle 0|(\hat{a}_g + \hat{a}_d^\dagger)\hat{\sigma}_- + \hat{\sigma}_+(\hat{a}_g^\dagger + \hat{a}_d)|0\rangle. \end{aligned} \tag{4.26}$$

These are computed from the numerically calculated eigenstates. For $\chi \lesssim 0.3$, the sum rule approach and the direct numerical frequencies agree closely. These two sets of results are compared in Figure 4.4 with the semiclassical approach[13]. All three calculations show a clear splitting of the modes due to the Berry curvature. The energy splitting between dipole modes from the semiclassical approximation is $\frac{\delta\omega}{\omega_0} = \frac{1}{2}\zeta\chi$ (Eq. 4.6). For small ζ, there is good quantitative agreement between this and the other two approaches[14]. For large $\zeta \simeq 1$, the sum rule and numerical

[13] In the non-interacting case, we apply the semiclassical equations rather than the hydrodynamic approach. Using $\boldsymbol{F} = -\boldsymbol{\nabla}V$ in Eq. 3.3, we recover the hydrodynamic frequencies for the dipole mode (Eq. 4.6).

[14] Using second-order perturbation theory in λ_R on the energy state scheme of Figure 4.3, we find

approach diverge significantly from the semiclassical approach. This is because we assume semiclassically that the cloud has a large width and so is well-described by the properties of the minimum in the energy dispersion. However, as the dispersion flattens and the effective mass diverges, the width of the non-interacting cloud in a trap becomes narrower, and this approximation breaks down.

4.4.3 The Interacting Case

To include interactions, we look for an appropriate ansatz for the ground-state. The simplest ansatz would be:

$$\Psi = \begin{pmatrix} \psi_1 \\ \psi_2 \end{pmatrix} = f\left(\frac{r}{R}\right) \begin{pmatrix} 1 \\ 0 \end{pmatrix} \tag{4.27}$$

where $f\left(\frac{r}{R}\right)$ encodes the spatial variation due to the trap[15]. This assumes that in the ground-state, all particles are in the $|\uparrow\rangle$ state. However, the spin-orbit coupling mixes the spin states; this is therefore a bad ansatz, unable to capture even the effective mass behaviour for a vanishing trap ($\chi \to 0$). A better choice is:

$$\Psi = \begin{pmatrix} \sqrt{\frac{\mu+\Delta-V(x,y)}{g_{2D}}} \\ \frac{\lambda_R}{4\Delta\sqrt{g_{2D}}} \frac{M\omega_0^2\hbar}{\sqrt{\mu+\Delta-V(x,y)}} (x+iy) \end{pmatrix} \tag{4.28}$$

where μ is the chemical potential, normalised so that there are N particles in component ψ_1 within the Thomas-Fermi volume. This ansatz can be justified by considering the interacting Gross-Pitaevskii equations under the constraint that the occupation of ψ_2 is still much less than that of ψ_1. For the details of this ansatz and the accompanying sum rule calculation see Appendix E. The dipole mode frequencies within the sum rule approach (Eq. 4.18) then become:

$$\omega_{\pm 1}^2 = (1-\zeta)\omega_0^2 = \frac{M}{M^*}\omega_0^2, \tag{4.29}$$

the splitting $2\chi\zeta/(4-\chi^2)$. This reduces to $\frac{\delta\omega}{\omega_0} = \frac{1}{2}\zeta\chi$ for sufficiently small χ.

[15]This ansatz was sufficient to capture the simpler 1D SO coupling behaviour in Ref. [215].

(i.e. the $|m| = 1$, $\Omega = 0$ line in Figure 4.2). Unfortunately, the ansatz is still insufficiently accurate to discern the effects of Berry curvature. This is because the splitting due to Berry curvature is proportional to $\chi = \hbar\omega_0/\Delta$. As Δ is the Zeeman energy splitting the spin-states, increasing χ breaks our assumption that there are a negligible number of atoms in the $|\downarrow\rangle$ component.

We have not been able to extend the sum rule approach beyond Eq. 4.29, to the regime where the effects of Berry curvature are significant. While even the simplest ansatz (Eq. 4.27) was able to capture the important physics of 1D spin-orbit coupling[215], we see that the 2D problem is substantially more difficult and a much more sophisticated ansatz is required. We therefore leave this problem as an open question. Instead, we now develop an alternative approach, which shares many of the advantages of the sum rules, but avoids this drawback.

4.5 Dipole Operator Approach

We derive the frequencies of the dipole mode using an operator approach, which captures the effects of Berry curvature. We calculate the Heisenberg equations of motion for an operator, $\hat{F}$:

$$\dot{\hat{F}} = \frac{i}{\hbar}[\hat{H}, \hat{F}] + \frac{\partial \hat{F}}{\partial t}. \tag{4.30}$$

In general, the commutator, $[\hat{H}, \hat{F}]$, generates terms involving other operators. By considering the equations of motion of these operators too, we seek a closed set of equations that can be solved for the mode frequencies.

For particles in a quadratic band minimum, the dipole mode is a centre-of-mass oscillation[217, 218]. It is therefore unaffected by interactions (which depend only on interparticle separations). As we now show, the dipole mode remains a centre-of-mass oscillation for non-zero Berry curvature. Hence, interactions can be neglected provided they do not excite particles to high-energy states which lie beyond the effective mass approximation, which we now assume. For a BEC in an optical lattice, we require interactions to be sufficiently weak that $\xi \gg a$, where $\xi = (\hbar^2/2M\rho_0 g)^{1/2}$ is the healing length and a is the lattice spacing. For the 2D Rashba model, the

effective mass approximation breaks down for momenta $p \simeq \Delta/\lambda_R$, and so we require that the healing length is much greater than $\hbar\lambda_R/\Delta$.

We first apply the dipole operator method to the 2D Rashba model, where we confirm the splitting of the dipole modes due to Berry curvature. In Appendix F, we also calculate the mode for 1D spin-orbit coupling. While this system does not have Berry curvature, we show that in this system too, the dipole operator method captures the behaviour expected from a hydrodynamic and a sum rule approach. Finally, we discuss a general multi-band Hamitlonian, where we see how Berry curvature effects arise naturally as the next-order correction after the effective mass.

4.5.1 2D Rashba Spin-Orbit Coupling

We begin from the full many-body Hamiltonian in Eq. 4.10. As $\hat{D}_{\pm1}$ commutes with the interacting term, the interactions drop out and the centre of mass motion is equivalent to that of a single particle. The Heisenberg equations of motion are then:

$$\begin{aligned}
\dot{\hat{D}}_{+1} &= \frac{1}{M}\hat{P}_{+1} + \frac{2i\lambda_R}{\hbar}\hat{S}_{+1} \\
\dot{\hat{P}}_{+1} &= -\omega_0^2 M \hat{D}_{+1} \\
\dot{\hat{S}}_{+1} &= \frac{i\lambda_R}{2}\sum_i (-2ip_x\hat{\sigma}_z + 2p_y\hat{\sigma}_z) + \frac{2i\Delta}{\hbar}\hat{S}_{+1}
\end{aligned} \tag{4.31}$$

where $\hat{P}_{+1} = \hat{P}_x - i\hat{P}_y$ and $\hat{S}_{+1} = \frac{\hbar}{2}(\hat{\Sigma}_x - i\hat{\Sigma}_y)$. Without approximations, this set of operator equations does not close, but contains products of the momentum and spin. We assume that the atoms are in the lower band minimum. Then we can replace the spin operator, $\hat{\sigma}_z$ with the expectation value at this point, $\langle 0|\sigma_z|0\rangle \simeq 1$, where we have neglected terms of order $1/\Delta^2$. Then:

$$\frac{i\lambda_R}{2}\sum_i (-2ip_x\hat{\sigma}_z + 2p_y\hat{\sigma}_z) \simeq \lambda_R\hat{P}_+. \tag{4.32}$$

Then we have a set of three coupled equations. Using the approximation again that we neglect terms of order $1/\Delta^2$, we can further reduce this to two equations. We

find:

$$\begin{aligned} -i\omega\hat{D}_{+1} &= \left(\frac{1}{M} - \frac{2\lambda_R^2}{(\hbar\omega + 2\Delta)}\right)\hat{P}_{+1} \simeq \left(\frac{1}{M} - \frac{\lambda_R^2}{\Delta} - \frac{\lambda_R^2\hbar\omega}{2\Delta^2}\right)\hat{P}_{+1} \\ -i\omega\hat{P}_{+1} &= -\omega_0^2 M\hat{D}_{+1} \end{aligned} \tag{4.33}$$

where we have substituted in for $\hat{S}_{+1}$ and expanded to first order in $\hbar\omega/2\Delta$. We have also taken the operators to vary harmonically as $e^{-i\omega t}$. Similar equations can be found for $\hat{D}_{-1}$. Then the dipole mode frequencies are:

$$\omega_{\pm 1}^2 = \left(\frac{1}{M} - \frac{\lambda_R^2}{\Delta} \mp \frac{\lambda_R^2\hbar\omega}{2\Delta^2}\right)\omega_0^2 M = \frac{M}{M^*} \mp \frac{\Omega\omega M\omega_0^2}{\hbar} \tag{4.34}$$

where we have used the effective mass and Berry curvature introduced in Section 4.3. This therefore confirms the hydrodynamic results (Eq. 4.6) for the dipole mode. In Appendix F, we apply this approach to the 1D spin-orbit coupled Hamiltonian, where we reproduce theoretical results from a hydrodynamic and sum rule approach.

4.5.2 General Multi-Band Hamiltonian

For the particular case of the dipole mode, we now show how the effects of Berry curvature arise naturally for a very general multi-band system. We assume that the minimum of the lowest band is at a high symmetry point (e.g. the Brillouin zone centre, $\boldsymbol{p} = \boldsymbol{0}$). We choose axes such that the local Berry curvature is $\Omega\hat{\boldsymbol{z}}$, and discuss motion in the xy plane (motion along z decouples). The single-particle Hamiltonian is $H = -\frac{\hbar^2}{2M}\boldsymbol{\nabla}^2 + V(\boldsymbol{r}) + U(\boldsymbol{r})$, where $U(\boldsymbol{r})$ is the periodic lattice potential. Following the usual effective mass theory[226], we expand the wave function in terms of functions $e^{i\boldsymbol{k}\cdot\boldsymbol{r}}|n\rangle$, where $|n\rangle \equiv |n\boldsymbol{0}\rangle$ is the Bloch function of the n-th band at $\boldsymbol{p} = \boldsymbol{0}$. We find

$$\hat{H} = \sum_n \left(E_n + \frac{\hbar^2|\hat{\boldsymbol{k}}|^2}{2M} + \frac{1}{2}M\omega_0^2|\hat{\boldsymbol{x}}|^2\right)|n\rangle\langle n| + \sum_{\alpha,n,n'} \frac{\hbar\hat{k}^\alpha}{M}\pi_{n,n'}^\alpha |n\rangle\langle n'| \tag{4.35}$$

where E_n is the n-th band energy at the zone centre, and α runs over spatial dimensions. The operator $\hbar\hat{\boldsymbol{k}}$ is the crystal momentum (with eigenvalues $\hbar\boldsymbol{k}$ for the states $e^{i\boldsymbol{k}\cdot\boldsymbol{r}}|n\rangle$) and $\hat{\boldsymbol{x}}$ is the conjugate crystal position. The last term in $\hat{H}$ is of the

familiar "$\boldsymbol{k}\cdot\boldsymbol{p}$" form [226], with $\pi^\alpha_{n,n'} \equiv \langle n|\hat{p}^\alpha|n'\rangle$ the interband matrix elements[16] of $\hat{p}$.

For a quadratic band minimum, the Heisenberg equations of motion are then:

$$\begin{aligned}
\dot{\hat{X}}^\alpha &= \frac{1}{M}\hat{P}^\alpha + \frac{1}{M}\sum_{n,n'}\hat{\Pi}^\alpha_{nn'} \\
\dot{\hat{P}}^\alpha &= -M\omega_0^2\hat{X}^\alpha \\
\dot{\hat{\Pi}}^\alpha_{nn'} &= \frac{i}{\hbar}(E_n - E_{n'})\hat{\Pi}^\alpha_{nn'} + \frac{i}{\hbar}\frac{\hat{P}^\beta}{M}\sum_j \pi^\alpha_{nn'}\left(\pi^\beta_{jn}|j\rangle\langle n'| - \pi^\beta_{n'j}|n\rangle\langle j|\right)
\end{aligned} \tag{4.36}$$

for the crystal position, $\hat{X}^\alpha \equiv \hat{x}^\alpha\sum_n |n\rangle\langle n|$, crystal momentum, $\hat{P}^\alpha \equiv \hbar\hat{k}^\alpha\sum_n |n\rangle\langle n|$, and Bloch momentum, $\hat{\Pi}^\alpha_{nn'} \equiv \pi^\alpha_{nn'}|n\rangle\langle n'|$ (all defined at $t=0$).

These equations of motion describe coupling of motion of the centre-of-mass of the atoms to interband transitions. We now again assume that all interband transition energies $E_n - E_0$ are large compared to $\hbar\omega$, in which case we can approximate the last line, replacing $\hat{P}^\beta\hat{O}$ with $\hat{P}^\beta\langle 0|\hat{O}|0\rangle$. (This assumes that all atoms are in the lowest band, $n=0$.) The last line becomes $\propto \hat{P}^\beta\left(\pi^\beta_{0n}\pi^\alpha_{n0}\delta_{n'0} - \pi^\beta_{n'0}\pi^\alpha_{0n'}\delta_{n0}\right)$, such that only $\hat{\Pi}^\alpha_{n0}$ and $\hat{\Pi}^\alpha_{0n'}$ couple to $\hat{P}$. Taking the operators to vary harmonically with $e^{-i\omega t}$, and eliminating $\hat{\Pi}^\alpha_{nn'}$, we find:

$$\begin{aligned}
-i\quad & \omega\hat{P}^\alpha = -M\omega_0^2\hat{X}^\alpha \\
-i\quad & \omega\hat{X}^\alpha \simeq \frac{1}{M}\hat{P}^\alpha - \frac{\hat{P}^\beta}{M^2}\sum_{n>0}\left[\frac{\pi^\beta_{0n}\pi^\alpha_{n0}}{[\hbar\omega + (E_n - E_0)]} - \frac{\pi^\alpha_{0n}\pi^\beta_{n0}}{[\hbar\omega - (E_n - E_0)]}\right]
\end{aligned} \tag{4.37}$$

We expand this to first order in $\hbar\omega/(E_n - E_0)$ and find:

$$\begin{aligned}
-i\omega\hat{X} &\simeq \left(\frac{1}{M^*}\right)_{xx}\hat{P}^x + \left(\frac{1}{M^*}\right)_{xy}\hat{P}^y + \frac{i\omega\Omega}{\hbar}\hat{P}^y \\
-i\omega\hat{Y} &\simeq \left(\frac{1}{M^*}\right)_{yy}\hat{P}^y + \left(\frac{1}{M^*}\right)_{yx}\hat{P}^x - \frac{i\omega\Omega}{\hbar}\hat{P}^x
\end{aligned} \tag{4.38}$$

where we have introduced the effective mass [227] and Berry curvature [12] for the

[16] Note that $\pi^\alpha_{n,n} = M(\partial E_n/\partial p^\alpha) = 0$ at a band minimum.

lowest band at the Brillouin zone centre:

$$\left(\frac{1}{M^*}\right)_{\alpha\beta} \equiv \frac{1}{M}\delta_{\alpha\beta} - \frac{1}{M^2}\sum_{n>0}\frac{\pi^\beta_{0n}\pi^\alpha_{n0} + \pi^\alpha_{0n}\pi^\beta_{n0}}{(E_n - E_0)}$$
$$\Omega \equiv \frac{i\hbar^2}{M^2}\sum_{n>0}\frac{\pi^x_{0n}\pi^y_{n0} - \pi^y_{0n}\pi^x_{n0}}{(E_n - E_0)^2}. \tag{4.39}$$

This expression for Ω can be derived from Eq. 4.3 using the relation $\langle n|\frac{\partial H}{\partial \boldsymbol{p}}|n'\rangle = \langle\frac{\partial n}{\partial \boldsymbol{p}}|n'\rangle(E_n - E'_n)$ [12]. From Eq. 4.38, we calculate the dipole frequencies of $\hat{D}_{\pm1} = \hat{X} \mp i\hat{Y}$ (corresponding to the modes $\delta\rho_{\pm1}$). For an isotropic effective mass, the dipole mode frequencies are given by Eq. 4.6 (with $n_r = 0$, $l = 1$ and $m = \pm1$), confirming the hydrodynamic result. Moreover, since all atoms oscillate in the same way, the dipole mode remains a centre-of-mass oscillation, so this result is independent of the regime or equation of state. Our derivation shows that the Berry curvature appears as the next-order correction after the effective mass[17].

4.6 Size of the Effects of Berry Curvature on Collective Modes

Finally we discuss the size of the effects of Berry curvature on collective modes. We illustrate this for the Harper-Hofstadter model of a tight-binding lattice with a flux $n_\phi = 1/q$ (where q is an integer) per plaquette of dimensions $a \times a$ [99]. The magnetic unit cell contains one flux quantum, so its area is $A = a^2/n_\phi$. The corresponding magnetic BZ has an area $A_{\mathrm{BZ}} = (2\pi)^2 n_\phi/a^2$. The average Berry curvature, $\bar{\Omega}$, scales as $\propto 1/n_\phi$ (because $\bar{\Omega}A_{\mathrm{BZ}} = 2\pi C$, where C is the Chern number, which is $C = 1$ in this case). Therefore, the mode splitting due to Berry curvature is *bigger* for smaller flux density (Eq. 4.6). Decreasing n_ϕ will maximise the size of this effect, so long as the energy gap between bands ($\propto n_\phi$) is always greater than $\hbar\omega_0$. Beyond this limit, our assumption that the occupation of higher bands is negligible breaks down and Eq. 4.6 will not be valid.

The effects of the Berry curvature can be large even when the flux per unit cell

[17] Away from high symmetry points, there can also be cubic corrections to the effective mass which will scale on the same order as the Berry curvature ($\propto 1/(E_n - E_0)^2$) as discussed further in Appendix G.

is of order 1, as for the optical flux lattices [96, 107]. For example, we take ^{87}Rb atoms condensed in the minimum of the $F = 1$ two-photon coupling scheme (with the parameters of Fig. 4(a) in Ref. [107]). The splitting between two surface modes with $m = \pm l$ then is $\delta\omega/\omega_0 \approx 3.4\% \times l$ for $\omega_0/2\pi = 150$Hz (Eq. 4.6). For the quadrupole modes (with $m = \pm 2$), $\delta\omega/2\pi \approx 10$Hz, which is larger than measured damping rates and should be experimentally observable [193]. Hence, measurements of the collective mode frequencies of a BEC can efficiently be used to characterise geometrical properties of these novel lattices.

4.7 Conclusion

In conclusion, we have shown that Berry curvature has important effects on the collective modes of ultracold gases. We have derived the splitting of these modes within the hydrodynamic approach for a BEC and extended the results to other systems using a general polytropic equations of state. We have analysed important classes of modes, and shown that the splitting due to Berry curvature is independent of the system. Our results were illustrated on the 2D Rashba model with a Zeeman field. We also analysed the dipole mode in this model using a sum rule approach and dipole operator method. For a general multi-band system, we have then shown how the Berry curvature arises naturally as the next-order correction to the collective modes, after the effective mass. These effects can be large and should be readily detectable with current experimental capabilities. Their observation would allow a characterisation of the geometrical properties of BECs in topological energy bands.

Chapter 5

Skyrmion-antiSkyrmion Pairs in Ultracold Atomic Gases

In this chapter we investigate the *dynamical* properties of topological excitations in 2D spinor BECs. We focus on a two-component BEC, which admits configurations with the topology of skyrmions[44]. We study a branch of uniformly propagating solitary waves, which at large momentum are skyrmion-antiskyrmion pairs moving perpendicular to the line separating their centres. As introduced in Section 1.2.2, trapped BECs can be imaged and controlled with high temporal and spatial resolution[61, 63] and skyrmion-antiskyrmion pairs can be imprinted on a BEC with holographically produced light beams[57]. Applied to a trapped gas, this imprinting technique would allow for a full study of the dynamical properties of these excitations[57].

We begin in Section 5.1 by introducing the Gross-Pitaveskii energy functional for a 2D two-component Bose-Einstein condensate. We show how this can be usefully re-written in the pseudo-spin representation, and we specify the physical constraints on the dynamics of the condensate. In Section 5.2, we use these conservation laws to identify and study a branch of uniformly propagating solitary waves, which, at high momentum, can be viewed as skyrmion-antiskyrmion pairs. We study these solitary waves for a range of interaction regimes and show that, for experimentally relevant cases, there is a transition to spatially extended spin-wave states at low momentum. We also show how our results can be understood by analogy to the

2D ferromagnet[228], establishing the importance of topology in describing these systems. This work was published as Ref. [3].

5.1 The Gross-Pitaevskii Energy Functional for a 2D two-component BEC

We study the Gross-Pitaevskii energy functional in 2D for a two-component condensate of atoms:

$$E = \int d^2\boldsymbol{r} \sum_{i,\alpha} \frac{\hbar^2}{2M_i} |\nabla_\alpha \psi_i|^2 + \frac{1}{2} \sum_{i,j} g_{ij} |\psi_i|^2 |\psi_j|^2 \,. \tag{5.1}$$

(Summation convention is assumed throughout, with i, j running over the two components and α, β over the two spatial dimensions.) We neglect the trapping potential, and study the properties in the central region of the cloud where the density is uniform. Since skyrmions can be imprinted by exciting atoms between different hyperfine states(Section 1.2.2), we take $M_i = M_j$ for simplicity. The interaction parameters g_{ij} for a quasi-2D harmonically confined gas can be expressed as $g_{ij} = (\hbar^2\sqrt{8\pi}a_{ij})/Ma_z$[229], where a_{ij} are the s-wave scattering lengths and a_z is the oscillator length along the kinematically frozen axis. We are guided by the experimentally relevant system of ^{87}Rb in the $|1,-1\rangle$ and $|2,1\rangle$ hyperfine states[57], hereafter denoted component 1 and 2 respectively. For these states, $g_{11} \sim g_{12} \sim g_{22}$ and so stationary solutions vary on lengthscales much larger than the healing length, allowing us to neglect variations in the total density[54].

5.1.1 The Pseudo-Spin Representation

The two-component condensate wavefunction is a spinor which we choose to parameterise as:

$$\begin{pmatrix} \psi_1 \\ \psi_2 \end{pmatrix} = \sqrt{\rho_0} \begin{pmatrix} \chi_1 \\ \chi_2 \end{pmatrix} = \sqrt{\rho_0} \begin{pmatrix} \cos(\theta/2) e^{i(\epsilon - \phi/2)} \\ \sin(\theta/2) e^{i(\epsilon + \phi/2)} \end{pmatrix} \tag{5.2}$$

where ρ_0 is the total density and $\theta \in [0, \pi]$, $\phi \in [0, 2\pi)$ and $\epsilon \in [0, 2\pi)$ are functions of position $\boldsymbol{r}$. We can then define the local spin as:

$$\vec{\ell} = \chi^\dagger \vec{\sigma} \chi = \sin\theta(\cos\phi\hat{\vec{x}} + \sin\phi\hat{\vec{y}}) + \cos\theta\hat{\vec{z}} \tag{5.3}$$

where $\vec{\sigma}$ is the vector of Pauli matrices. Following [55, 52], we use this to recast Eq. 5.1:

$$E = \int d^2\boldsymbol{r} \left[\frac{\hbar^2\rho_0}{8M}(\boldsymbol{\nabla}\vec{\ell})^2 + \frac{\rho_0 M \boldsymbol{v}_s^2}{2} + \frac{\rho_0^2}{2}(c_0 + c_1\ell_z + c_2\ell_z^2) \right] \tag{5.4}$$

where $\boldsymbol{v}_s = (2\boldsymbol{\nabla}\epsilon - \cos\theta\boldsymbol{\nabla}\phi)\hbar/2m$ is the superfluid velocity and $c_0 = (g_{11} + g_{22} + 2g_{12})/4$, $c_1 = (g_{11} - g_{22})/2$ and $c_2 = (g_{11} + g_{22} - 2g_{12})/4$. The first term of Eq. 5.4 corresponds to the non-linear σ model, previously studied for a ferromagnet[228]. The second term is the hydrodynamic kinetic energy of the superfluid flow. The c_0 term is a uniform energy shift, while, in the analogy to the ferromagnet, the c_1 and c_2 terms can be interpreted as a magnetic field and an anisotropy respectively[52]. c_1 just shifts the chemical potentials for N_1 and N_2, so, like c_0, it has no physical consequences and we henceforth define the energy (Eq. 5.4) with $c_0 = c_1 = 0$.

As skyrmions can be imprinted by selectively exciting atoms from one hyperfine component into a second[57], we consider only solutions with all atoms in a single component at large radii. In this case, $\vec{\ell}(\boldsymbol{r})$ is uniform for $\boldsymbol{r} \to \infty$. The local spin vector field is then equivalent to a mapping from $S^2 \to S^2$ (Figure 5.1). The topological index of this mapping is an integer counting how many times the local

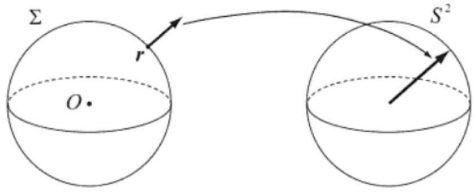

Figure 5.1: Figure taken from Ref. [7]. A mapping from the real space two-sphere, Σ, to the Bloch sphere for $\vec{\ell}(\boldsymbol{r})$. Real space can be represented as a two-sphere because we are concerned with solutions that have all atoms in one component at large distances. These solutions have finite energy and a uniform $\vec{\ell}(\boldsymbol{r})$ as $\boldsymbol{r} \to \infty$. Under these circumstances, the 2D plane is topologically equivalent to the two-sphere[230].

spin vector wraps over the sphere[230]:

$$Q = \frac{1}{8\pi}\int d^2\boldsymbol{r}\varepsilon_{\alpha\beta}(\partial_\beta\vec{\ell}\times\partial_\alpha\vec{\ell})\cdot\vec{\ell} \tag{5.5}$$

where $\varepsilon_{\alpha\beta}$ is the 2D Levi-Civita symbol. A skyrmion is a configuration which has $Q = 1$, while an anti-skyrmion has $Q = -1$.

5.1.2 Dynamics of the Condensate and Conserved Quantities

The condensate dynamics are described by the two coupled time-dependent Gross-Pitaevskii equations:

$$i\hbar\frac{\partial\chi_i}{\partial t} = \left[-\frac{\hbar^2}{2M}\boldsymbol{\nabla}^2 + g_{ii}\rho_0|\chi_i|^2 + g_{ij}\rho_0|\chi_j|^2\right]\chi_i\,. \tag{5.6}$$

These equations conserve particle number in each component, N_i, as well as the energy. We will look at configurations where $\chi \to \chi_\infty \equiv (1,0)^{\mathrm{T}}$ at spatial infinity, so that the particle number in component 2

$$N_2 = \rho_0\int d^2\boldsymbol{r}|\chi_2|^2 \tag{5.7}$$

is finite, and related to the excitation size. (Since ρ_0 is constant, N_1 is automatically conserved when N_2 is conserved.) Two additional important conserved quantities are the topological index, which we re-write here in terms of the wave function, and the linear momentum, P_α:

$$Q = \int d^2\boldsymbol{r}q(\boldsymbol{r}) \tag{5.8}$$

$$P_\alpha = 2\hbar\pi\rho_0\varepsilon_{\alpha\beta}\int d^2\boldsymbol{r}r_\beta q(\boldsymbol{r}) \tag{5.9}$$

where $q(\boldsymbol{r}) = \frac{1}{2\pi i}\varepsilon_{\alpha\beta}\nabla_\alpha\chi_i^*\nabla_\beta\chi_i$ is the topological density[230]. (The definition of momentum is related to the hydrodynamical impulse of classical fluid dynamics[231].) As we consider the condition $\chi \to \chi_\infty$ at spatial infinity, the topological index, Q, is an integer.

For given P_α, Q and N_2, we find the wavefunction configurations which minimise

the energy E. The time evolution of these configurations follows from Eq. 5.6 as:

$$\frac{\partial \chi_i}{\partial t} = -v_\alpha \nabla_\alpha \chi_i - i\omega \chi_2 \delta_{i2} \tag{5.10}$$

where v_α and ω are Lagrange parameters, introduced to enforce the constraints on P_α and N_2. It is straightforward to demonstrate that this is consistent with travelling wave configurations, which uniformly propagate through the system with a constant velocity v_α, while the local spin precesses around ℓ_z at angular frequency ω. The "energy dispersion" $E^*_Q(P_\alpha, N_2)$ is the minimal energy for given P_α, N and Q, and so:

$$v_\alpha = \left(\frac{\partial E^*_Q}{\partial P_\alpha}\right)_{N_2} \qquad \omega = -\frac{1}{\hbar}\left(\frac{\partial E^*_Q}{\partial N_2}\right)_{P_\alpha}. \tag{5.11}$$

Following Ref. [228], we note that under translation, $\chi_i(r_\alpha) \to \chi_i(r_\alpha + R_\alpha)$, the momentum transforms as $P_\alpha \to P_\alpha - QR_\alpha$. Therefore, for a system which is translationally invariant, as we assume here, $E^*_{Q\neq 0}(P_\alpha, N_2) = E^*_{Q\neq 0}(0, N_2)$. Propagating solutions with non-zero velocity therefore exist only for Q=0. Solutions with Q=1, which include static skyrmions, were previously theoretically studied in Ref. [55]. Henceforth we restrict our analysis to the topological subspace Q=0, and drop the subscript Q. We shall find that some of the extremal configurations are localised, and these are therefore the uniformly propagating solitary waves[228, 25].

5.2 A Uniformly Propagating Branch of Solitary Waves

We have investigated the discretised energy functional $E^*(P_\alpha, N_2)$ numerically over a square lattice of length L. Here, we present results for a system of size 115 by 115, with the boundaries set to $\chi = \chi_\infty$. The scale-invariance of the theory requires that under a scaling λ, $E^*(P, N_2, L) = E^*(P\lambda, N_2\lambda^2, L\lambda)$[228]. This implies that the energy can only depend on the "scaled momentum" $p = P/\sqrt{N_2\rho_0\hbar^2}$, the "boundary parameter" $\eta = N_2/(\rho_0 L^2)$ and the "anisotropy" $\tilde{c}_2 = N_2 c_2 M/\hbar^2$. Hereafter we use these dimensionless variables, and express the energy in units of $\hbar^2\rho_0/M$. The results for an infinite system are obtained by taking the limit $\eta \to 0$.

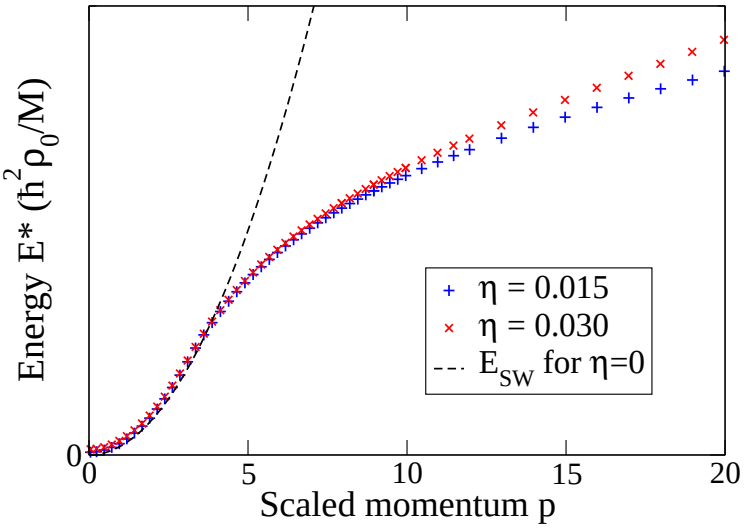

Figure 5.2: The energy dispersion of a two-component condensate for η =0.015 and 0.030 and $\tilde{c}_2$=0. The energy for a system of free spin waves, Eq.5.12, is shown for comparison in the limit of an infinite system, $\eta \to 0$.

5.2.1 Dynamical Properties without Anisotropy

Figure 5.2 shows the minimum energy as a function of p for $\tilde{c}_2$=0, at two values of the boundary parameter, η. Although this behaviour is still weakly dependent on η, it is clear that E^* is tending to a limit as $\eta \to 0$.

We have analysed the extremal configurations and find that as $\eta \to 0$, there is a transition from spatially extended configurations at small p to localised structures at large p. A study of the polar angle at the centre of the system, θ_c, shows that for $p \gtrsim 2.4$, θ_c tends to a finite value in the limit of an infinite system indicating localised solutions. Below $p \simeq 2.4$, the system contains delocalised configurations with θ_c extrapolating to zero as $\eta \to 0$. From this, we identify a transition at p^*=2.4, consistent with that found for the ferromagnet[228]. The energy of delocalised states below p^* can be understood within a linearized continuum theory[228], which gives:

$$E_{\rm SW} = \frac{p^2}{2} + \pi^2 \eta \tag{5.12}$$

corresponding to a system of length L filled with N_2 free, non-interacting spin waves[1]. Numerically, we find that E^* approaches this form as $\eta \to 0$, and the particle densities in each component match those for free spin waves.

Above p^*, the spatially localised configurations form the branch of uniformly propagating solitary waves. Typical spin configurations and particle densities in component 2 are shown in Fig. 5.3 (a) & (b) for intermediate and high p respectively. At intermediate momentum, the structure resembles free spin-waves with a finite spatial extent and so is referred to as a "spin-wave droplet"[228]. Solutions of this type were first found for the 2D two-component BEC at large negative anisotropy in Ref. [232], where they were called "bubbles".

At high momentum, the local spin configuration matches that for a skyrmion-antiskyrmion pair[2]. From Eq. 5.9, the scaled momentum, p, is related to the separation of a skyrmion-antiskyrmion pair, r, by $p = 2r\pi\sqrt{\rho_0/N_2}$. For wide separations (*i.e.* large momenta), the dominant contribution to the energy, E^*, is from the kinetic energy of the superfluid flow. The properties of this regime therefore differ from those of the ferromagnet previously studied[228]. Outside the core regions of size r_0 (wherein $\vec{\ell}$ describes a skyrmion or anti-skyrmion), the superfluid flow is that of a vortex-antivortex pair. The scaled energy, E^*, then includes the term $2\pi \ln(r/r_0)$[231]. The energy dispersion curve at high p approaches this result continuously as $\eta \to 0$ and the velocity, v, of the skyrmion-antiskyrmion pair (Eq. 5.11) tends to $v = \hbar/Mr$.

5.2.2 Dynamical Properties in the Presence of Anisotropy

We have investigated how the anisotropy, $\tilde{c}_2$, affects these results. Figure 5.4 shows the minimum energy as a function of p for $\tilde{c}_2 = -2.0$, 0.0 and 2.0, calculated with respect to $\chi = \chi_\infty$. Negative values of $\tilde{c}_2$ represent an "easy-axis" anisotropy, preferring spatial separation of the components. The ground state is one in which all atoms are in a single component, and the extremal configurations correspond

[1] The momentum of a single free spin wave is P/N_2. Therefore N_2 free spin waves have energy $P^2/2MN_2$ or $p^2/2$ in units of $\hbar^2\rho_0/M$. The term, $\pi^2\eta$, is the finite size energy offset for a system of length L. In the linearised continuum theory, we derive these results by expanding Eq. 5.2 around the ground-state.

[2] These configurations are also the 2D analogues of 3D vortex rings in spinor BECs[54, 233].

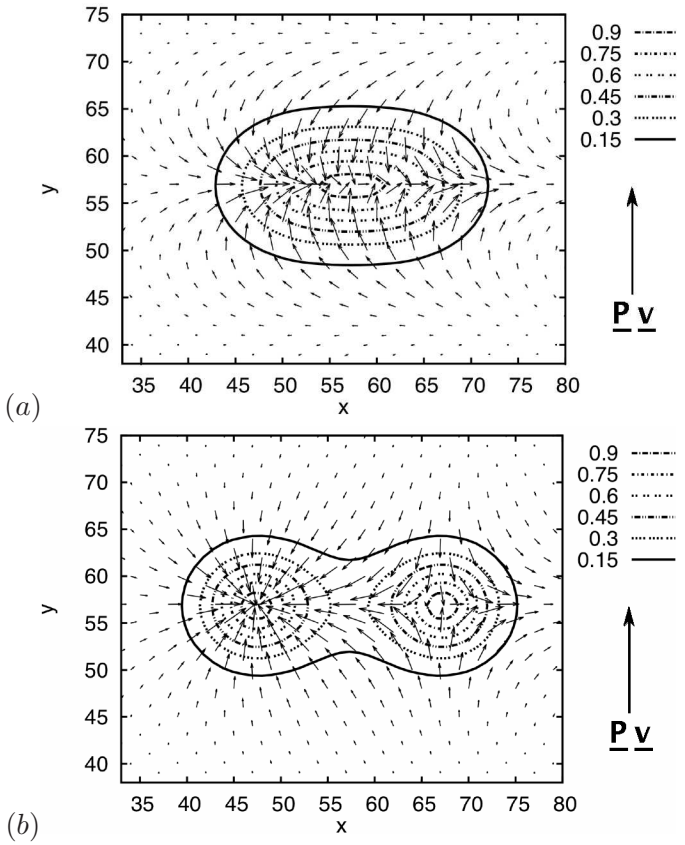

Figure 5.3: The local spin vector $\vec{\ell}(\boldsymbol{r})$ projected onto the xy plane, and contours of the typical particle density in component 2, for η=0.015 and (a) p=4.0 and (b) p=8.5. For clarity, one spin in five is plotted. The direction of the velocity, $\boldsymbol{v}$, and momentum, $\boldsymbol{P}$, of the solitary wave is indicated.

to those discussed above. As the anisotropy is decreased below zero, the critical scaled momentum, p^*, shifts down, until below a critical value, $\tilde{c}_2^*$, the solitary waves exist for all values of momentum[3]. We apply the radially symmetric ansatz of Ref. [228] for the spin-wave droplet state just above the transition. We then find that $p^* = \sqrt{5.8 + 4\tilde{c}_2}$ from the solution of a 1D nonlinear equation[234]. Hence, the transition point, p^*, vanishes below a critical anisotropy, $\tilde{c}_2^* \simeq -1.5$, which is consistent with our numerical results.

A positive $\tilde{c}_2$ represents an "easy-plane" anisotropy, preferring component mixing. The ground state will be an equal mixture of both components. Solitary waves with these boundary conditions were studied in Ref. [235]. However, even for positive $\tilde{c}_2$, skyrmions can be created and can be dynamically stable: starting from a

[3]Solitary waves below this critical value were first discussed in Ref. [232].

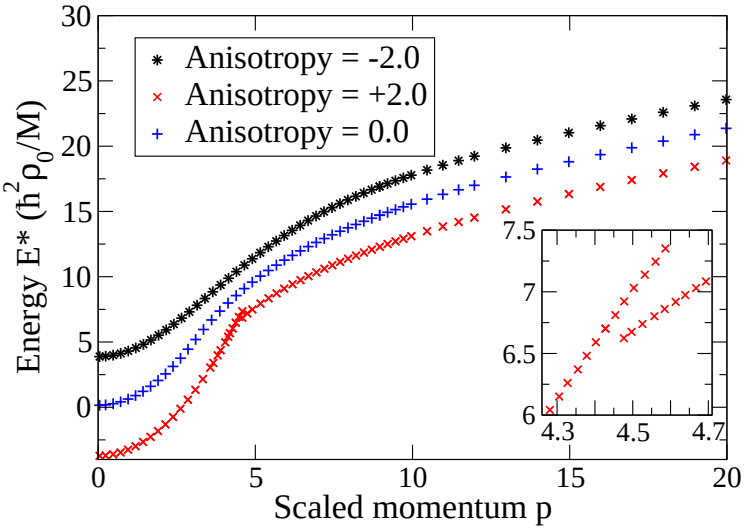

Figure 5.4: The energy dispersion of a two-component condensate for $\tilde{c}_2 = -2.0$, 0.0 and 2.0 for η =0.015. Energy is measured relative to the uniform system $\chi = \chi_\infty$. The value $\tilde{c}_2 = -2.0$ is below $\tilde{c}_2^* = -1.5$, and so solitary waves exist at all momenta, p, for $\eta \to 0$. Inset: Enlargement of the bifurcation region for $\tilde{c}_2 = 2.0$, within which we find two branches of excitations for the same momenta.

single component BEC, such as $\chi = \chi_\infty \equiv (1, 0)$ (with $N_2 = 0$), excitation into a state with non-zero N_2 and P can lead to a solitary wave which cannot relax to the ground state due to the conservation laws. This situation is relevant experimentally as a skyrmion-antiskyrmion pair may be imprinted by selectively exciting atoms from a single component[57]. The energy dispersion curve for these solitary waves is shown in Fig. 5.4. We find that a positive value of $\tilde{c}_2$ increases the critical scaled momentum, p^*. Furthermore, it introduces a bifurcation region, where two excitation branches exist for the same momenta. From our numerical results, we find that excitations in the higher momentum branch always have the form of the skyrmion-antiskyrmion pair described above.

5.3 Experimental Considerations

Recent experimental advances[51, 57, 61] should allow the imprinting of a skyrmion-antiskyrmion pair on a quasi-2D multicomponent BEC and the study of the interesting dynamical properties we predict. Using holographic beams, the separation of the imprinted pair and hence the momentum may be varied, permitting the dynamics of these topological solitons to be investigated with high spatial and temporal resolution.

The anisotropy, $\tilde{c}_2$, controls the position of the cross-over and the type of extremal configuration. For the $|1,-1\rangle$ and $|2,1\rangle$ states of ^{87}Rb, the scattering lengths are: $a_{22} = 95.00a_0$, $a_{11} = 100.40a_0$ and $a_{12} = 97.66a_0$ where a_0 is the Bohr radius[236], giving a small positive value of c_2. For a density of $\rho_{3\mathrm{D}} \simeq 10^{14}\mathrm{cm}^{-3}$, the anisotropy healing length is $\xi_2 \simeq 30\mu$m. Anisotropy is important ($\tilde{c}_2 \gtrsim 1$) only for excitations with $\mathcal{L} \gtrsim \xi_2$, where $\mathcal{L}$ is the scale over which the density of component 2 varies. Recent experiments have demonstrated a spatial resolution on scales as small as 0.5μm[61], and so would allow an exploration of regimes of both weak and strong $\tilde{c}_2$ (for $\mathcal{L} \lesssim 30\mu$m and $\mathcal{L} \gtrsim 30\mu$m respectively)[4].

The solitary waves travel through the system with a uniform velocity, v, while the local spin precesses around ℓ_z with angular frequency, ω. For an excitation with size $\mathcal{L} \simeq 3\mu$m at $p = 8$ for ^{87}Rb, our results typically show that $v \simeq 0.2\mathrm{mm\ s}^{-1}$ and $\omega \simeq 0.3\mathrm{rad\ ms}^{-1}$ (Eq.5.11). Thus, the temporal resolution required to resolve ω is $\simeq 20$ms and it will take $\simeq 50$ms to move a distance of 10μm, both of which are within current experimental capabilities[63].

The creation and characterisation of the solitary waves predicted here will allow subsequent experimental studies of their scattering properties. It would be especially interesting to investigate the general prediction coming from high energy physics, that pairs of (related) 2D solitary waves of equal and opposite momenta should scatter at right angles after colliding head-on[237, 232, 238].

[4]To neglect total density variations, imprinted excitations should be larger than the healing length, $\xi_0 \simeq (\hbar^2/2c_0\rho_{3\mathrm{D}}Ma_z)^{1/2} \simeq 400$nm for ^{87}Rb

5.4 Conclusion

We have explored theoretically the dynamical properties of two-component Bose-Einstein condensates in two dimensions, which can support excitations with the topology of skyrmions. We have investigated a branch of uniformly propagating solitary waves which, at high momentum, can be viewed as skyrmion-antiskyrmion pairs. We have studied these excitations for all interaction regimes and found that above a critical interaction anisotropy, $\tilde{c}_2^*$, there is always a transition to delocalised states at low momentum. We have also discussed how the dynamics of these solitary waves could be accessed with current experimental capabilities and techniques.

Chapter 6

Conclusions

Summary

In this thesis, we have explored some of the fascinating consequences of topology for ultracold atomic gases. We have focused on two key areas of current experimental research: topological energy bands and topological solitons. We have shown that these phenomena have novel features in ultracold gases and proposed how these features might be investigated in experiments. We have also discussed how ultracold gases present the ideal opportunity to probe some properties which are inaccessible in other physical systems.

Our research has been motivated by the direction of current experiments. Energy bands with nontrivial geometrical and topological properties play an important role in artificial gauge fields and optical lattices with more than one site per unit cell. Such bands have long been of interest in the solid-state, where they underlie remarkable phenomena such as the quantum Hall effect. However, ultracold gas experiments require innovative tools to probe these properties, as transport measurements, standard in the solid-state, are hard to achieve. Therefore, in Chapter 3, we have proposed a general method for mapping the Berry curvature from the semiclassical dynamics of a wave packet. We have outlined a "time-reversal" protocol that would allow the Berry curvature to measured over the Brillouin zone for the first time. We have demonstrated this method for several example experimental systems and shown that these measurements would be within current capabilities. Since the publication of this work, a related method has been successfully used to

measure a geometrical phase for the first time in an ultracold atomic gas.

Furthermore, we have shown, in Chapter 4, that the geometrical properties of energy bands can crucially modify the collective mode frequencies of an ultracold gas. Collective modes are an important experimental probe of a system, as they can be measured with high precision. We have demonstrated in this thesis that collective modes may be used characterise the geometrical properties of BECs in topological energy bands. We have determined how the Berry curvature changes the hydrodynamic equations of motion for a trapped Bose-Einstein condensate, shifting oscillation frequencies and splitting otherwise degenerate modes. Using an operator approach, we have derived the effects of Berry curvature on the dipole mode in very general settings. We have also shown that these effects can be large in experiments and so should be readily detected.

In the final chapter of this thesis we have studied the dynamical properties of a two-component 2D Bose-Einstein condensate, which supports excitations with the topology of skyrmions. Skyrmions are topological solitons with applications in many areas of physics. Here, we have identified a branch of uniformly propagating solitary waves, which, at high momentum, can be viewed as skyrmion-antiskyrmion pairs. We have investigated the key features of this branch, and shown that, for experimentally relevant cases, there can be a transition to spatially extended spin wave states at low momentum. These dynamical properties could soon be investigated in experiment as skyrmion-antiskyrmion pairs can be imprinted on BECs and ultracold gases can be studied with high temporal and spatial resolution.

Outlook

There are many interesting open questions still to be explored, both in the wider field and in extensions to this thesis. It would be useful, for example, to ask how we could extend our proposal to map the *non-Abelian* Berry curvature over the Brillouin zone using semiclassical dynamics. This would allow experiments to reconstruct the invariants associated with topological insulators[5, 6, 239], which are another hot topic of current research. We might also consider whether we can combine the two types of topological phenomena discussed in this thesis, and study the effects

of Berry curvature on the behaviour of solitons. When we discussed semiclassical dynamics in Section 3, we neglected the effects of non-linear interactions. However, around the band maximum, where the effective mass is negative, a wavepacket can decay into discrete solitons, as is known without Berry curvature[175, 176, 41]. How would this behaviour be modified if we include a nonzero Berry curvature?

It would also be interesting to expand our work on collective modes. One open question from this thesis is how to obtain the dipole mode splitting using the sum rule method (Section 4.4). This requires an improved ansatz for the interacting wave function. Understanding how to go further with this approach would develop our physical insight into the effects of Berry curvature for a BEC with 2D Rashba spin-orbit coupling.

We could also take our research in new directions and ask, for example, what happens if there are degenerate minima with Berry curvature in the energy dispersion. This would be directly relevant to 2D Rashba spin-orbit coupling with a sufficiently small Zeeman field, where the minima form a degenerate ring at finite momenta and exotic Bose-condensed states are expected[123]. How would this affect the collective modes? Another interesting direction would be to ask what are the lowest-order corrections to the collective mode frequencies when we include beyond mean-field interactions. Without Berry curvature, beyond mean-field effects have been probed in high precision collective mode experiments[188], and so this could be a question of practical interest.

In the wider field, many of the immediate challenges are being faced by experimentalists. It will be a great achievement to reach the strongly correlated regime with artificial magnetic fields, to explore the exotic phenomena associated with 2D SO coupling and to investigate the dynamical properties of topological excitations. While there are various exciting theoretical proposals to reach these goals, it remains to be seen which can be implemented successfully in practice. These experiments will then drive fresh lines of inquiry and probe novel physical phenomena. We hope that new tools, such as those discussed in this thesis, will help to further this endeavour.

Theoretically too there are many interesting avenues of research to be pursued. To give a few examples, one important direction is the realisation of exotic topologi-

cal phases of matter, such as topological insulators, in schemes proposed for ultracold atomic gases. Another area of interest is the creation of artificial dynamical gauge fields, where the field evolves in time through a coupling to the condensate[65]. This may open up opportunities for simulating lattice gauge theories and interesting phenomena more familiar from high energy physics. A third possible avenue of research is to consider topological systems out-of-equilbrium and to ask if any interesting effects are possible when adiabaticity is broken.

Topology will therefore continue to be an fascinating area of research in ultracold atomic gases. There are interesting natural extensions to the work in this thesis, and there are important questions in the wider field for both experiment and theory.

Appendices

Appendix A

Hamiltonian for the Two-Photon Optical Flux Lattice for $F = 1/2$

The Hamiltonian acts in the $g_\pm$ manifold, with the form of (3.16). The optical potential, $\hat{V}(\mathbf{r})$, is characterised by the Rabi frequencies κ_m, $m = 0, \pm 1$, where $m\hbar$ is the angular momentum along z gained by the atom when it absorbs a photon [107].

The potential is formed from laser beams at two frequencies: ω_L and $\omega_L + \delta$ where δ is the Zeeman splitting of the ground states. The laser beams at ω_L are linearly polarised and travelling in the xy plane, while the laser at $\omega_L + \delta$ gives a plane wave propagating along the z axis with σ_z polarisation. The resulting potential takes the form:

$$\hat{V} = \frac{\hbar\kappa_{tot}^2}{3\Delta}\hat{1} + \frac{\hbar}{3\Delta}\begin{pmatrix} |\kappa_-|^2 - |\kappa_+|^2 & E\kappa_0 \\ E\kappa_0^* & |\kappa_+|^2 - |\kappa_-|^2 \end{pmatrix} \tag{A.1}$$

where $\kappa_{tot}^2 = \sum_m |\kappa_m|^2$, $\Delta = \omega_L - \omega_A$, with ω_A as the atomic resonance frequency and it is assumed that $|\Delta| \gg |\delta|, |\kappa_m|$. The field of the laser at frequency $\omega_L + \delta$ is characterised by E, which serves as a uniform, adjustable coupling.

The laser field at frequency ω_L is formed from the superposition of three travelling plane waves of equal intensity and wavevectors $\mathbf{k}_i$ in the xy plane. The set-up discussed in Ref. [107] has triangular symmetry, with an angle of $2\pi/3$ between the beams. The wavevectors are then $\mathbf{k}_1 = -k/2(\sqrt{3}, 1, 0)$, $\mathbf{k}_2 = k/2(\sqrt{3}, -1, 0)$ and

$\mathbf{k}_3 = k(0, 1, 0)$. Up to a scale factor and rotation, this is the same geometry as the asymmetric hexagonal lattice in Section 3.3.1.

Each beam is linearly polarised at an angle θ to the z-axis, giving

$$\kappa = \kappa \sum_{i=1}^{3} e^{i\mathbf{k}_i \cdot \mathbf{r}} [\cos\theta \hat{\mathbf{z}} + \sin\theta (\hat{\mathbf{z}} \times \hat{\mathbf{k}_i})], \tag{A.2}$$

where κ is the Rabi frequency of a single beam. The relative strength of the laser fields at frequencies ω_L and $\omega_L + \delta$ will henceforth be denoted as $\epsilon = E/\kappa$. The overall strength of the potential is $V = \hbar^2\kappa^2/3\Delta$.

To define the unit cell, we consider a unitary transformation: $\hat{U} \equiv \exp(-i\mathbf{k}_3 \cdot \mathbf{r}\hat{\sigma}_z/2)$. This gauge transformation is state dependent and leads to the Hamiltonian in Eqn. 3.20, where $\hat{V}' = \hat{U}^\dagger \hat{V} \hat{U}$ has the same form as $\hat{V}$, with κ_0 replaced by $\kappa_0' = e^{-i\mathbf{k}_3 \cdot \mathbf{r}} \kappa_0$. The coupling then only includes the momentum transfers $\mathbf{K}_{1,2} \equiv \mathbf{k}_{1,2} - \mathbf{k}_3$. These define the reciprocal lattice vectors of the largest possible Brillouin zone, and the smallest possible real space unit cell. This unit cell is that of the hexagonal lattice discussed in Section 3.3.1.

Appendix B

Collective Modes in a Trapped Gas from Hydrodynamics

In a spherically symmetric trap, $V(\boldsymbol{r}) = \frac{1}{2}\kappa|\boldsymbol{r}|^2$, and general modes have the form: $\delta\rho = D(r)Y_{lm}(\theta,\varphi)e^{-i\omega t}$ where $Y_{lm}(\theta,\varphi)$ is a spherical harmonic[209]. To find the mode frequencies, we solve Eq. 4.5:

$$\delta\ddot{\rho} = -\frac{\boldsymbol{\nabla}V\cdot\boldsymbol{\nabla}\delta\rho}{M^*} + \frac{\rho g\boldsymbol{\nabla}^2\delta\rho}{M^*} + \frac{\boldsymbol{\nabla}V\cdot(\boldsymbol{\nabla}\delta\dot{\rho}\times\hat{\boldsymbol{z}})\Omega}{\hbar}. \tag{B.1}$$

Following Ref. [8], we define a new radial function $G(r) = D(r)/r^l$. This leads to a differential equation for the radial function:

$$\omega^2 G(r) = \frac{\kappa}{M^*}\left[lG(r) + rG'(r) - \frac{1}{2}(R^2 - r^2)\left[G''(r) + \frac{2(l+1)G'(r)}{r}\right]\right] - \frac{m\kappa\omega\Omega}{\hbar}G(r),$$

where we have introduced $R^2 = 2\mu/\kappa$, and where a prime is used to denote a spatial derivative. To solve, we change variables to $u = r^2/R^2$[8]. The differential equation becomes:

$$\begin{aligned} u(1-u)G''(u) \quad + \quad & \left[l + \frac{3}{2} - \left(l + \frac{5}{2}\right)u\right]G'(u) \\ & + \frac{1}{2}\left(\frac{M^*}{\kappa}\omega^2 - l + \frac{M^* m\omega\Omega}{\hbar}\right)G(u) = 0. \end{aligned} \tag{B.2}$$

This can be identified[8] as the equation for the hypergeometric function $F(\alpha, \beta; \Gamma; u)$:

$$u(1-u)F''(u) + [\Gamma - (\alpha + \beta + 1)u]\, F'(u) - \alpha\beta F(u) = 0. \tag{B.3}$$

To ensure that the function is well-behaved, either α or β must be a negative integer, $-n_r$. By convention, we choose $\alpha = -n_r$[8]. Comparing Eq. B.2 and Eq. B.3, we can read off: $\beta = l + n_r + 3/2$, $\Gamma = l + 3/2$ and:

$$\frac{1}{2}\left(\frac{M^*}{\kappa}\omega^2 - l + \frac{M^* m\omega\Omega}{\hbar}\right) = -\alpha\beta = n_r(l + n_r + 3/2). \tag{B.4}$$

Rearranging for the frequency, we find:

$$\begin{aligned} \omega^2 &= \frac{\kappa}{M^*}(l + 3n_r + 2n_r l + 2n_r^2) - \frac{\kappa\omega\Omega}{\hbar} \\ \omega &= -\frac{m\kappa\Omega}{2\hbar} + \frac{1}{2}\sqrt{\left(\frac{m\kappa\Omega}{\hbar}\right)^2 + \frac{4\kappa}{M^*}(l + 3n_r + 2n_r l + 2n_r^2)} \end{aligned} \tag{B.5}$$

for the general modes:

$$\delta\rho = Cr^l F(-n_r, l + n_r + 3/2; l + 3/2, r^2/R^2) Y_{lj}(\theta, \varphi) e^{-i\omega t} \tag{B.6}$$

where C is an arbitrary constant and we have chosen the positive energy root of the spectrum by convention. When $\Omega = 0$, we recover the expected mode energies[209].

Appendix C

Hydrodynamics for a General Polytropic Equation of State

C.1 The Velocity Equation

The velocity equation was first derived for a normal gas without Berry curvature in Ref. [211]. In the following derivation, we are also guided by the presentation of Ref. [8]. For reference, we begin by repeating Equation 4.4:

$$\begin{aligned}\dot{\rho} + \boldsymbol{\nabla} \cdot (\rho \boldsymbol{v}) &= 0 \\ \dot{\boldsymbol{v}} &= \frac{\boldsymbol{F}}{M^*} - \left(\frac{\dot{\boldsymbol{F}}}{\hbar} \times \hat{\boldsymbol{z}}\right) \Omega.\end{aligned}$$

In general, the local force per particle is:

$$\begin{aligned}\boldsymbol{F} &= -\frac{1}{\rho}\boldsymbol{\nabla} P - \boldsymbol{\nabla} V \\ \frac{\partial \boldsymbol{F}}{\partial t} &= -\frac{1}{\rho}\boldsymbol{\nabla}\frac{\partial P}{\partial t} + \frac{1}{\rho^2}\frac{\partial \rho}{\partial t}\boldsymbol{\nabla} P.\end{aligned} \tag{C.1}$$

We substitute this into the Euler equation and linearize with respect to the density and pressure, $\rho = \rho_0 + \delta\rho$ and $P = P_0 + \delta P$:

$$\rho_0 \frac{\partial \boldsymbol{v}}{\partial t} = -\frac{\boldsymbol{\nabla}\delta P}{M^*} - \frac{\delta\rho}{M^*}\boldsymbol{\nabla} V + \left(\frac{1}{\hbar}\boldsymbol{\nabla}\frac{\partial \delta P}{\partial t} \times \hat{\boldsymbol{z}}\right)\Omega - \left(\frac{1}{\rho_0}\frac{\partial \delta\rho}{\partial t}\frac{\boldsymbol{\nabla} P_0}{\hbar} \times \hat{\boldsymbol{z}}\right)\Omega. \tag{C.2}$$

This is the linearized form of the conservation of momentum. In equilibrium, the local force is zero and so $\boldsymbol{\nabla} P_0 = -\rho_0 \boldsymbol{\nabla} V$[8]. Substituting this in we find:

$$\rho_0 \frac{\partial \boldsymbol{v}}{\partial t} = -\frac{\boldsymbol{\nabla}\delta P}{M^*} - \frac{\delta\rho}{M^*}\boldsymbol{\nabla} V + \left(\frac{1}{\hbar}\boldsymbol{\nabla}\frac{\partial \delta P}{\partial t} \times \hat{\boldsymbol{z}}\right)\Omega + \left(\frac{\partial \delta\rho}{\partial t}\frac{\boldsymbol{\nabla} V}{\hbar} \times \hat{\boldsymbol{z}}\right)\Omega. \qquad \text{(C.3)}$$

Taking another time derivative gives:

$$\rho_0 \frac{\partial^2 \boldsymbol{v}}{\partial t^2} = -\frac{1}{M^*}\boldsymbol{\nabla}\frac{\partial \delta P}{\partial t} - \frac{\partial \delta\rho}{\partial t}\frac{\boldsymbol{\nabla} V}{M^*} + \left(\frac{1}{\hbar}\boldsymbol{\nabla}\frac{\partial^2 \delta P}{\partial t^2} \times \hat{\boldsymbol{z}}\right)\Omega + \left(\frac{\partial^2 \delta\rho}{\partial t^2}\frac{\boldsymbol{\nabla} V}{\hbar} \times \hat{\boldsymbol{z}}\right)\Omega. \qquad \text{(C.4)}$$

To eliminate the time derivatives of pressure and density, we use the continuity equation, $\frac{\partial \delta\rho}{\partial t} + \boldsymbol{\nabla}\cdot(\rho_0 \boldsymbol{v}) = 0$, as well as:

$$\frac{\partial \delta P}{\partial t} \;=\; -(\gamma+1)P_0 \boldsymbol{\nabla}\cdot\boldsymbol{v} + \rho_0 \boldsymbol{\nabla} V \cdot \boldsymbol{v}, \qquad \text{(C.5)}$$

a statement of the linearised conservation of energy[240, 211, 212, 8]. Substituting into Eq. C.4, we find:

$$\begin{aligned}\rho_0 \frac{\partial^2 \boldsymbol{v}}{\partial t^2} \;=\;& \frac{(\gamma+1)}{M^*}\boldsymbol{\nabla}(P_0 \boldsymbol{\nabla}\cdot\boldsymbol{v}) - \frac{1}{M^*}\boldsymbol{\nabla}(\rho_0 \boldsymbol{\nabla} V\cdot\boldsymbol{v}) + \boldsymbol{\nabla}\cdot(\rho_0\boldsymbol{v})\frac{\boldsymbol{\nabla} V}{M^*} \\ & -\frac{\Omega}{\hbar}\left[(\gamma+1)\boldsymbol{\nabla}\left(P_0\boldsymbol{\nabla}\cdot\frac{\partial \boldsymbol{v}}{\partial t}\right) - \boldsymbol{\nabla}\left(\rho_0\boldsymbol{\nabla} V\cdot\frac{\partial \boldsymbol{v}}{\partial t}\right) + \boldsymbol{\nabla}\cdot\left(\rho_0\frac{\partial \boldsymbol{v}}{\partial t}\right)\right]\times\hat{\boldsymbol{z}}.\end{aligned}$$

To find the final form of the velocity equation, we use that: $(\boldsymbol{\nabla} V\cdot\boldsymbol{v})\boldsymbol{\nabla}\rho_0 = \boldsymbol{\nabla} V(\boldsymbol{v}\cdot\boldsymbol{\nabla})\rho_0$[8]. Then we have:

$$\begin{aligned}\frac{\partial^2 \boldsymbol{v}}{\partial t^2} \;=\;& \frac{(\gamma+1)}{M^*}\frac{P_0}{\rho_0}\boldsymbol{\nabla}(\boldsymbol{\nabla}\cdot\boldsymbol{v}) - \frac{1}{M^*}\boldsymbol{\nabla}(\boldsymbol{\nabla} V\cdot\boldsymbol{v}) - \frac{\gamma}{M^*}\boldsymbol{\nabla} V(\boldsymbol{\nabla}\cdot\boldsymbol{v}) \\ & -\frac{\Omega}{\hbar}\left[(\gamma+1)\frac{P_0}{\rho_0}\boldsymbol{\nabla}\left(\boldsymbol{\nabla}\cdot\frac{\partial \boldsymbol{v}}{\partial t}\right) - \boldsymbol{\nabla}\left(\boldsymbol{\nabla} V\cdot\frac{\partial \boldsymbol{v}}{\partial t}\right) - \gamma\boldsymbol{\nabla} V\left(\boldsymbol{\nabla}\cdot\frac{\partial \boldsymbol{v}}{\partial t}\right)\right]\times\hat{\boldsymbol{z}}. \qquad \text{(C.6)}\end{aligned}$$

This is a vector equation for the velocity field, which can be solved for the collective mode frequencies. (To first calculate the velocity field, we insert our ansatz for the density variation into the continuity equation (Eq. 4.4) and find the corresponding $\boldsymbol{v}$.) As discussed in the main text, modes are separated into three classes. There are incompressible modes ($\boldsymbol{\nabla}\cdot\boldsymbol{v} = 0$), such as the surface modes, which are system-independent. Compressible modes with $\boldsymbol{\nabla}(\boldsymbol{\nabla}\cdot\boldsymbol{v}) = 0$, such as the breathing mode, depend only on γ. And finally, higher energy modes with $n_r > 1$ for $l = 0$ and

$n_r > 0$ for $l > 0$ which depend on both γ and the equilibrium properties of the gas through P_0/ρ_0.

C.2 The Density Equation for Weakly Interacting Bose and Fermi Gases

For a weakly interacting Bose and Fermi gases, the polytropic equation of state describes both the equilibrium properties and linear deviations from equilibrium. Therefore, we can use the equation of state to calculate the local force per particle:

$$\begin{aligned} \boldsymbol{F} &= -\frac{1}{\rho}\boldsymbol{\nabla}P - \boldsymbol{\nabla}V = -\frac{a_p}{\rho}\boldsymbol{\nabla}(\rho^{\gamma+1}) - \boldsymbol{\nabla}V = -\frac{a_p(\gamma+1)}{\gamma}\boldsymbol{\nabla}(\rho^{\gamma}) - \boldsymbol{\nabla}V \\ \frac{\partial \boldsymbol{F}}{\partial t} &= -\frac{a_p(\gamma+1)}{\gamma}\boldsymbol{\nabla}\frac{\partial}{\partial t}(\rho^{\gamma}) \end{aligned} \tag{C.7}$$

where a_p is a dimensional constant (from: $P = a_p\rho^{\gamma+1}$). We substitute this into Eq. 4.4 and linearize to find:

$$\frac{\partial \boldsymbol{v}}{\partial t} = -\frac{a_p(\gamma+1)}{M^*}\boldsymbol{\nabla}(\rho_0^{\gamma-1}\delta\rho) + \frac{a_p(\gamma+1)}{\hbar}\left(\boldsymbol{\nabla}\frac{\partial}{\partial t}(\rho_0^{\gamma-1}\delta\rho)\times\hat{\boldsymbol{z}}\right)\Omega. \tag{C.8}$$

Taking the time derivative of the continuity equation, we can eliminate the velocity to obtain the density equation:

$$\frac{\partial^2\delta\rho}{\partial t^2} + \boldsymbol{\nabla}\cdot\left(\rho_0\left(-\frac{a_p(\gamma+1)}{M^*}\boldsymbol{\nabla}(\rho_0^{\gamma-1}\delta\rho) + \frac{a_p(\gamma+1)}{\hbar}\left(\boldsymbol{\nabla}\frac{\partial}{\partial t}(\rho_0^{\gamma-1}\delta\rho)\times\hat{\boldsymbol{z}}\right)\Omega\right)\right) = 0$$

General Modes in Dilute Quantum Gases

As in Appendix B, we can compute the general modes of a condensed gas from the density equation. This depends on the equilibrium density, ρ_0. For a large enough N, a weakly interacting dilute BEC can be described by the Thomas-Fermi approximation: $\rho_0 = [\mu - V(\boldsymbol{r})]/g$, where we have neglected the kinetic energy. A similar semiclassical treatment can also be applied to fermions, where to a good first approximation, we can assume that they are non-interacting[1]. Then, in the

[1] This is appropriate for a one-component Fermi gas as there is no s-wave scattering between two fermions in the same internal state.

Thomas-Fermi approximation, the local Fermi energy is that of a homogeneous gas, giving the density[8]:

$$\rho_0 = \frac{1}{6\pi^2}\left(\frac{m\kappa}{\hbar^2}[R^2 - r^2]\right)^{3/2}. \tag{C.9}$$

This is valid provided that the Fermi wavelength is small compared to the size of the cloud (i.e. $N^{1/3} \gg 1$)[8]. We write the Thomas-Fermi density for both bosons and fermions in one general equation:

$$\rho_0 = \left(\frac{\gamma}{2(\gamma+1)a_p}\kappa[R^2 - r^2]\right)^{1/\gamma}. \tag{C.10}$$

Using this, the density equation becomes:

$$\begin{aligned}\frac{\partial^2\delta\rho}{\partial t^2} \quad & +\boldsymbol{\nabla}\cdot(-\left(R^2-r^2\right)^{1/\gamma}\frac{\gamma\kappa}{2M^*}\boldsymbol{\nabla}\left(\left(R^2-r^2\right)^{(\gamma-1)/\gamma}\delta\rho\right) \\ & +\left(R^2-r^2\right)^{1/\gamma}\frac{\gamma\kappa\Omega}{2\hbar}\left(\boldsymbol{\nabla}\left(\left(R^2-r^2\right)^{(\gamma-1)/\gamma}\frac{\partial\delta\rho}{\partial t}\right)\times\hat{\boldsymbol{z}}\right)) = 0\end{aligned} \tag{C.11}$$

which reduces to Eq. 4.5 for the Bose gas ($\gamma = 1$). As in Appendix B, we solve this for general modes:

$$\delta\rho \propto r^l G(r) Y_{l,j}(\theta,\varphi)(R^2-r^2)^{(\gamma-1)/\gamma}e^{-i\omega t} \tag{C.12}$$

where the factor of $(R^2 - r^2)^{(\gamma-1)}$ has to be introduced to ensure that the density variation in a Fermi gas vanishes smoothly at the cloud boundary[213]. Otherwise, a large kinetic energy cost is incurred, which cannot be neglected. (This is in contrast to the Bose gas[213]). The derivation of the mode frequencies then follows closely that in Appendix B: we substitute $\delta\rho$ into Eq. C.11 and obtain a differential equation for $G(r)$. After a variable substitution, $u = r^2/R^2$, the radial equation becomes:

$$u(1-u)G''(u) + \left[l + \frac{3}{2} - \left(l + \frac{3}{2} + \frac{1}{\gamma}\right)u\right]G'(u) + \frac{1}{2\gamma}\left[\frac{M^*}{\kappa}\omega^2 - l + \frac{M^* m\omega\Omega}{\hbar}\right]G(u) = 0$$

(c.f. Eq. B.2). The solution is the hypergeometric function, $F(\alpha,\beta;\Gamma;u)$, now with: $\alpha = -n_r$, $\beta = l + n_r + 1/\gamma + 1/2$, $\Gamma = l + 3/2$. Therefore the polytropic index enters

the function only through the parameter β. The frequencies of the modes are:

$$\begin{aligned} \omega^2 &= \frac{\kappa}{M^*}(l+\gamma n_r(2l+2n_r+1)+2n_r) - \frac{\kappa\omega\Omega}{\hbar} \\ \omega &= -\frac{m\kappa\Omega}{2\hbar} + \frac{1}{2}\sqrt{\left(\frac{m\kappa\Omega}{\hbar}\right)^2 + \frac{4\kappa}{M^*}(l+\gamma n_r(2l+2n_r+1)+2n_r)} \end{aligned} \quad \text{(C.13)}$$

Again this reduces to Eq. 4.6 as required $\gamma = 1$. This shows that for dilute condensates, the effect of Berry curvature is independent of the polytropic index. The mode frequencies shift and split regardless of the statistics of the gas.

Appendix D

A Sum Rule Method for the 2D Rashba Dipole Mode

We derive the frequency of the dipole mode in the 2D Rashba model (Eq. 4.10) using a sum rule approach. We are guided by Ref. [215] which considers the simpler case of 1D SO-coupling. As our aim is to find an expression for:

$$\hbar\omega_{\pm 1} \leq \sqrt{\frac{m_{-1}(\hat{D}_{\pm 1})}{m_{-3}(\hat{D}_{\pm 1})}}, \tag{D.1}$$

we begin with the inverse energy weighted moment:

$$\begin{aligned}
m_{-1}(\hat{D}_{\pm 1}) &= \sum_n \frac{|\langle 0|\hat{D}_{\pm 1}|n\rangle|^2}{E_n - E_0} \\
&= -\sum_n \frac{i}{2\omega_0^2 \hbar M} \frac{[\langle 0|\hat{D}_{\pm 1}|n\rangle\langle n|[\hat{H}, \hat{P}_x \pm i\hat{P}_y]|0\rangle + \langle 0|[\hat{H}, \hat{P}_x \mp i\hat{P}_y]|n\rangle\langle n|\hat{D}^\dagger_{\pm 1}|0\rangle]}{E_n - E_0} \\
&= -\sum_n \frac{i}{2\omega_0^2 \hbar M} \frac{(E_n - E_0)[\langle 0|\hat{D}_{\pm 1}|n\rangle\langle n|\hat{P}_x \pm i\hat{P}_y|0\rangle - \langle 0|\hat{P}_x \mp i\hat{P}_y]n\rangle\langle n|\hat{D}^\dagger_{\pm 1}|0\rangle]}{E_n - E_0} \\
&= -\frac{i}{2\omega_0^2 \hbar M}\langle 0|[\hat{X}, \hat{P}_x] + [\hat{Y}, \hat{P}_y] \pm i2\hat{X}\hat{P}_y \mp i2\hat{Y}\hat{P}_x|0\rangle \\
&= \frac{N}{\omega_0^2 M} - \frac{1}{\omega_0^2 \hbar M}\langle 0| \mp \hat{X}\hat{P}_y \pm \hat{Y}\hat{P}_x|0\rangle = \frac{N}{\omega_0^2 M} \pm \frac{1}{\omega_0^2 \hbar M}\langle 0|\hat{L}_z|0\rangle
\end{aligned} \tag{D.2}$$

where we have the closure relation $\sum_n |n\rangle\langle n| = 1$, as well as the commutation relations:

$$[\hat{H}, \hat{P}_x] = i\omega_0^2 \hbar M \hat{X}, \qquad [\hat{H}, \hat{P}_y] = i\omega_0^2 \hbar M \hat{Y}. \tag{D.3}$$

Note, the second term in Eq. D.2 has no analogue in 1D spin-orbit coupling[215]. It arises naturally because the 2D dipole operator is not Hermitian (unlike the operator in 1D). Now we turn to the inverse cubic energy weighted moment:

$$\begin{aligned} m_{-3}(\hat{D}_{\pm 1}) &= \sum_n \frac{|\langle 0|\hat{D}_{\pm 1}|n\rangle|^2}{(E_n - E_0)^3} = \sum_n \frac{1}{\omega_0^4 \hbar^2 M^2} \frac{|\langle 0|[\hat{H}, \hat{P}_x \mp i\hat{P}_y]|n\rangle|^2}{(E_n - E_0)^3} \\ &= \frac{1}{\omega_0^4 \hbar^2 M^2} \sum_n \frac{|\langle 0|\hat{P}_x \mp i\hat{P}_y|n\rangle|^2}{(E_n - E_0)} \left(= \frac{m_{-1}(\hat{P}_x \mp i\hat{P}_y)}{\omega_0^4 \hbar^2 M^2} \right). \end{aligned}$$

Here we shall use that:

$$(\hat{P}_x \mp i\hat{P}_y) = \frac{iM}{\hbar}[\hat{H}, \hat{D}_{\pm 1})] + M\lambda_R(\mp i\hat{\Sigma}_x - \hat{\Sigma}_y). \tag{D.4}$$

Substituting this in, we find:

$$\begin{aligned} m_{-3}(\hat{D}_{\pm 1}) &= \frac{i}{2\omega_0^4 \hbar^3 M} \sum_n [\langle 0|\hat{P}_x \mp i\hat{P}_y|n\rangle\langle n|\hat{D}^\dagger_{\pm 1}|0\rangle - \langle 0|\hat{D}_{\pm 1}|n\rangle\langle n|(\hat{P}_x \pm i\hat{P}_y)|0\rangle] \\ &+ \frac{1}{2\omega_0^4 \hbar^2 M^2} \sum_n \frac{\langle 0|\hat{P}_x \mp i\hat{P}_y|n\rangle\langle n|M\lambda_R(\pm i\hat{\Sigma}_x - \hat{\Sigma}_y)|0\rangle}{E_n - E_0} \\ &+ \frac{1}{2\omega_0^4 \hbar^2 M^2} \sum_n \frac{\langle 0|M\lambda_R(\mp i\hat{\Sigma}_x - \hat{\Sigma}_y)|n\rangle\langle n|\hat{P}_x \pm i\hat{P}_y|0\rangle}{E_n - E_0} \end{aligned}$$

Substituting once again for $(\hat{P}_x \mp i\hat{P}_y)$ and using $\sum_n |n\rangle\langle n| = 1$, we have:

$$\begin{aligned} m_{-3}(\hat{D}_{\pm 1}) &= \frac{i}{2\omega_0^4 \hbar^3 M} [\langle 0|(\hat{P}_x \mp i\hat{P}_y)\hat{D}^\dagger_{\pm 1}|0\rangle - \langle 0|\hat{D}_{\pm 1}(\hat{P}_x \pm i\hat{P}_y)|0\rangle] \\ &+ \frac{1}{2\omega_0^4 \hbar^2 M^2} \sum_n \frac{\langle 0|\frac{iM}{\hbar}[\hat{H}, \hat{D}_{\pm 1}]|n\rangle\langle n|M\lambda_R(\pm i\hat{\Sigma}_x - \hat{\Sigma}_y)|0\rangle}{E_n - E_0} + \frac{\lambda_R^2}{\omega_0^4 \hbar^2} \sum_n \frac{|\langle 0|(\mp i\hat{\Sigma}_x - \hat{\Sigma}_y)|n\rangle|^2}{E_n - E_0} \\ &+ \frac{1}{2\omega_0^4 \hbar^2 M^2} \sum_n \frac{\langle 0|M\lambda_R(\mp i\hat{\Sigma}_x - \hat{\Sigma}_y)|n\rangle\langle n|\frac{iM}{\hbar}[\hat{H}, \hat{D}^\dagger_{\pm 1}]|0\rangle}{E_n - E_0}. \end{aligned} \tag{D.5}$$

We expand and simplify to find:

$$\begin{aligned} m_{-3}(\hat{D}_{\pm 1}) &= \frac{N}{M\hbar^2\omega_0^4} \pm \frac{1}{M\hbar^3\omega_0^4}\langle 0|\hat{L}_z|0\rangle \pm \frac{\lambda_R}{\hbar^3\omega_0^4}\langle 0|(\hat{X} + i\hat{Y})\hat{\Sigma}_- + \hat{\Sigma}_+(\hat{X} - i\hat{Y})|0\rangle \\ &+ \sum_n \frac{4\lambda_R^2}{\hbar^2\omega_0^4(E_n - E_0)} |\langle 0|\hat{\Sigma}_\mp|n\rangle|^2 \end{aligned} \tag{D.6}$$

Appendix E

Applying the Sum Rule Approach for 2D Rashba Dipole Mode to an Ansatz

Choice of Ansatz

We begin with the interacting Gross-Pitaevskii equations (Section 1.2.2):

$$\begin{aligned}\frac{\boldsymbol{p}^2}{2M}\psi_1 - \Delta\psi_1 - \lambda_R(ip_x + p_y)\psi_2 + V(x,y)\psi_1 + g(|\psi_1|^2 + |\psi_2|^2)\psi_1 &= \mu\psi_1 \\ \frac{\boldsymbol{p}^2}{2M}\psi_2 + \Delta\psi_2 + \lambda_R(ip_x - p_y)\psi_1 + V(x,y)\psi_2 + g(|\psi_1|^2 + |\psi_2|^2)\psi_2 &= \mu\psi_2\end{aligned}$$

where ψ_1 is the component in $|\uparrow\rangle$, ψ_2 is the component in $|\downarrow\rangle$ and we have taken $g_{2D} = g$. Within the Thomas-Fermi approximation, we neglect the kinetic energy terms compared to the interactions and trapping potential. Then if we assume that to lowest order only ψ_1 is occupied, we find that:

$$|\psi_1| = \sqrt{\frac{\mu + \Delta - V(x,y)}{g}} \tag{E.1}$$

where we can normalise μ so that there are N particles within the Thomas-Fermi volume. In reality, all the atoms are not in $|\uparrow\rangle$, so we relax this constraint to lowest

order:

$$\lambda_R(ip_x - p_y)\psi_1 \simeq \left(\mu - \Delta - V(x,y) - g|\psi_1|^2\right)\psi_2 = -2\Delta\psi_2 \tag{E.2}$$

where we neglect both the kinetic energy and $|\psi_2|^2$. Then we can write:

$$\psi_2 = -\frac{\lambda_R}{2\Delta}(ip_x - p_y)\psi_1 \quad = \quad +\frac{\lambda_R}{4\Delta\sqrt{g}}\frac{M\omega_0^2\hbar}{\sqrt{\mu+\Delta-V(x,y)}}(x+iy) \tag{E.3}$$

The ansatz is therefore:

$$\Psi = \begin{pmatrix} \sqrt{\frac{\mu+\Delta-V(x,y)}{g}} \\ \frac{\lambda_R}{4\Delta\sqrt{g}}\frac{M\omega_0^2\hbar}{\sqrt{\mu+\Delta-V(x,y)}}(x+iy) \end{pmatrix} \tag{E.4}$$

This ansatz has key similarities to the non-interacting states discussed in Section 4.4.2. There too the spin-orbit coupling leads to a ground-state of $|\uparrow\rangle$ atoms with no angular momentum mixed with $|\downarrow\rangle$ atoms with one unit of angular momentum. This suggest that the ansatz has captured some of the important physical features of this system. As calculating the dipole mode frequencies is long and involved, we shall break it up into intermediate steps. For a summary of the results, see Section E.3.

E.1 Inverse Energy Weighted Moment: m_{-1}

We begin with:

$$m_{-1}(\hat{D}_{\pm1}) \quad = \quad \frac{N}{m\omega_0^2} \pm \frac{1}{m\hbar\omega_0^2}\langle 0|\hat{L}_z|0\rangle = \frac{N}{m\omega_0^2} \pm \frac{1}{m\omega_0^2\hbar}\langle 0|\hat{X}\hat{P}_y - \hat{Y}\hat{P}_x|0\rangle \tag{E.5}$$

The second term vanishes when operating on ψ_1 (as expected). However, we can see from the form of the ansatz, that all atoms in ψ_2 have one unit of angular momentum. Then we find:

$$(\hat{X}\hat{P}_y - \hat{Y}\hat{P}_x)\psi_2 = \frac{\lambda_R}{4\Delta\sqrt{g}}\frac{M\omega_0^2\hbar^2}{\sqrt{\mu+\Delta-V(x,y)}}(x+iy)\,, \tag{E.6}$$

and so:

$$\langle 0|\hat{X}\hat{P}_y - \hat{Y}\hat{P}_x|0\rangle \;=\; \frac{\lambda_R^2 M^2\omega_0^4\hbar^3}{16\Delta^2 g}\int \frac{\left(x^2+y^2\right)}{\mu+\Delta-V(x,y)}d^2r = \hbar N_2, \qquad \text{(E.7)}$$

where we have recognised $N_2 \equiv \langle\psi_2|\psi_2\rangle$. Above, we assumed that $N_2 \ll N$ when we neglected the interaction terms due to $|\psi_2|^2$. From this integral, we can estimate that $N_2 \propto \frac{\zeta\chi}{G}N$. As we are interested in the regime of $G \gg 1$, $\chi \lesssim 1$ and $0 < \zeta < 1$, neglecting N_2 seems a reasonable approximation. Therefore:

$$m_{-1}(D_a) = \frac{N}{m\omega_0^2} \pm \frac{N_2}{m\omega_0^2} \simeq \frac{N}{m\omega_0^2} \qquad \text{(E.8)}$$

E.2 Inverse Cubic Energy Weighted Moment: m_{-3}

Let us now consider the other moment:

$$\begin{aligned} m_{-3}(\hat{D}_{\pm 1}) \;=\; & \frac{N}{M\hbar^2\omega_0^4} \pm \frac{1}{M\hbar^3\omega_0^4}\langle 0|\hat{L}_z|0\rangle \pm \frac{\lambda_R}{\hbar^3\omega_0^4}\langle 0|(\hat{X}+i\hat{Y})\hat{\Sigma}_- + \hat{\Sigma}_+(\hat{X}-i\hat{Y})|0\rangle \\ & + \sum_n \frac{4\lambda_R^2}{\hbar^2\omega_0^4(E_n-E_0)}|\langle 0|\hat{\Sigma}_\mp|n\rangle|^2 \end{aligned} \qquad \text{(E.9)}$$

The first two terms have just been considered above, so now we focus on the third and fourth terms.

The Third Term in m_{-3}

The Pauli spin matrix operators in this term couple ψ_1 and ψ_2. Therefore we can write:

$$\begin{aligned} & \int [\psi_2^\dagger(\hat{X}+i\hat{Y})\psi_1 + \psi_1^\dagger(\hat{X}-i\hat{Y})\psi_2]d^2r \\ & = \frac{\lambda_R}{4\Delta g}M\omega_0^2\hbar\int\left[(x-iy)(x+iy)+(x+iy)(x-iy)\right]d^2r \\ & = \frac{\lambda_R}{2\Delta g}M\omega_0^2\hbar\int[x^2+y^2]d^2r = \frac{\lambda_R\pi}{\Delta g}M\omega_0^2\hbar\int_0^R r^3dr = \frac{\lambda_R\pi}{4\Delta g}M\hbar\omega_0^2R^4 \end{aligned} \qquad \text{(E.10)}$$

where R is the radius of the cloud. As we have assumed N_2 is negligible, R is set by the equation for ψ_1 only. From Eq. E.1, this is radius at which ψ_1 drops to zero:

$$R^2 = \frac{2(\mu+\Delta)}{M\omega_0^2} \tag{E.11}$$

We can determine μ, through the normalisation: $N = \int |\psi_1|^2 d^2r$. Then we find:

$$\begin{aligned} N &= \int \frac{\mu+\Delta-\frac{1}{2}M\omega_0^2 r^2}{g} r dr d\theta = \frac{2\pi}{g}\left[\frac{(\mu+\Delta)^2}{M\omega_0^2} - \frac{(\mu+\Delta)^2}{2M\omega_0^2}\right] = \frac{\pi(\mu+\Delta)^2}{gM\omega_0^2} \\ (\mu+\Delta) &= \sqrt{\frac{NgM\omega_0^2}{\pi}} \\ R &= \left(\frac{4Ng}{M\omega_0^2\pi}\right)^{(1/4)} \end{aligned} \tag{E.12}$$

So putting this all together, we find:

$$\pm\frac{\lambda_R}{\hbar^3\omega_0^4}\langle 0|(\hat{X}+i\hat{Y})\hat{\Sigma}_- + \hat{\Sigma}_+(\hat{X}-i\hat{Y})|0\rangle = \pm\frac{\lambda_R^2 N}{\hbar^2\omega_0^4\Delta}. \tag{E.13}$$

Fourth Term in m_{-3}

Finally, we consider:

$$\sum_n \frac{4\lambda_R^2}{\hbar^2\omega_0^2(E_n-E_0)}|\langle 0|\hat{\Sigma}_\mp|n\rangle|^2 = \frac{4\lambda_R^2}{\hbar^2\omega_0^2} m_{-1}(\hat{\Sigma}_\mp). \tag{E.14}$$

As mentioned in the main text, this is related to the static spin polarizability per particle as: $\chi_{\hat{\Sigma}_\pm}(0) = m_{-1}(\hat{\Sigma}_+) + m_{-1}(\hat{\Sigma}_-)$.

Linear Response Theory

We are guided by the standard procedure within linear response theory for calculating static spin polarizabilities. We consider the perturbation of the ground-state wave function under the influence of a weak magnetic field. To find the spin response function, we can then differentiate the expectation value of the spin in the new perturbed ground-state with respect to the magnetic field. Mathematically, the

wave function in first order perturbation theory will become:

$$|0\rangle' \simeq |0\rangle + |\delta\Psi\rangle = |0\rangle + \sum_{n\neq 0} |n\rangle \frac{\langle n| \sum_\alpha h_\alpha \hat{\Sigma}_\alpha |0\rangle}{E_0 - E_n}, \tag{E.15}$$

where the weak perturbing field is $\boldsymbol{h}$. Therefore to lowest order:

$$\delta\langle\hat{\Sigma}_\alpha\rangle \simeq \sum_{n\neq 0} \frac{\langle 0|\hat{\Sigma}_\alpha|n\rangle\langle n| \sum_\beta h_\beta \hat{\Sigma}_\beta|0\rangle}{E_0 - E_n} + \frac{\langle 0| \sum_\beta h_\beta \hat{\Sigma}_\beta|n\rangle\langle n|\hat{\Sigma}_\alpha|0\rangle}{E_0 - E_n}. \tag{E.16}$$

Then we have:

$$\chi_{\alpha\beta} \equiv \left.\frac{\partial\langle\hat{\Sigma}_\alpha\rangle}{\partial h_\beta}\right|_{\boldsymbol{h}\to 0} = \sum_{n\neq 0}\left[\frac{\langle 0|\hat{\Sigma}_\alpha|n\rangle\langle n|\hat{\Sigma}_\beta|0\rangle}{E_0 - E_n} + \frac{\langle 0|\hat{\Sigma}_\beta|n\rangle\langle n|\hat{\Sigma}_\alpha|0\rangle}{E_0 - E_n}\right]. \tag{E.17}$$

Using the above expressions we can re-write the term appearing in m_{-3} as:

$$\begin{aligned}
&\sum_n \frac{4}{(E_n - E_0)}|\langle 0|\hat{\Sigma}_\mp|n\rangle|^2 = m_{-1}(\mp i\hat{\Sigma}_x - \hat{\Sigma}_y) = \sum_{n\neq 0}\frac{|\langle 0| \mp i\hat{\Sigma}_x - \hat{\Sigma}_y|n\rangle|^2}{E_n - E_0} \\
= &\sum_{n\neq 0}\frac{1}{E_n - E_0}[|\langle 0|\hat{\Sigma}_x|n\rangle|^2 + |\langle 0|\hat{\Sigma}_y|n\rangle|^2 \pm i\langle 0|\hat{\Sigma}_x|n\rangle\langle n|\hat{\Sigma}_y|0\rangle \mp i\langle 0|\hat{\Sigma}_y|n\rangle\langle n|\hat{\Sigma}_x|0\rangle] \\
= &-\frac{\chi_{xx}}{2} - \frac{\chi_{yy}}{2} \pm i\frac{\partial}{\partial h_y}[\langle 0|\hat{\Sigma}_x|\delta\Psi\rangle - \langle\delta\Psi|\hat{\Sigma}_x|0\rangle]
\end{aligned} \tag{E.18}$$

We shall therefore calculate these parts in turn.

Variational Perturbed Wavefunction

We would like to calculate $|\delta\psi\rangle$ without knowledge of the higher many-body states $|n\rangle$. We therefore proceed by taking a variational wave-function based on the ground-state. We minimise the energy of this wave-function with the external perturbing magnetic field. To be consistent, we assume that all atoms are in $|\uparrow\rangle$ when we carry out this variational calculation. We then use the interacting Gross-Pitaevskii equations and include the perturbed $\bar{\psi}_2$ to lowest order, to find the complete final perturbed wave function.

In the limit of $\chi \to 0$, where only ψ_1 is occupied, we can write the wave function

variationally as:

$$\Psi \propto \begin{pmatrix} \cos(\theta) \\ -\sin(\theta)e^{i\phi} \end{pmatrix} e^{i\boldsymbol{k}\cdot\boldsymbol{r}}. \tag{E.19}$$

In the ground state, we have $\boldsymbol{k} = 0$ and $\theta = 0$ (ϕ can take any value). To find the effects of a small external field, we expand this variational wave function around these equilibrium values as:

$$\cos(\theta) \to 1 - \frac{(\delta\theta)^2}{2}, \qquad \sin(\theta) \to \delta\theta, \qquad \boldsymbol{k} \to 0 + \delta\boldsymbol{k} \tag{E.20}$$

where we neglect terms above second order. The energy density $\epsilon = \varepsilon/N$, as calculated with respect to our variational wave function, is:

$$\begin{aligned} \epsilon_0 &= \frac{\hbar^2\delta\boldsymbol{k}^2}{2M} + 2\hbar\lambda_R\delta\theta\delta k_y\cos\phi - 2\hbar\lambda_R\delta\theta\delta k_x\sin\phi - \Delta(1-2\delta\theta^2) + \frac{g\rho}{2}(1-2\delta\theta^2) + g\rho\delta\theta^2 \\ &= \frac{\hbar^2\delta\boldsymbol{k}^2}{2M} + 2\hbar\lambda_R\delta\theta\delta k_y\cos\phi - 2\hbar\lambda_R\delta\theta\delta k_x\sin\phi - \Delta(1-2\delta\theta^2) + \frac{g\rho}{2} \end{aligned} \tag{E.21}$$

where again only keep up to second order. The external field, $\boldsymbol{h}$, couples to our system as:

$$\Delta H = \frac{h_x\hat{\Sigma}_x + h_y\hat{\Sigma}_y}{\hbar}, \tag{E.22}$$

giving the energy contribution:

$$\delta\epsilon = -2h_x\delta\theta\cos\phi - 2h_y\delta\theta\sin\phi. \tag{E.23}$$

We minimise the total energy $\epsilon = \epsilon_0 + \delta\epsilon$ with respect to ϕ, $\delta\theta$ and $\delta\boldsymbol{k}$ to find $\tan\phi = \frac{h_y}{h_x}$ and:

$$\delta k_y = -\frac{2\lambda_R m\delta\theta\cos\phi}{\hbar}, \qquad \delta k_x = \frac{2\lambda_R m\delta\theta\sin\phi}{\hbar}, \qquad \delta\theta = \frac{2h_x\cos\phi + 2h_y\sin\phi}{-4\lambda_R^2 m + 4\Delta}.$$

The perturbed wave function, $\bar{\psi}_1$ can therefore be written to first order in the perturbing field:

$$\bar{\psi}_1 \simeq \sqrt{\frac{\mu + \Delta - V(x,y)}{g}}e^{i\delta\boldsymbol{k}\cdot\boldsymbol{r}}. \tag{E.24}$$

To find $\bar{\psi}_2$, we turn to the interacting Gross-Piteavskii equations. In the presence of an external magnetic field, Eq. E.2 becomes:

$$\lambda_R(ip_x - p_y)\tilde{\psi}_1 + (h_x + ih_y)\tilde{\psi}_1 \simeq \left(\mu - \Delta - V(x,y) - g|\tilde{\psi}_1|^2\right)\tilde{\psi}_2 = -2\Delta\tilde{\psi}_2. \quad \text{(E.25)}$$

Rearranging this, we find:

$$\begin{aligned}\tilde{\psi}_2 &= +\frac{\lambda_R}{4\Delta\sqrt{g}}\frac{M\omega_0^2\hbar}{\sqrt{\mu+\Delta-V(x,y)}}(x+iy)\,e^{i\delta\boldsymbol{k}\cdot\boldsymbol{r}} - i\frac{\lambda_R\hbar}{2\Delta}(\delta k_x + i\delta k_y)\sqrt{\frac{\mu+\Delta-V(x,y)}{g}}e^{i\delta\boldsymbol{k}\cdot\boldsymbol{r}} \\ &\quad -\frac{1}{2\Delta}(h_x+ih_y)\sqrt{\frac{\mu+\Delta-V(x,y)}{g}}e^{i\delta\boldsymbol{k}\cdot\boldsymbol{r}} \qquad \text{(E.26)}\end{aligned}$$

Calculating χ_{xx}

Now that we have an expression for the perturbed wave function, we can calculate all the terms in Eq. E.18. We begin with $\chi_{xx} \equiv \frac{\partial\langle\hat{\Sigma}_x\rangle}{\partial h_x}|_{\boldsymbol{h}\to 0}$. Therefore we consider:

$$\begin{aligned}\langle\hat{\Sigma}_x\rangle &= \int(\tilde{\psi}_1^\dagger\tilde{\psi}_2 + \tilde{\psi}_2^\dagger\tilde{\psi}_1)d^2\mathbf{r} \\ &= \int\left[\frac{2\lambda_R}{4\Delta g}M\omega_0^2\hbar r\cos\theta + \frac{\delta k_y\lambda_R\hbar}{\Delta}\frac{\mu+\Delta-\frac{1}{2}M\omega_0^2r^2}{g} - \frac{h_x}{\Delta}\frac{\mu+\Delta-\frac{1}{2}M\omega_0^2r^2}{g}\right]rdrd\theta \\ &= \frac{\delta k_y\lambda_R\hbar}{\Delta}N - \frac{h_x}{\Delta}N\end{aligned}$$

where we have used the normalisation: $N = \int|\psi_1|^2d^2r$. After substituting for δk_y, we find:

$$\langle\Sigma_x\rangle = -\frac{\lambda_R^2MN}{\Delta}\frac{\frac{1}{2}\left[\frac{h_x-\frac{h_y^2}{h_x}}{1+\frac{h_y^2}{h_x^2}}+h_x\right]+\frac{\frac{h_y^2}{h_x}}{1+\frac{h_y^2}{h_x^2}}}{-\lambda_R^2M+\Delta} - \frac{h_x}{\Delta}N. \qquad \text{(E.27)}$$

We differentiate with respect to h_x, and take the limit $\boldsymbol{h}\to 0$ to calculate:

$$\chi_{xx} = -\frac{\lambda_R^2MN}{\Delta}\frac{1}{-\lambda_R^2M+\Delta} - \frac{N}{\Delta} \qquad \text{(E.28)}$$

Calculating: χ_{yy}

Now we repeat the above procedure for $\chi_{yy} \equiv \frac{\partial \langle \hat{\Sigma}_y \rangle}{\partial h_y}|_{\boldsymbol{h}\to 0}$. Then we have:

$$\begin{aligned}
\langle \hat{\Sigma}_y \rangle &= \int (-i\tilde{\psi}_1^\dagger \tilde{\psi}_2 + i\tilde{\psi}_2^\dagger \tilde{\psi}_1) d^2\mathbf{r} \\
&= \int \left[\frac{2\lambda_R}{4\Delta g} M\omega_0^2 \hbar r \sin\theta - \frac{\delta k_x \lambda_R \hbar}{\Delta} \frac{\mu + \Delta - \frac{1}{2}M\omega_0^2 r^2}{g} - \frac{h_y}{\Delta} \frac{\mu + \Delta - \frac{1}{2}M\omega_0^2 r^2}{g} \right] r dr d\theta \\
&= -\frac{\delta k_x \lambda_R \hbar}{\Delta} N - \frac{h_y}{\Delta} N. \qquad \text{(E.29)}
\end{aligned}$$

Again we substitute for δk_x to find:

$$\begin{aligned}
\langle \hat{\Sigma}_y \rangle &= -\frac{\lambda_R^2 M N}{\Delta} \frac{\frac{h_y}{1+\frac{h_y^2}{h_x^2}} + \frac{1}{2}\left[h_y - \frac{h_y - \frac{h_y^3}{h_x^2}}{1+\frac{h_y^2}{h_x^2}} \right]}{-\lambda_R^2 M + \Delta} - \frac{h_y}{\Delta} N \\
\chi_{yy} &= -\frac{\lambda_R^2 M N}{\Delta} \frac{1}{-\lambda_R^2 M + \Delta} - \frac{N}{\Delta} \qquad \text{(E.30)}
\end{aligned}$$

As expected, these results are isotropic i.e. $\chi_{xx} = \chi_{yy}$.

Calculating $\frac{\partial}{\partial h_y}[\langle 0|\hat{\Sigma}_x|\delta\Psi\rangle - \langle \delta\Psi|\hat{\Sigma}_x|0\rangle]$

To lowest order in $\boldsymbol{h}$, the perturbation in the wave function can be written as:

$$\begin{aligned}
\delta\Psi \approx \Psi - \tilde{\Psi} = &\begin{pmatrix} 0 \\ i\frac{\lambda_R \hbar}{2\Delta}(\delta k_x + i\delta k_y)\sqrt{\frac{\mu_2}{g}} + \frac{1}{2\Delta}(h_x + ih_y)\sqrt{\frac{\mu_2}{g}} \end{pmatrix} \\
&-i\delta\boldsymbol{k}\cdot\boldsymbol{r} \begin{pmatrix} \sqrt{\frac{\mu_2}{g}} \\ +\frac{\lambda_R}{4\Delta\sqrt{g}} \frac{m\omega_0^2 \hbar}{\sqrt{\mu_2}} (x+iy) - i\frac{\lambda_R \hbar}{2\Delta}(\delta k_x + i\delta k_y)\sqrt{\frac{\mu_2}{g}} - \frac{1}{2\Delta}(h_x + ih_y)\sqrt{\frac{\mu_2)}{g}} \end{pmatrix}
\end{aligned}$$

where we have expanded $e^{i\delta\boldsymbol{k}\cdot\boldsymbol{r}}$ and introduced the notation $\mu_2 = \mu + \Delta - V(x,y)$. Then we see that:

$$\begin{aligned}
[\langle 0|\hat{\Sigma}_x|\delta\Psi\rangle - \langle \delta\Psi|\hat{\Sigma}_x|0\rangle] &= \int [\psi_1^\dagger \delta\psi_2 + \psi_2^\dagger \delta\psi_1 - \delta\psi_1^\dagger \psi_2 - \delta\psi_2^\dagger \psi_1] d^2\mathbf{r} \\
&= \frac{i h_y N}{\Delta}
\end{aligned}$$

where we have omitted all of the (straightforward) algebraic steps between the first and second lines for compactness. Then:

$$\frac{\partial}{\partial h_y}[\langle 0|\hat{\Sigma}_x|\delta\Psi\rangle - \langle\delta\Psi|\hat{\Sigma}_x|0\rangle] = \frac{iN}{\Delta} \tag{E.31}$$

Combining all these results, we find that the fourth term in m_{-3} is proportional to:

$$\begin{aligned}
\sum_n \frac{4}{(E_n - E_0)}|\langle 0|\hat{\Sigma}_-|n\rangle|^2 &= -\frac{\chi_{xx}}{2} - \frac{\chi_{yy}}{2} + i\frac{\partial}{\partial h_y}[\langle 0|\hat{\Sigma}_x|\delta\Psi\rangle - \langle\delta\Psi|\hat{\Sigma}_x|0\rangle] \\
&= \frac{\lambda_R^2 MN}{\Delta}\frac{1}{-\lambda_R^2 M + \Delta} \\
\sum_n \frac{4}{(E_n - E_0)}|\langle 0|\hat{\Sigma}_+|n\rangle|^2 &= -\frac{\chi_{xx}}{2} - \frac{\chi_{yy}}{2} - i\frac{\partial}{\partial h_y}[\langle 0|\hat{\Sigma}_x|\delta\Psi\rangle - \langle\delta\Psi|\hat{\Sigma}_x|0\rangle] \\
&= \frac{\lambda_R^2 MN}{\Delta}\frac{1}{-\lambda_R^2 M + \Delta} + \frac{2N}{\Delta}
\end{aligned} \tag{E.32}$$

E.3 The Dipole Mode Frequencies

We can calculate an upper bound on the dipole mode frequencies through:

$$\hbar\omega_{\pm 1} \leq \sqrt{\frac{m_{-1}(\hat{D}_{\pm 1})}{m_{-3}(\hat{D}_{\pm 1})}}. \tag{E.33}$$

When we put together all the above results, we find:

$$\begin{aligned}
\frac{\omega_{-1}^2}{\omega_0^2} &= \frac{1}{1 - \frac{\lambda_R^2 M}{\Delta} + \frac{(\lambda_R^2 M)^2}{\Delta}\frac{1}{-\lambda_R^2 m + \Delta} + 2\frac{\lambda_R^2 M}{\Delta}} = \frac{1}{1 + \frac{\lambda_R^2 M}{\Delta} + \frac{(\lambda_R^2 M)^2}{\Delta}\frac{1}{-\lambda_R^2 M + \Delta}} \\
\frac{\omega_{+1}^2}{\omega_0^2} &= \frac{1}{1 + \frac{\lambda_R^2 M}{\Delta} + \frac{(\lambda_R^2 M)^2}{\Delta}\frac{1}{-\lambda_R^2 M + \Delta}}.
\end{aligned} \tag{E.34}$$

From this we can see that:

$$\frac{\omega_{\pm 1}^2}{\omega_0^2} = (1 - \zeta) = \frac{M}{M^*} \tag{E.35}$$

Therefore, this ansatz perfectly captures the behaviour of our system as $\chi \to 0$. However, exploring the splitting due to Berry curvature effects is more difficult as

this is proportional to χ. To go further, we would need to find a better ansatz which does not assume $|\psi_2|^2$ is negligible.

Appendix F

The Dipole Operator Approach for 1D Spin Orbit Coupling

In this Appendix, we demonstrate how the dipole operator approach can also be used to derive the effects of 1D spin-orbit coupling on the dipole mode. This was previously studied theoretically in Ref. [215, 241] using a sum rule method. Our method is significantly easier and is able to replicate all results for spin-independent interactions. For ease of comparison, we are guided by the notation of these references. The Hamiltonian is:

$$\begin{aligned}\hat{H} &= \sum_i \hat{h}_0(i) + \frac{1}{2} g_{2\mathrm{D}} \sum_{i \neq j} \delta(x_i - x_j)\delta(y_i - y_j) \\ \hat{h}_0 &= \frac{1}{2}\left[(p_x - k_0\hat{\sigma}_z)^2 + p_\perp^2\right] + \frac{\Omega_R}{2}\hat{\sigma}_x + \frac{\Delta}{2}\hat{\sigma}_z + V(x,y). \end{aligned} \tag{F.1}$$

where $M = \hbar = 1$ and k_0 is the spin-orbit coupling strength. This Hamiltonian has been realised experimentally (Section 2.2.1), where Ω_R corresponds to the Raman coupling strength and k_0 is the momentum transfer in from the two Raman beams. We have taken the interactions to be independent of spin[1], which is a good approximation for ^{87}Rb. We also set $\Delta = 0$ to compare our results with those of Ref. [215].

The Hamiltonian in Eq. F.1 has a phase diagram depending on k_0, Ω and the spin-dependent interactions[241]. The three possible states are the "spin-polarized"

[1]The effects of spin-dependent interactions on the dipole mode was also discussed in Ref. [215].

phase, the stripe phase and the single-minimum phase. In the spin-polarized phase (Phase II in the terminology of Ref. [241]), the Bose-Einstein condensate forms at one nonzero momentum. In the stripe phase, condensation occurs in a superposition of plane waves with opposite nonzero momenta. However, this phase is only stabilised by spin-dependent interactions and does not occur for the spin-independent interactions that we consider in this Appendix. Finally, the single minimum phase (Phase III) consists of a Bose-Einstein condensate at zero momentum; this is analogous to the phase considered for 2D Rashba spin-orbit coupling in the main text.

There is no Berry curvature for 1D spin-orbit coupling and so the dipole mode is always given in hydrodynamics by: $\omega = \sqrt{\frac{M}{M^*}}\omega_0$ (Section 4.2). We can calculate the effective mass from the single-particle spectrum of $\hat{h}_0$:

$$\varepsilon(p_x) = \frac{1}{2}\left(k_0^2 + p_x^2 + p_\perp^2 - \sqrt{\Omega_R^2 + 4k_0^2 p_x^2}\right) \tag{F.2}$$

For $\Omega_R > 2k_0$, this has a single minimum at $p_x = 0$ and Phase III will form[241]. For $\Omega_R < 2k_0$, there are two minima at $p_x = \pm k_0\sqrt{1 - \frac{\Omega_R^2}{4k_0^4}}$. One minimum will be selected by a discrete symmetry breaking and the condensate will appear in Phase II. In the zero momentum phase, the effective mass is $\frac{1}{M^*} = 1 - \frac{2k_0^2}{\Omega_R}$, while in the spin-polarized phase, it is $\frac{1}{M^*} = 1 - \frac{\Omega_R^2}{4k_0^4}$. In what follows, we will use the dimensionless parameters of our system. Two of these are $\chi = \omega_0/\Omega_R$ and $\zeta = k_0^2/\Omega_R$ in direct analogy to those chosen in Section 4.3. Hence, the hydrodynamic mode frequency can be written as $\omega = \omega_0\sqrt{1-2\zeta}$ in Phase III, and $\omega = \omega_0\sqrt{1 - 1/4\zeta^2}$ in Phase II.

In 1D, the dipole operator is simply $\hat{X} = \sum_i \hat{x}_i$. Therefore the Heisenberg equations of motion are:

$$\begin{aligned}
\dot{\hat{X}} &= \hat{P}_x - k_0\hat{\Sigma}_z \\
\dot{\hat{P}} &= -\omega_0^2\hat{X} \\
\dot{\hat{\Sigma}}_z &= \Omega_R\hat{\Sigma}_y \\
\dot{\hat{\Sigma}}_x &= 2\sum_i k_0 p_x\hat{\sigma}_y \\
\dot{\hat{\Sigma}}_y &= -\Omega_R\hat{\Sigma}_z - 2\sum_i k_0 p_x\hat{\sigma}_x
\end{aligned} \tag{F.3}$$

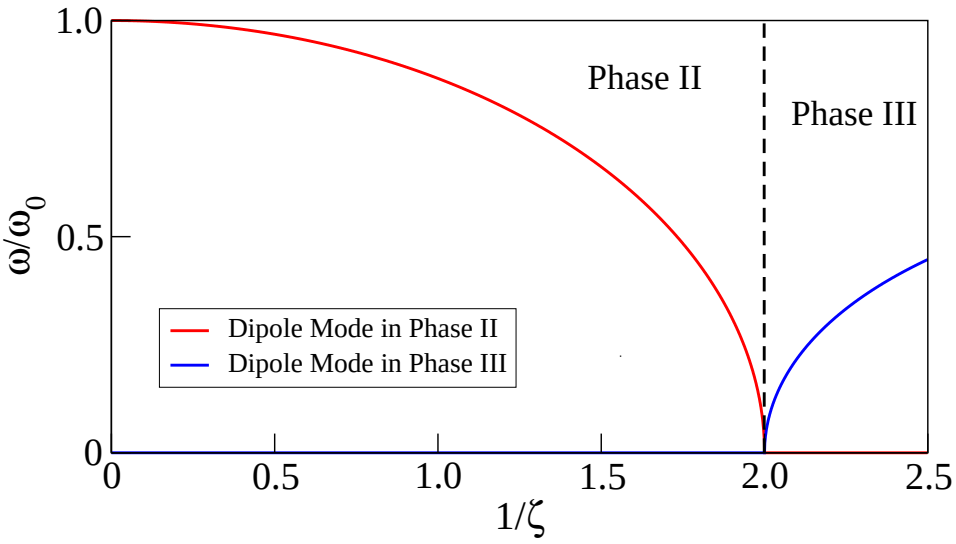

Figure F.1: The dipole mode from the dipole operator approach for Eq. F.1 with $k_0^2 = 2\pi \times 4.42$ Hz and $\omega_0 = 2\pi \times 45$ Hz. These parameters are chosen to match the experiment of Ref. [130] and to allow a direct comparison with Fig 2 of Ref. [215]. For this purpose, the x axis is chosen to be $1/\zeta$ rather than ζ. Our results show excellent agreement both with the hydrodynamic approach described in the text and with Ref. [215] which uses a sum rule approach. (For a comparison to the experiment of Ref. [130], see Fig 2 of Ref. [215]). The dashed line shows the transition from the spin-polarized phase (Phase II) to the zero-momentum phase (Phase III). However, as we assume spin-independent interactions, we have not included the transition to the stripe phase. Ref. [215] predicts this transition occurs for very low $1/\zeta \approx 0.2$ for ^{87}Rb (for which $a_{\uparrow\uparrow} = a_{\downarrow\downarrow} = 101.20a_B$, $a_{\uparrow\downarrow} = 100.99a_B$). (We also note that greater spin-dependence in the interactions would change the transition point between Phases II and III[215].)

As in Section 4.5.1, to go further we must make certain approximations. These now depend on the phase of the system, so we shall treat each phase in turn.

Zero Momentum Phase (Phase III)

In the single-minimum phase, we can use that $\langle 0|\sigma_x|0\rangle \simeq -1$, $\langle 0|\sigma_y|0\rangle \simeq 0$ and $\langle 0|p_x|0\rangle \simeq 0$, i.e. the atoms are at zero momentum and are all polarised along the x direction[215]. Then we have:

$$\dot{\hat{\Sigma}}_x \simeq 0, \qquad \dot{\hat{\Sigma}}_y = -\Omega_R \hat{\Sigma}_z + 2k_0 \hat{P}_x. \tag{F.4}$$

So we see that $\hat{\Sigma}_x$ decouples, and we are left with four equations. We assume that the time dependence goes as $e^{-i\omega t}$, and write our set of operator equations in the form of an eigenvalue problem:

$$-i\frac{\omega}{\omega_0}\begin{pmatrix}\hat{X}'\\ \hat{P}'_x\\ \hat{\Sigma}_z\\ \hat{\Sigma}_y\end{pmatrix} = \begin{pmatrix}0 & 1 & -\sqrt{\frac{\zeta}{\chi}} & 0\\ -1 & 0 & 0 & 0\\ 0 & 0 & 0 & \frac{1}{\chi}\\ 0 & 2\sqrt{\frac{\zeta}{\chi}} & -\frac{1}{\chi} & 0\end{pmatrix}\begin{pmatrix}\hat{X}'\\ \hat{P}'_x\\ \hat{\Sigma}_z\\ \hat{\Sigma}_y\end{pmatrix}$$

where we have defined the dimensionless operators $\hat{X}' = \sqrt{\omega_x}\hat{X}$ and $\hat{P}' = \frac{1}{\sqrt{\omega_x}}\hat{P}$ (as $M = \hbar = 1$). The low energy dipole mode[2] is shown in Figure F.1. This mode shows excellent qualitative agreement with the results of Ref. [215] which uses a sum rule approach. Quantitatively, we expect from hydrodynamics that the mode should have frequency:

$$\omega^2 = \frac{M}{M^*}\omega_0^2 = \left(1 - \frac{2k_0^2}{\Omega}\right)\omega_0^2 = (1-2\zeta)\omega_0^2. \tag{F.5}$$

The Taylor series expansion of the mode found in the dipole operator approach is:

$$\omega = \omega_0^2(1-2\zeta) - \omega_0^2\left(\frac{2}{\zeta} - 4\right)\chi^2\zeta^2 + \mathcal{O}(\chi^4). \tag{F.6}$$

The dipole operator agrees perfectly with the sum rule and hydrodynamic result in the limit that χ is small. For larger values of χ, we expect our approximations to break down as different spin eigenstates are mixed.

"Spin-Polarized" Phase (Phase II)

Now let us turn to Phase II, the "spin-polarized" phase. The key difference to the zero-momentum phase is that the Bose-Einstein condensate has formed at nonzero

[2]The other mode found is high in energy and represents transitions to the higher band.

momentum. We take this into account by approximating:

$$\begin{aligned}
\dot{\hat{\Sigma}}_x &\simeq \pm 2k_0^2\sqrt{1-\frac{\Omega_R^2}{4k_0^4}}\hat{\Sigma}_y \\
\dot{\hat{\Sigma}}_y &\simeq -\Omega_R\hat{\Sigma}_z + 2k_0\frac{\Omega_R}{2k_0^2}\hat{P}_x \mp 2k_0^2\sqrt{1-\frac{\Omega_R^2}{4k_0^4}}\hat{\Sigma}_x,
\end{aligned} \tag{F.7}$$

where we have used that in this phase[215]:

$$\begin{aligned}
\langle 0|\hat{\Sigma}_x|0\rangle &\simeq -\frac{\Omega_R}{2k_0^2} \\
\langle 0|\hat{P}_x|0\rangle &\simeq \pm k_0\sqrt{1-\frac{\Omega_R^2}{4k_0^4}} \\
\langle 0|\hat{\Sigma}_y|0\rangle &\simeq 0.
\end{aligned} \tag{F.8}$$

The resulting set of operator equations can be written in the dimensionless form:

$$-i\frac{\omega}{\omega_0}\begin{pmatrix}\hat{X}'\\ \hat{P}'\\ \hat{\Sigma}_z\\ \hat{\Sigma}_y\\ \hat{\Sigma}_x\end{pmatrix} = \begin{pmatrix} 0 & -1 & \sqrt{\frac{\zeta}{\chi}} & 0 & 0 \\ 1 & 0 & 0 & 0 & 0 \\ 0 & 0 & 0 & -\frac{1}{\chi} & 0 \\ 0 & -\sqrt{\frac{1}{\zeta\chi}} & \frac{1}{\chi} & 0 & \pm 2\frac{\zeta}{\chi}\sqrt{1-\frac{1}{4\zeta^2}} \\ 0 & 0 & 0 & \mp 2\frac{\zeta}{\chi}\sqrt{1-\frac{1}{4\zeta^2}} & 0 \end{pmatrix}\begin{pmatrix}\hat{X}'\\ \hat{P}'\\ \hat{\Sigma}_z\\ \hat{\Sigma}_y\\ \hat{\Sigma}_x\end{pmatrix} \tag{F.9}$$

Upon solving these equations, we now get a zero mode, as we have not used the constraint that the magnitude of the spin vector is fixed (i.e. $\sigma_x^2+\sigma_y^2+\sigma_z^2=1$). This mode is therefore not physical and can be neglected. The low energy dipole mode is shown in Figure F.1. This also shows excellent agreement both with the sum rule approach of Ref. [215] and the hydrodynamic prediction:

$$\omega^2 = \frac{M}{M^*}\omega_0^2 = \left(1-\frac{\Omega_R^2}{4k_0^4}\right)\omega_0^2 = (1-\frac{1}{4\zeta^2})\omega_0^2. \tag{F.10}$$

The Taylor series expansion of the mode in the dipole operator approach is for comparison:

$$\frac{\omega^2}{\omega_0^2} = \left(1-\frac{1}{4\zeta^2}\right) + \frac{\left(\frac{1}{\zeta^2}-4\right)\chi^2}{64\zeta^4} + \mathcal{O}(\chi^4), \tag{F.11}$$

which again agrees for small χ.

Therefore, in summary, we have shown how the dipole mode can be derived from the dipole operator approach for 1D SO-coupling for spin-independent interactions. This has allowed direct comparison with the experimental results of Ref. [130], as well as two other theoretical methods: the sum rule approach[215] and hydrodynamics.

Appendix G

Higher-Order Corrections Beyond the Effective Mass

In Section 4, we have assumed that the energy dispersion is completely characterised by an isotropic effective mass, $M^* = \hbar^2 / \left(\partial^2 E / \partial \boldsymbol{p}^2\right)$. In most systems, the dispersion is not perfectly quadratic and so there can be cubic, quartic and further higher order contributions to this approximation. In this Appendix, we investigate these terms in more detail for the models considered in the main text. We first discuss 2D Rashba spin-orbit coupling and then a general multi-band Hamiltonian.

G.1 2D Rashba Spin-Orbit Coupling

We begin from the Hamiltonian in Eq. 4.10. The single-particle energy spectrum is given by $\varepsilon_\pm = \frac{p^2}{2M} \pm \sqrt{\lambda_R^2 p^2 + \Delta^2}$. When $\zeta \equiv \frac{\lambda_R^2 M}{\Delta} < 1$, there is a single minimum in the lower band at $p = 0$. The effective mass at this point is:

$$\frac{1}{M^*} = \frac{\partial^2 \varepsilon_-(p)}{\partial p^2} = \frac{1}{M} - \frac{\lambda_R^2}{(\lambda_R^2 p^2 + \Delta^2)^{1/2}} + \frac{p^2 \lambda_R^4}{(\lambda_R^2 p^2 + \Delta^2)^{3/2}} \xrightarrow{p=0} \frac{1}{M} - \frac{\lambda_R^2}{\Delta} \quad \text{(G.1)}$$

From the single-particle energy spectrum, we can also compute the cubic correction:

$$\frac{\partial^3 \varepsilon_-(p)}{\partial p^3} = \frac{\lambda_R^4 p}{(\lambda_R^2 p^2 + \Delta^2)^{3/2}} + \frac{2p\lambda_R^4}{(\lambda_R^2 p^2 + \Delta^2)^{3/2}} - \frac{3p^3 \lambda_R^6}{(\lambda_R^2 p^2 + \Delta^2)^{5/2}} \xrightarrow{p=0} 0, \quad \text{(G.2)}$$

and the quartic correction:

$$\frac{\partial^4 \varepsilon_-(p)}{\partial p^4} = \frac{\lambda_R^4}{(\lambda_R^2 p^2+\Delta^2)^{3/2}} - \frac{3\lambda_R^6 p^2}{(\lambda_R^2 p^2+\Delta^2)^{5/2}} + \frac{2\lambda_R^4}{(\lambda_R^2 p^2+\Delta^2)^{3/2}} - \frac{6p^2\lambda_R^6}{(\lambda_R^2 p^2+\Delta^2)^{5/2}} - \frac{9p^2\lambda_R^6}{(\lambda_R^2 p^2+\Delta^2)^{5/2}} + \frac{15p^4\lambda_R^8}{(\lambda_R^2 p^2+\Delta^2)^{7/2}} \xrightarrow{p=0} \frac{3\lambda_R^4}{\Delta^3}. \quad \text{(G.3)}$$

Higher order corrections scale with increasing powers of the Zeeman shift, Δ. We compare these corrections to the Berry curvature at $\boldsymbol{p} = 0$ for the lower band: $\Omega = \frac{\lambda_R^2\hbar^2}{2\Delta^2}$. Therefore, for a large band-gap, Δ, the Berry curvature will always be the next-order correction after the effective mass.

G.2 A General Multi-Band Hamiltonian

We can use "$\boldsymbol{k}\cdot\boldsymbol{p}$" perturbation theory to ask when cubic and higher-order contributions from the dispersion may be important. We shall compare these contributions to the Berry curvature:

$$\Omega_n \equiv \frac{i\hbar^2}{M^2}\sum_{l\neq n}\frac{\pi_{nl}^x\pi_{ln}^y - \pi_{nl}^y\pi_{ln}^x}{(E_l-E_n)^2}. \quad \text{(G.4)}$$

where $\pi_{nl}^\alpha \equiv \langle n|\hat{p}^\alpha|l\rangle$ is the inter-band matrix element of $\hat{p}$ and where $|n\rangle = |n\boldsymbol{k}_0\rangle$ is the Bloch function at $\boldsymbol{k}_0$.

Review of $\boldsymbol{k}\cdot\boldsymbol{p}$ Perturbation Theory

We consider the simple Hamiltonian $\hat{H} = \frac{\hat{\boldsymbol{p}}^2}{2M} + U(\boldsymbol{r})$ where $U(\boldsymbol{r})$ is the lattice potential[227]. The wave function is $e^{i\boldsymbol{k}\cdot\boldsymbol{r}}|n\boldsymbol{k}\rangle$and the Schrödinger equation is then:

$$\left[\frac{\hat{\boldsymbol{p}}^2}{2M} + V + \frac{\hbar^2\boldsymbol{k}^2}{2M} + \frac{\hbar\boldsymbol{k}}{M}\hat{\boldsymbol{p}}\right]|n\boldsymbol{k}\rangle = E_{n\boldsymbol{k}}|n\boldsymbol{k}\rangle \quad \text{(G.5)}$$

Then we expand in $\boldsymbol{k} = \boldsymbol{k}_0 + \delta\boldsymbol{k}$ up to third order:

$$\begin{aligned} E_{n\boldsymbol{k}} &= E_{n\boldsymbol{k}_0} + \delta k^\alpha\partial_\alpha E_n + \frac{1}{2}\delta k^\alpha\delta k^\beta\partial_\alpha\partial_\beta E_n + \frac{1}{3!}\delta k^\alpha\delta k^\beta\delta k^\gamma\partial_\alpha\partial_\beta\partial_\gamma E_n + ... \\ |n\boldsymbol{k}\rangle &= |n\rangle + \sum_{m\neq n} a_m^{(1)}|m\rangle + \sum_{m\neq n} a_m^{(2)}|m\rangle + \sum_{m\neq n} a_m^{(3)}|m\rangle + ... \end{aligned}$$

where $|n\rangle = |n\boldsymbol{k}_0\rangle$ and ∂_α means the partial derivative with respect to $\boldsymbol{k}$ as evaluated at $\boldsymbol{k}_0$. Now we collect terms of different orders; the zeroth order terms give[227]:

$$\left[\frac{\hat{\boldsymbol{p}}^2}{2M} + V + \frac{\hbar^2\boldsymbol{k}_0^2}{2M} + \frac{\hbar\boldsymbol{k}_0}{M}\hat{\boldsymbol{p}}\right]|n\rangle = E_{n\boldsymbol{k}_0}|n\rangle. \tag{G.6}$$

The first order terms are:

$$\delta k^\alpha\left[\frac{\hbar^2 k_0^\alpha}{M} + \frac{\hbar}{M}\hat{p}^\alpha\right]|n\rangle + \sum_{m\neq n} E_{m\boldsymbol{k}_0}a_m^{(1)}|m\rangle = \delta k^\alpha\partial_\alpha E_n|n\rangle + E_{n\boldsymbol{k}_0}\sum_{m\neq n}a_m^{(1)}|m\rangle. \tag{G.7}$$

To proceed, we dot this equation with the state $\langle l|$ and perform the integration over one unit cell[227]. If we take $n = l$ this gives the group velocity:

$$\frac{\hbar k_0^\alpha}{M} + \frac{1}{M}\pi_{nn}^\alpha = \frac{1}{\hbar}\partial_\alpha E_n \equiv v_n^\alpha \tag{G.8}$$

If we take $n \neq l$, we find:

$$\begin{aligned}
&\delta k^\alpha\frac{\hbar}{M}\pi_{ln}^\alpha + E_l a_l^{(1)} = E_n a_l^{(1)} \\
&a_l^{(1)} = \frac{\hbar}{M}\frac{\delta\boldsymbol{k}\cdot\boldsymbol{\pi}_{ln}}{E_n - E_l}
\end{aligned} \tag{G.9}$$

We shall use this co-efficient $a_l^{(1)}$ when we proceed to second order:

$$\begin{aligned}
&\sum_{m\neq n} E_{m\boldsymbol{k}_0}a_m^{(2)}|m\rangle + \delta k^\alpha\delta k^\alpha\frac{\hbar^2}{2M}|n\rangle + \delta k^\alpha\left[\frac{\hbar^2 k_0^\alpha}{M} + \frac{\hbar}{M}\hat{p}^\alpha\right]\sum_{m\neq n}a_m^{(1)}|m\rangle = \\
&\frac{1}{2}\delta k^\alpha\delta k^\beta\partial_\alpha\partial_\beta E_n|n\rangle + \delta k^\alpha\partial_\alpha E_n\sum_{m\neq n}a_m^{(1)}|m\rangle + E_{n\boldsymbol{k}_0}\sum_{m\neq n}a_m^{(2)}|m\rangle
\end{aligned} \tag{G.10}$$

Again we dot with $\langle l|$ and perform the integration over one unit cell[227]. If we take $n = l$ this leads to:

$$\begin{aligned}
\partial_\alpha\partial_\beta E_n &= \frac{\hbar^2}{M}\delta_{\alpha\beta} + \sum_{m\neq n}\frac{\hbar^2}{M^2}\frac{\pi_{nm}^\alpha\pi_{mn}^\beta + \pi_{nm}^\beta\pi_{mn}^\alpha}{E_n - E_m} \\
\frac{1}{M^*} &\equiv \frac{\delta_{\alpha\beta}}{M} + \frac{1}{M^2}\sum_{m\neq n}\frac{\pi_{nm}^\alpha\pi_{mn}^\beta + \pi_{nm}^\beta\pi_{mn}^\alpha}{E_n - E_m}
\end{aligned} \tag{G.11}$$

This is where a standard text-book[227] leaves the calculation. As we are interested in higher-order corrections we continue following the same procedure.

Cubic Corrections in $k \cdot p$ Perturbation Theory

We dot Eq. G.10 with $\langle l|$ (with $l \neq n$) to find:

$$\begin{aligned} E_l a_l^{(2)} &+ \delta k^\alpha \frac{\hbar^2 k_0^\alpha}{M} a_l^{(1)} + \delta k^\alpha \sum_{m\neq n} \frac{\hbar}{M} \pi_{lm}^\alpha a_m^{(1)} = \delta k^\alpha \partial_\alpha E_n a_l^{(1)} + E_n a_l^{(2)} \\ (E_l - E_n) a_l^{(2)} &= \delta k^\alpha \left(\partial_\alpha E_n - \frac{\hbar^2 k_0^\alpha}{M} \right) a_l^{(1)} - \delta k^\alpha \sum_{m\neq n} \frac{\hbar}{M} \pi_{lm}^\alpha a_m^{(1)} \\ (E_l - E_n) a_l^{(2)} &= \delta k^\alpha \frac{\hbar}{M} \pi_{nn}^\alpha a_l^{(1)} - \delta k^\alpha \sum_{m\neq n} \frac{\hbar}{M} \pi_{lm}^\alpha a_m^{(1)}. \end{aligned} \tag{G.12}$$

We manipulate this further to give:

$$\begin{aligned} a_l^{(2)} &= -\frac{\hbar^2}{M^2} \frac{\delta k^\alpha \pi_{nn}^\alpha \delta k^\beta \pi_{ln}^\beta}{(E_n - E_l)^2} + \sum_{m\neq n} \frac{\hbar^2}{M^2} \frac{\delta k^\alpha \pi_{lm}^\alpha \delta k^\beta \pi_{mn}^\beta}{(E_n - E_m)(E_n - E_l)} \\ &= \frac{\hbar^2}{M} \frac{\delta k^\alpha (v_l^\alpha - v_n^\alpha) \delta k^\beta \pi_{ln}^\beta}{(E_n - E_l)^2} + \sum_{m\neq l,n} \frac{\hbar^2}{M^2} \frac{\delta k^\alpha \pi_{lm}^\alpha \delta k^\beta \pi_{mn}^\beta}{(E_n - E_m)(E_n - E_l)}. \end{aligned} \tag{G.13}$$

We can use this to calculate the cubic correction from the dispersion. The third order terms are:

$$\begin{aligned} &\sum_{m\neq n} E_{m\boldsymbol{k}_0} a_m^{(3)} |m\rangle + \delta k^\alpha \delta k^\alpha \frac{\hbar^2}{2M} \sum_{m\neq 0} a_m^{(1)} |m\rangle + \delta k^\alpha \left[\frac{\hbar^2 k_0^\alpha}{M} + \frac{\hbar}{M} \hat{p^\alpha} \right] \sum_{m\neq n} a_m^{(2)} |m\rangle = \\ &\quad \frac{1}{6} \delta k^\alpha \delta k^\beta \delta k^\gamma \partial_\alpha \partial_\beta \partial_\gamma E_n |n\rangle + \frac{1}{2} \delta k^\alpha \delta k^\beta \partial_\alpha \partial_\beta E_n \sum_{m\neq n} a_m^{(1)} |m\rangle \\ &\quad + \delta k^\alpha \ \partial_\alpha E_n \sum_{m\neq n} a_m^{(2)} |m\rangle + E_{n\boldsymbol{k}_0} \sum_{m\neq n} a_m^{(3)} |n\rangle \end{aligned} \tag{G.14}$$

We dot this with $\langle l|$ and take $n = l$ to find:

$$\begin{aligned} &\frac{1}{6} \delta k^\alpha \delta k^\beta \delta k^\gamma \partial_\alpha \partial_\beta \partial_\gamma E_n = \delta k^\alpha \sum_{l\neq n} \frac{\hbar}{M} \pi_{nl}^\alpha a_l^{(2)} \\ &\quad = \frac{\hbar^3}{M^2} \sum_{l\neq n} \frac{\delta k^\gamma (v_l^\gamma - v_n^\gamma) \delta k^\beta \pi_{ln}^\beta \delta k^\alpha \pi_{nl}^\alpha}{(E_n - E_l)^2} + \sum_{m\neq l,n} \sum_{l\neq n} \frac{\hbar^3}{M^2} \frac{\delta k^\gamma \pi_{lm}^\gamma \delta k^\beta \pi_{mn}^\beta \delta k^\alpha \pi_{nl}^\alpha}{(E_n - E_m)(E_n - E_l)} \end{aligned}$$

These terms are proportional to the inverse squared power of the band-gap and so would enter the dynamical equations at the same order as the Berry curvature. However, we know that cubic corrections will vanish when we are at a high symmetry

point in the Brillouin zone, as cubic terms do not preserve inversion symmetry. Away from high symmetry points, we see that these terms need not vanish and could play an important role.

Finally, we can go further and find that each higher order scales with one higher inverse power of the band gap. For example, quartic corrections scale like $(E_n - E_0)^{-3}$ (as in the 2D Rashba model). All these higher order corrections will therefore be smaller than the Berry curvature when the band-gap is large, and so they can be neglected.

Bibliography

[1] H. M. Price and N. R. Cooper, Phys. Rev. A **85**, 033620 (2012).

[2] H. M. Price and N. R. Cooper, arXiv:1306.4796.

[3] H. M. Price and N. R. Cooper, Phys. Rev. A **83**, 061605 (2011).

[4] D. J. Thouless, M. Kohmoto, M. P. Nightingale, and M. den Nijs, Phys. Rev. Lett. **49**, 405 (1982).

[5] M. Z. Hasan and C. L. Kane, Rev. Mod. Phys. **82**, 3045 (2010).

[6] X.-L. Qi and S.-C. Zhang, Rev. Mod. Phys. **83**, 1057 (2011).

[7] M. Ueda, *Fundamentals and New Frontiers of Bose-Einstein Condensation* (World Scientific Publishing Co., Singapore, 2010).

[8] C. J. Pethick and H. Smith, *Bose-Einstein Condensation in Dilute Gases* (Cambridge University Press, Cambridge, 2001).

[9] M. V. Berry, Proc. R. Soc. London, Ser. A **392**, 45 (1984).

[10] T. Kato, J. Phys. Soc. Jpn. **5**, 435 (1950).

[11] V. Fock, Z. Phys **49**, 323 (1928).

[12] D. Xiao, M.-C. Chang, and Q. Niu, Rev. Mod. Phys. **82**, 1959 (2010).

[13] M. Born and R. Oppenheimer, Ann. Phys. (Berlin) **389**, 457 (1927).

[14] C. A. Mead and D. G. Truhlar, J. Chem. Phys. **70**, 2284 (1979).

[15] F. Wilczek and A. Zee, Phys. Rev. Lett. **52**, 2111 (1984).

[16] B. Simon, Phys. Rev. Lett. **51**, 2167 (1983).

[17] T. Jungwirth, Q. Niu, and A. H. MacDonald, Phys. Rev. Lett. **88**, 207208 (2002).

[18] M. Onoda and N. Nagaosa, J. Phys. Soc. Jpn. **71**, 19 (2002).

[19] F. D. M. Haldane, Phys. Rev. Lett. **93**, 206602 (2004).

[20] N. Nagaosa, J. Sinova, S. Onoda, A. H. MacDonald, and N. P. Ong, Rev. Mod. Phys. **82**, 1539 (2010).

[21] R. Karplus and J. M. Luttinger, Phys. Rev. **95**, 1154 (1954).

[22] M.-C. Chang and Q. Niu, Phys. Rev. Lett. **75**, 1348 (1995).

[23] M.-C. Chang and Q. Niu, Phys. Rev. B **53**, 7010 (1996).

[24] G. Sundaram and Q. Niu, Phys. Rev. B **59**, 14915 (1999).

[25] R. Rajaraman, *Solitons and Instantons* (North Holland, Amsterdam, 1982).

[26] P. Chaikin and T. Lubensky, *Principles of Condensed Matter Physics* (Cambridge University Press, Cambridge, 2000).

[27] T. H. R. Skyrme, Proc. Roy. Soc. Lond. A **260**, 127 (1961).

[28] S. L. Sondhi, A. Karlhede, S. A. Kivelson, and E. H. Rezayi, Phys. Rev. B **47**, 16419 (1993).

[29] S. Mülbauer *et al.*, Science **323**, 915 (2009).

[30] X. Z. Yu *et al.*, Nature **465**, 901 (2010).

[31] C. Pfleiderer, Nat. Phys. **7**, 673 (2011).

[32] P. W. Anderson and G. Toulouse, Phys. Rev. Lett. **38**, 508 (1977).

[33] M. H. Anderson, J. R. Ensher, M. R. Matthews, C. E. Wieman, and E. A. Cornell, Science **269**, 198 (1995).

[34] K. B. Davis *et al.*, Phys. Rev. Lett. **75**, 3969 (1995).

[35] M. Greiner, C. A. Regal, and D. S. Jin, Nature **426**, 537 (2003).

[36] S. Giorgini, L. P. Pitaevskii, and S. Stringari, Rev. Mod. Phys. **80**, 1215 (2008).

[37] L. Pitaevskii and S. Stringari, *Bose-Einstein Condensation* (International Series of Monographs on Physics, Clarendon Press, Oxford, 2003).

[38] F. Dalfovo, S. Giorgini, L. P. Pitaevskii, and S. Stringari, Rev. Mod. Phys. **71**, 463 (1999).

[39] A. J. Leggett, Rev. Mod. Phys. **73**, 307 (2001).

[40] I. Bloch, J. Dalibard, and W. Zwerger, Rev. Mod. Phys. **80**, 885 (2008).

[41] O. Morsch and M. Oberthaler, Rev. Mod. Phys. **78**, 179 (2006).

[42] J. Dalibard, F. Gerbier, G. Juzeliūnas, and P. Öhberg, Rev. Mod. Phys. **83**, 1523 (2011).

[43] http://jila.colorado.edu/bec/cornellgroup/gallery/images/, Accessed: 03-07-2013.

[44] M. R. Matthews *et al.*, Phys. Rev. Lett. **83**, 2498 (1999).

[45] M. R. Andrews *et al.*, Science **275**, 637 (1997).

[46] T. Kinoshita, T. Wenger, and D. S. Weiss, Science **305**, 1125 (2004).

[47] Z. Hadzibabic, P. Krüger, M. Cheneau, B. Battelier, and J. Dalibard, Nature **441**, 1118 (2006).

[48] M. Greiner, O. Mandel, T. Esslinger, T. W. Hansch, and I. Bloch, Nature **415**, 39 (2002).

[49] W. S. Bakr *et al.*, Science **329**, 547 (2010).

[50] C. Chin, R. Grimm, P. Julienne, and E. Tiesinga, Rev. Mod. Phys. **82**, 1225 (2010).

[51] L. S. Leslie, A. Hansen, K. C. Wright, B. M. Deutsch, and N. P. Bigelow, Phys. Rev. Lett. **103**, 250401 (2009).

[52] K. Kasamatsu, M. Tsubota, and M. Ueda, Phys. Rev. A **71**, 043611 (2005).

[53] J. Ruostekoski and J. R. Anglin, Phys. Rev. Lett. **86**, 3934 (2001).

[54] R. A. Battye, N. R. Cooper, and P. M. Sutcliffe, Phys. Rev. Lett. **88**, 080401 (2002).

[55] K. Kasamatsu, M. Tsubota, and M. Ueda, Phys. Rev. Lett. **93**, 250406 (2004).

[56] R. W. Cherng and E. Demler, Phys. Rev. A **83**, 053614 (2011).

[57] J. F. S. Brachmann, W. S. Bakr, J. Gillen, A. Peng, and M. Greiner, Opt. Express **19**, 12984 (2011).

[58] J.-Y. Choi *et al.*, New J. Phys. **14**, 053013 (2012).

[59] A. E. Leanhardt, Y. Shin, D. Kielpinski, D. E. Pritchard, and W. Ketterle, Phys. Rev. Lett. **90**, 140403 (2003).

[60] J.-Y. Choi, W. J. Kwon, and Y.-I. Shin, Phys. Rev. Lett. **108**, 035301 (2012).

[61] J. I. Gillen *et al.*, Phys. Rev. A **80**, 021602 (2009).

[62] M. Greiner, http://greiner.physics.harvard.edu/research.html, Accessed: 03-07-2013.

[63] D. V. Freilich, D. M. Bianchi, A. M. Kaufman, T. K. Langin, and D. S. Hall, Science **329**, 1182 (2010).

[64] R. Grimm, M. Weidemüller, and Y. B. Ovchinnikov, Adv. At., Mol., Opt. Phys. **42**, 95 (2000).

[65] I. Bloch, J. Dalibard, and S. Nascimbene, Nature **8**, 267 (2012).

[66] J. Simon *et al.*, Nature **472**, 307 (2011).

[67] I. Bloch, Nature Phys. **1**, 23 (2005).

[68] C. Becker *et al.*, New J. Phys. **12**, 065025 (2010).

[69] P. Soltan-Panahi *et al.*, Nature Phys. **7**, 434 (2011).

[70] L. Tarruell, D. Greif, T. Uehlinger, G. Jotzu, and T. Esslinger, Nature **483**, 302 (2012).

[71] G.-B. Jo *et al.*, Phys. Rev. Lett. **108**, 045305 (2012).

[72] S. Fölling *et al.*, Nature **448**, 1029 (2007).

[73] G. W. Semenoff, Phys. Rev. Lett. **53**, 2449 (1984).

[74] D. C. Tsui, H. L. Stormer, and A. C. Gossard, Phys. Rev. Lett. **48**, 1559 (1982).

[75] R. B. Laughlin, Phys. Rev. Lett. **50**, 1395 (1983).

[76] N. R. Cooper, Adv. Phys. **57**, 539 (2008).

[77] K. W. Madison, F. Chevy, W. Wohlleben, and J. Dalibard, Phys. Rev. Lett. **84**, 806 (2000).

[78] J. R. Abo-Shaeer, C. Raman, J. M. Vogels, and W. Ketterle, Science **292**, 476 (2001).

[79] E. Hodby, G. Hechenblaikner, S. A. Hopkins, O. M. Maragò, and C. J. Foot, Phys. Rev. Lett. **88**, 010405 (2001).

[80] A. L. Fetter, Rev. Mod. Phys. **81**, 647 (2009).

[81] V. Bretin, S. Stock, Y. Seurin, and J. Dalibard, Phys. Rev. Lett. **92**, 050403 (2004).

[82] V. Schweikhard, I. Coddington, P. Engels, V. P. Mogendorff, and E. A. Cornell, Phys. Rev. Lett. **92**, 040404 (2004).

[83] M. Roncaglia, M. Rizzi, and J. I. Cirac, Phys. Rev. Lett. **104**, 096803 (2010).

[84] M. Roncaglia, M. Rizzi, and J. Dalibard, Sci. Rep. **1** (2011).

[85] R. Dum and M. Olshanii, Phys. Rev. Lett. **76**, 1788 (1996).

[86] M. J. Edmonds, M. Valiente, G. Juzeliūnas, L. Santos, and P. Öhberg, Phys. Rev. Lett. **110**, 085301 (2013).

[87] G. Juzeliūnas, J. Ruseckas, and J. Dalibard, Phys. Rev. A **81**, 053403 (2010).

[88] G. Juzeliūnas and P. Öhberg, Phys. Rev. Lett. **93**, 033602 (2004).

[89] G. Juzeliūnas, P. Öhberg, J. Ruseckas, and A. Klein, Phys. Rev. A **71**, 053614 (2005).

[90] G. Juzeliūnas, J. Ruseckas, P. Öhberg, and M. Fleischhauer, Phys. Rev. A **73**, 025602 (2006).

[91] K. J. Günter, M. Cheneau, T. Yefsah, S. P. Rath, and J. Dalibard, Phys. Rev. A **79**, 011604 (2009).

[92] Y.-J. Lin, R. L. Compton, K. Jimenez-Garcia, J. V. Porto, and I. B. Spielman, Nature **462**, 628 (2009).

[93] Y.-J. Lin *et al.*, Phys. Rev. Lett. **102**, 130401 (2009).

[94] I. B. Spielman, Phys. Rev. A **79**, 063613 (2009).

[95] Y.-J. Lin *et al.*, Nature Physics **7**, 531 (2011).

[96] N. R. Cooper, Phys. Rev. Lett. **106**, 175301 (2011).

[97] R. Peierls, Z. Phys. **80**, 763 (1933).

[98] J. Avron, in *Multiscale Methods in Quantum Mechanics*, pp. 11–22, Birkhäuser, 2004.

[99] D. R. Hofstadter, Phys. Rev. B **14**, 2239 (1976).

[100] D. Jaksch and P. Zoller, New J. Phys. **5**, 56 (2003).

[101] M. Aidelsburger *et al.*, Phys. Rev. Lett. **107**, 255301 (2011).

[102] M. Aidelsburger *et al.*, arXiv:1308.0321.

[103] E. J. Mueller, Physics **4**, 107 (2011).

[104] L.-K. Lim, A. Hemmerich, and C. M. Smith, Phys. Rev. A **81**, 023404 (2010).

[105] G. Möller and N. R. Cooper, Phys. Rev. A **82**, 063625 (2010).

[106] F. Gerbier and J. Dalibard, New J. Phys. **12**, 033007 (2010).

[107] N. R. Cooper and J. Dalibard, Europhys. Lett. **95**, 66004 (2011).

[108] N. R. Cooper and R. Moessner, Phys. Rev. Lett. **109**, 215302 (2012).

[109] N. R. Cooper and J. Dalibard, Phys. Rev. Lett. **110**, 185301 (2013).

[110] A. S. Sørensen, E. Demler, and M. D. Lukin, Phys. Rev. Lett. **94**, 086803 (2005).

[111] J. Struck *et al.*, Science **333**, 996 (2011).

[112] A. Eckardt *et al.*, Europhys. Lett. **89**, 10010 (2010).

[113] T. Kitagawa, E. Berg, M. Rudner, and E. Demler, Phys. Rev. B **82**, 235114 (2010).

[114] J. Struck *et al.*, Phys. Rev. Lett. **108**, 225304 (2012).

[115] J. Struck *et al.*, arXiv:1304.5520.

[116] P. Hauke *et al.*, Phys. Rev. Lett. **109**, 145301 (2012).

[117] S. Tung, V. Schweikhard, and E. A. Cornell, Phys. Rev. Lett. **97**, 240402 (2006).

[118] R. A. Williams, S. Al-Assam, and C. J. Foot, Phys. Rev. Lett. **104**, 050404 (2010).

[119] A. Klein and D. Jaksch, Europhys. Lett. **85**, 13001 (2009).

[120] K. Jiménez-García *et al.*, Phys. Rev. Lett. **108**, 225303 (2012).

[121] I. Žutić, J. Fabian, and S. Das Sarma, Rev. Mod. Phys. **76**, 323 (2004).

[122] M. Levin and A. Stern, Phys. Rev. Lett. **103**, 196803 (2009).

[123] V. Galitski and I. B. Spielman, Nature **494**, 49 (2013).

[124] C. Zhang, S. Tewari, R. M. Lutchyn, and S. Das Sarma, Phys. Rev. Lett. **101**, 160401 (2008).

[125] M. Gong, S. Tewari, and C. Zhang, Phys. Rev. Lett. **107**, 195303 (2011).

[126] T. D. Stanescu, B. Anderson, and V. Galitski, Phys. Rev. A **78**, 023616 (2008).

[127] T. A. Sedrakyan, A. Kamenev, and L. I. Glazman, Phys. Rev. A **86**, 063639 (2012).

[128] E. J. Mueller, Physics **5**, 96 (2012).

[129] Y.-J. Lin, K. Jiménez-García, and I. B. Spielman, Nature **471**, 83 (2011).

[130] J.-Y. Zhang *et al.*, Phys. Rev. Lett. **109**, 115301 (2012).

[131] P. Wang *et al.*, Phys. Rev. Lett. **109**, 095301 (2012).

[132] L. W. Cheuk *et al.*, Phys. Rev. Lett. **109**, 095302 (2012).

[133] J. Ruseckas, G. Juzeliūnas, P. Öhberg, and M. Fleischhauer, Phys. Rev. Lett. **95**, 010404 (2005).

[134] T. D. Stanescu, C. Zhang, and V. Galitski, Phys. Rev. Lett. **99**, 110403 (2007).

[135] D. L. Campbell, G. Juzeliūnas, and I. B. Spielman, Phys. Rev. A **84**, 025602 (2011).

[136] B. M. Anderson, G. Juzeliūnas, V. M. Galitski, and I. B. Spielman, Phys. Rev. Lett. **108**, 235301 (2012).

[137] N. Hatano, R. Shirasaki, and H. Nakamura, Phys. Rev. A **75**, 032107 (2007).

[138] S.-H. Chen and C.-R. Chang, Phys. Rev. B **77**, 045324 (2008).

[139] J. D. Sau, R. Sensarma, S. Powell, I. B. Spielman, and S. Das Sarma, Phys. Rev. B **83**, 140510 (2011).

[140] Z. F. Xu and L. You, Phys. Rev. A **85**, 043605 (2012).

[141] B. M. Anderson, I. B. Spielman, and G. Juzeliūnas, arXiv:1306.2606.

[142] Z.-F. Xu, L. You, and M. Ueda, arXiv:1306.2829.

[143] A. M. Dudarev, R. B. Diener, I. Carusotto, and Q. Niu, Phys. Rev. Lett. **92**, 153005 (2004).

[144] K. Osterloh, M. Baig, L. Santos, P. Zoller, and M. Lewenstein, Phys. Rev. Lett. **95**, 010403 (2005).

[145] M. Lewenstein *et al.*, Adv. Phys. **56**, 243 (2007).

[146] M. Atala *et al.*, arXiv:1212.0572.

[147] N. W. Ashcroft and D. N. Mermin, *Solid State Physics* (Thomson Learning, Toronto, 1976).

[148] M. Ben Dahan, E. Peik, J. Reichel, Y. Castin, and C. Salomon, Phys. Rev. Lett. **76**, 4508 (1996).

[149] C. F. Bharucha *et al.*, Phys. Rev. A **55**, R857 (1997).

[150] B. P. Anderson and M. A. Kasevich, Science **282**, 1686 (1998).

[151] G. Roati *et al.*, Phys. Rev. Lett. **92**, 230402 (2004).

[152] M. Fattori *et al.*, Phys. Rev. Lett. **100**, 080405 (2008).

[153] G. Ferrari, N. Poli, F. Sorrentino, and G. M. Tino, Phys. Rev. Lett. **97**, 060402 (2006).

[154] C. Zener, Proc. R. Soc. Lond. A **137**, 696 (1932).

[155] J. Feldmann *et al.*, Phys. Rev. B **46**, 7252 (1992).

[156] M. Cominotti and I. Carusotto, arXiv:1302.3165.

[157] A. R. Kolovsky and G. Mantica, Phys. Rev. E **83**, 041123 (2011).

[158] A. R. Kolovsky, Front. Phys. **7** (2012).

[159] T. Fukui, Y. Hatsugai, and H. Suzuki, J. Phys. Soc. Jpn. **74**, 1674 (2005).

[160] G. Pettini and M. Modugno, Phys. Rev. A **83**, 013619 (2011).

[161] D. Witthaut, F. Keck, H. J. Korsch, and S. Mossmann, New J. Phys. **6**, 41 (2004).

[162] A. R. Kolovsky and H. J. Korsch, Phys. Rev. A **67**, 063601 (2003).

[163] S. Mossmann, A. Schulze, D. Witthaut, and H. J. Korsch, J. Phys. A **38**, 3381 (2005).

[164] J. M. Zhang and W. M. Liu, Phys. Rev. A **82**, 025602 (2010).

[165] L.-K. Lim, J.-N. Fuchs, and G. Montambaux, Phys. Rev. Lett. **108**, 175303 (2012).

[166] F. D. M. Haldane, Phys. Rev. Lett. **61**, 2015 (1988).

[167] Y. Zhang, Y. Tan, H. Stormer, and P. Kim, Nature **438**, 201 (2005).

[168] K. Novoselov *et al.*, Nature **438**, 197 (2005).

[169] S. Y. Zhou *et al.*, Nature Mater. **6**, 770 (2007).

[170] D. Xiao, W. Yao, and Q. Niu, Phys. Rev. Lett. **99**, 236809 (2007).

[171] J. N. Fuchs, F. Pichon, M. O. Goerbig, and G. Montambaux, EPJ B **77**, 351 (2010).

[172] R. B. Diener, A. M. Dudarev, G. Sundaram, and Q. Niu, arXiv:0306184.

[173] M. Kohmoto, Ann. Phys. **160**, 343 (1985).

[174] T. Esslinger, Private Communication .

[175] A. Trombettoni and A. Smerzi, Phys. Rev. Lett. **86**, 2353 (2001).

[176] A. M. Dudarev, R. B. Diener, and Q. Niu, J. Opt. B **6**, S231 (2004).

[177] M. Gustavsson *et al.*, Phys. Rev. Lett. **100**, 080404 (2008).

[178] E. Zhao, N. Bray-Ali, C. J. Williams, I. B. Spielman, and I. I. Satija, Phys. Rev. A **84**, 063629 (2011).

[179] E. Alba, X. Fernandez-Gonzalvo, J. Mur-Petit, J. K. Pachos, and J. J. Garcia-Ripoll, Phys. Rev. Lett. **107**, 235301 (2011).

[180] D. A. Abanin, T. Kitagawa, I. Bloch, and E. Demler, Phys. Rev. Lett. **110**, 165304 (2013).

[181] T. D. Stanescu, V. Galitski, and S. Das Sarma, Phys. Rev. A **82**, 013608 (2010).

[182] X.-J. Liu, X. Liu, C. Wu, and J. Sinova, Phys. Rev. A **81**, 033622 (2010).

[183] N. Goldman, J. Beugnon, and F. Gerbier, Phys. Rev. Lett. **108**, 255303 (2012).

[184] N. Goldman *et al.*, Proc. Natl. Acad. Sci. USA **110**, 6736 (2013).

[185] J.-P. Brantut, J. Meineke, D. Stadler, S. Krinner, and T. Esslinger, Science **337**, 1069 (2012).

[186] A. Dauphin and N. Goldman, arXiv:1305.3872.

[187] L. J. LeBlanc *et al.*, Proc. Natl. Acad. Sci. U.S.A. **109**, 10811 (2012).

[188] A. Altmeyer *et al.*, Phys. Rev. Lett. **98**, 040401 (2007).

[189] M. Bartenstein *et al.*, Phys. Rev. Lett. **92**, 203201 (2004).

[190] H. Heiselberg, Phys. Rev. Lett. **93**, 040402 (2004).

[191] D. Jin, J. Ensher, M. Matthews, C. Wieman, and E. Cornell, Phys. Rev. Lett. **77**, 420 (1996).

[192] M.-O. Mewes *et al.*, Phys. Rev. Lett. **77**, 988 (1996).

[193] D. Stamper-Kurn, H.-J. Miesner, S. Inouye, M. Andrews, and W. Ketterle, Phys. Rev. Lett. **81**, 500 (1998).

[194] S. E. Pollack *et al.*, Phys. Rev. A **81**, 053627 (2010).

[195] F. Zambelli and S. Stringari, Phys. Rev. Lett. **81**, 1754 (1998).

[196] F. Chevy, K. W. Madison, and J. Dalibard, Phys. Rev. Lett. **85**, 2223 (2000).

[197] V. Bretin, P. Rosenbusch, F. Chevy, G. V. Shlyapnikov, and J. Dalibard, Phys. Rev. Lett. **90**, 100403 (2003).

[198] D. Guéry-Odelin and S. Stringari, Phys. Rev. Lett. **83**, 4452 (1999).

[199] O. M. Maragò *et al.*, Phys. Rev. Lett. **84**, 2056 (2000).

[200] M. Kottke *et al.*, Phys. Rev. A **72**, 053631 (2005).

[201] J. Lye *et al.*, Phys. Rev. Lett. **95**, 070401 (2005).

[202] P. A. Ruprecht, M. J. Holland, K. Burnett, and M. Edwards, Phys. Rev. A **51**, 4704 (1995).

[203] V. M. Pérez-García, H. Michinel, J. I. Cirac, M. Lewenstein, and P. Zoller, Phys. Rev. Lett. **77**, 5320 (1996).

[204] Y. Castin and R. Dum, Phys. Rev. Lett. **77**, 5315 (1996).

[205] T. D. Lee and C. N. Yang, Phys. Rev. **105**, 1119 (1957).

[206] T. D. Lee, K. Huang, and C. N. Yang, Phys. Rev. **106**, 1135 (1957).

[207] L. Pitaevskii and S. Stringari, Phys. Rev. Lett. **81**, 4541 (1998).

[208] G. E. Astrakharchik, R. Combescot, X. Leyronas, and S. Stringari, Phys. Rev. Lett. **95**, 030404 (2005).

[209] S. Stringari, Phys. Rev. Lett. **77**, 2360 (1996).

[210] M. Krämer, L. Pitaevskii, and S. Stringari, Phys. Rev. Lett. **88**, 180404 (2002).

[211] A. Griffin, W.-C. Wu, and S. Stringari, Phys. Rev. Lett. **78**, 1838 (1997).

[212] G. M. Bruun and C. W. Clark, Phys. Rev. Lett. **83**, 5415 (1999).

[213] M. Amoruso, I. Meccoli, A. Minguzzi, and M. Tosi, EPJ D **7**, 441 (1999).

[214] G. I. Martone, Y. Li, L. P. Pitaevskii, and S. Stringari, Phys. Rev. A **86**, 063621 (2012).

[215] Y. Li, G. I. Martone, and S. Stringari, Europhys. Lett. **99**, 56008 (2012).

[216] E. van der Bijl and R. A. Duine, Phys. Rev. Lett. **107**, 195302 (2011).

[217] W. Kohn, Phys. Rev. **123**, 1242 (1961).

[218] J. F. Dobson, Phys. Rev. Lett. **73**, 2244 (1994).

[219] W. Thomas, Naturwissenschaften **13**, 627 (1925).

[220] W. Kuhn, Z. Phys. **33**, 408 (1925).

[221] F. Reiche and W. Thomas, Z. Phys. **34**, 510 (1925).

[222] D. N. Basov *et al.*, Science **283**, 49 (1999).

[223] O. Bohigas, A. Lane, and J. Martorell, Phys. Rep. **51**, 267 (1979).

[224] M. A. Shifman, A. Vainshtein, and V. I. Zakharov, Nucl. Phys. B **147**, 385 (1979).

[225] E. Lipparini, *Modern many-particle physics : atomic gases, quantum dots and quantum fluids* (World Scientific, Singapore, 2003).

[226] J. M. Luttinger and W. Kohn, Phys. Rev. **97**, 869 (1955).

[227] J. Callaway, *Quantum theory of the solid state* (Academic Press, 1991).

[228] N. R. Cooper, Phys. Rev. Lett. **80**, 4554 (1998).

[229] Z. Hadzibabic and J. Dalibard, Riv. Nuovo Cimento **34** (2011).

[230] N. Papanicolaou and T. Tomaras, Nucl. Phys. B **360**, 425 (1991).

[231] P. G. Saffman, *Vortex Dynamics* (CUP, Cambridge, 1992).

[232] C. Yin *et al.*, Phys. Rev. A **83**, 051605 (2011).

[233] N. G. Berloff, Phys. Rev. Lett. **94**, 120401 (2005).

[234] A. M. Kosevich, B. A. Ivanov, and A. S. Kovalev, Phys. Rep **194**, 117 (1990).

[235] N. Berloff and C. Yin, J. Low Temp. Phys. **145**, 187 (2006).

[236] K. M. Mertes *et al.*, Phys. Rev. Lett. **99**, 190402 (2007).

[237] R. A. Leese, M. Peyrard, and W. J. Zakrzewski, Nonlinearity **3**, 773 (1990).

[238] S. Komineas, Phys. D **155**, 223 (2001).

[239] L. Fu and C. L. Kane, Phys. Rev. B **74**, 195312 (2006).

[240] L. Kadanoff and G. Baym, *Quantum statistical mechanics: Green's function methods in equilibrium and nonequilibrium problems* (Frontiers in physics, W.A. Benjamin, 1962).

[241] Y. Li, L. P. Pitaevskii, and S. Stringari, Phys. Rev. Lett. **108**, 225301 (2012).